AD-A058 714 FRANK J SEILER RESEARCH LAB UNITED STATES AIR FORCE --ETC F/G 20/4
UNSTEADY BOUNDARY LAYER FLOW REVERSAL IN A LONGITUDINALLY OSCIL--ETC(U)
AUG 78 J P RETELLE
FJSRL-TR-78-0006

UNCLASSIFIED NL

1 OF 2
AD A058714



AD A058714

DDC FILE COPY

LEVEL II

FRANK J. SEILER RESEARCH LABORATORY

SRL-TR-78-0006

AUGUST 1978

UNSTEADY BOUNDARY LAYER FLOW REVERSAL IN A LONGITUDINALLY OSCILLATING FLOW

DDC
RECEIVED
SEP 13 1978
F

FINAL REPORT

CAPT JOHN P. RETELLE, JR.

APPROVED FOR PUBLIC RELEASE;
DISTRIBUTION UNLIMITED.

PROJECT 2307

AIR FORCE SYSTEMS COMMAND
UNITED STATES AIR FORCE

78 09 01 050

This document was prepared by the Mechanics Division, Directorate of Aerospace-Mechanics Sciences, Frank J. Seiler Research Laboratory, United States Air Force Academy, Colorado. The research was conducted under Project Work Unit Number 2307-F1-34, An Investigation of the Flow Dynamics of Unsteady Separated Regions. Capt John P. Retelle, Jr., was the Project Engineer in charge of the work.

When U.S. Government drawings, specifications or other data are used for any purpose other than a definitely related Government procurement operation, the Government thereby incurs no responsibility nor any obligation whatsoever, and the fact that the Government may have formulated, furnished or in any way supplied the said drawings, specifications or other data is not to be regarded by implication or otherwise, as in any manner licensing the holder or any other person or corporation or conveying any rights or permission to manufacture, use or sell any patented invention that may in any way be related thereto.

Inquiries concerning the technical content of this document should be addressed to the Frank J. Seiler Research Laboratory (AFSC), FJSRL/NH, USAF Academy, Colorado 80840. Phone AC 303-472-3122.

This report has been reviewed by the Chief Scientist and is releasable to the National Technical Information Service (NTIS). At NTIS it will be available to the general public, including foreign nations.

This technical report has been reviewed and is approved for publication.

JOHN P. RETELLE, JR., Capt, USAF
Project Engineer

JOSEPH S. FORD II, Lt Col, USAF
Director
Aerospace-Mechanics Sciences

FOR THE COMMANDER

CHARLES E. SIMON, Lt Col, USAF
Chief Scientist

Copies of this report should not be returned unless return is required by security considerations, contractual obligations, or notice on a specific document.

Printed in the United States of America. Qualified requestors may obtain additional copies from the Defense Documentation Center. All others should apply to: National Technical Information Service
5285 Port Royal Road
Springfield, Virginia 22161

UNCLASSIFIED

SECURITY CLASSIFICATION OF THIS PAGE (When Data Entered)

REPORT DOCUMENTATION PAGE

READ INSTRUCTIONS BEFORE COMPLETING FORM

1. REPORT NUMBER: FJSRL-TR-78-0006 AD A-	2. GOVT ACCESSION NO.
3. RECIPIENT'S CATALOG NUMBER	
4. TITLE (and Subtitle): UNSTEADY BOUNDARY LAYER FLOW REVERSAL IN A LONGITUDINALLY OSCILLATING FLOW,	5. TYPE OF REPORT & PERIOD COVERED: Final Report, August 1975 - August 1978,
6. PERFORMING ORG. REPORT NUMBER	
7. AUTHOR(s): Capt John P. Retelle, Jr	8. CONTRACT OR GRANT NUMBER(s)
9. PERFORMING ORGANIZATION NAME AND ADDRESS: Frank J. Seiler Research Lab (AFSC) USAF Academy, CO 80840	10. PROGRAM ELEMENT, PROJECT, TASK AREA & WORK UNIT NUMBERS: DRS 61102F 2307-F1-34 F1
11. CONTROLLING OFFICE NAME AND ADDRESS: Frank J. Seiler Research Lab USAF Academy, CO 80840	12. REPORT DATE: August 1978
	13. NUMBER OF PAGES: 136
14. MONITORING AGENCY NAME & ADDRESS (if different from Controlling Office): 140p.	15. SECURITY CLASS. (of this report): UNCLASSIFIED
	15a. DECLASSIFICATION/DOWNGRADING SCHEDULE

16. DISTRIBUTION STATEMENT (of this Report)

Approved for public release; distribution unlimited.

17. DISTRIBUTION STATEMENT (of the abstract entered in Block 20, if different from Report)

18. SUPPLEMENTARY NOTES

19. KEY WORDS (Continue on reverse side if necessary and identify by block number)

Unsteady Flow
Unsteady Boundary Layers
Flow Reversal
Split Film Probe
Oscillating Flow
Wind Tunnel
Dynamic Stall

20. ABSTRACT (Continue on reverse side if necessary and identify by block number)

Measurements of boundary layer flow reversal made in a wind tunnel on a stationary NACA 0012 airfoil immersed in a longitudinally oscillating subsonic flow are described. A split-film sensor provided flow reversal data in regions above the airfoil surface throughout the period of flow oscillation. At angles of attack below the steady-flow stall angle of attack and for small amplitude oscillations, regions of boundary layer flow reversal near the leading edge were observed to vary nominally in phase with the time-varying

DD FORM 1 JAN 73 1473 EDITION OF 1 NOV 65 IS OBSOLETE

UNCLASSIFIED

SECURITY CLASSIFICATION OF THIS PAGE (When Data Entered)

319 920

78 09 01 050

LB

external velocity. However, an increase in the oscillation amplitude produced a phase lead and an increased downstream extent of the flow reversal region. Variations in the oscillation frequency produced only small changes in the shape of the flow reversal region. For angles of attack greater than the steady-flow stall angle, the growth and decay of reversed flow regions were observed to be stronger functions of the velocity oscillation frequency and amplitude. Increases in oscillation amplitude produced larger reversal regions which nominally lagged the phase of the free stream velocity. Although the unsteady wind tunnel was adjusted to reduce harmonic content, the presence of higher harmonics in the power spectrum of the oscillating free stream velocity was observed to produce flow reversals which led the phase of the free stream velocity. It is shown that boundary layer flow reversal on a stationary airfoil in an oscillating free stream responds to changes in the flow unsteadiness in a manner similar to the flow reversal observed during the onset of dynamic stall on an airfoil oscillating in pitch.

ACCESSION for
NTIS White Section
DDC Buff Section
UNANNOUNCED
JUSTIFICATION
BY
DISTRIBUTION/AVAILABILITY CODES
Dist.
A

TABLE OF CONTENTS

CHAPTER		PAGE
1.	INTRODUCTION	1
	1.1 Statement of the Problem.	1
	1.2 Oscillating Freestream Velocity Experiments	3
	1.3 Dynamic Stall Experiments	11
	1.4 Optimization of Oscillating Free Stream	15
2.	EXPERIMENTAL APPARATUS AND PROCEDURE	18
	2.1 Unsteady Wind Tunnel Configuration.	18
	2.2 Airfoil Configuration	26
	2.3 Velocity Measurements	27
	2.4 Flow Reversal Measurement	38
	2.5 Data Processing	41
	2.6 Sources of Error.	45
3.	UNSTEADY FLOW FIELD HARMONIC OPTIMIZATION.	47
4.	RESULTS AND DISCUSSION OF FLOW REVERSAL MEASUREMENTS	58
	4.1 Steady Flow Boundary Layer Reversal	58
	4.2 Unsteady Boundary Layer Equations	61
	4.3 Unsteady Flow Reversal for Angles of Attack Below the Steady Flow Stall Angle	73
	4.4 Unsteady Flow Reversal for Angles of Attack Above the Steady Flow Stall Angle	77

CHAPTER PAGE

5. FREQUENCY EFFECTS ON FLOW REVERSAL 87

5.1 Frequency Effects for Angles of Attack Below the Steady Flow Stall Angle 87

5.2 Frequency Effects for Angles of Attack Above the Steady Stall Angle. 91

6. OSCILLATION AMPLITUDE EFFECTS ON FLOW REVERSAL 102

6.1 Amplitude Effects for Angles of Attack Below the Steady Flow Stall Angle 102

6.2 Amplitude Effects for Angles of Attack Above the Steady Flow Stall Angle 104

7. CONCLUSIONS. 109

REFERENCES 113

APPENDIX A 116

APPENDIX B 122

NOTATION

$A(x)$	wind tunnel cross-section area, as a function of longitudinal distance
B	constant coefficient in King's Law equation
E	hot-wire anemometer output voltage
E_o	constant voltage in King's Law equation
F_1	pressure drop coefficient across main-flow rotating vanes
F_2	pressure drop coefficient across bypass-flow rotating vanes
K	kurtosis factor of u_1', i.e., $(\overline{u_1'^4})/(\overline{u_1'^2})^2$
K_{mn}	pressure changes between wind tunnel stations m and n
$L/2$	width of top or bottom bypass port opening in the unsteady flow generator
N	oscillating velocity amplitude ratio, i.e., $n = \frac{\Delta U}{U_1} = \frac{(U_{maximum} - U_1)}{U_1}$
$Q(x,t)$	mass flow per unit volume, $A(x)u(x,t)$
Q_o	steady-flow mass flow per unit volume
Q_1	mass flow per unit volume through main-flow rotating vanes
Q_2	mass flow through bypass rotating vanes
R	Reynolds number, $\frac{U_1 \rho c}{\mu}$
R_1	sum of coefficients of viscous and pressure losses for flow through tunnel test section and main-flow vanes
R_2	sum of coefficients of viscous and pressure drop losses for flow through bypass ports and bypass vanes
R'	coefficient of viscous and pressure losses for identical main-flow and bypass rotating vanes
S	skewness factor of u_1', i.e., $(\overline{u_1'^3})/(\overline{u_1'^2})^{3/2}$

T	time interval representing the maximum size of the digitized data sample in the time domain
U_∞	free stream velocity (steady or oscillatory)
U_o	free stream velocity prior to operating unsteady flow device
U_1	mean value of oscillating longitudinal free stream velocity
V	voltage
V_1	voltage used to compute the power contained in the first harmonic of the velocity oscillation power spectrum
V_2	voltage used to compute the power contained in the second harmonic of the velocity oscillation power spectrum
$\langle V \rangle$	average voltage resulting from the ensemble average process
c	airfoil chord length
$f_1(t)$	unsteady component of pressure drop coefficient across main-flow rotating vanes
$f_2(t)$	unsteady component of pressure drop coefficient across bypass rotating vanes
$\hat{f}_1(t)$	nondimensional value of $f_1(t)$, i.e., $f_1/2R'$
$\hat{f}_2(t)$	nondimensional value of $f_2(t)$, i.e., $f_2/2R'$
k	reduced frequency, $\frac{\omega c}{2U_1}$
n	exponent of velocity term in King's Law equation
p	ensemble counter parameter
$q_1(t)$	unsteady component of $Q_1(x,t)$
$q_2(t)$	unsteady component of $Q_2(x,t)$
r^2	ratio of $R_1/R_2 = (Q_{20}/Q_{10})^{\frac{1}{2}}$
t	time
u	velocity component in longitudinal direction
v	velocity component in vertical direction
x	length dimension along longitudinal (axial) coordinate
$\bar{x}$	nondimensional distance along the airfoil chord, i.e., x/c

$\underset{\sim}{x}$	position vector, $\lvert\underset{\sim}{x}\rvert = \sqrt{x^2 + y^2 = z^2}$
y	length dimension along vertical coordinate
z	length dimension along horizontal (spanwise) coordinate
α	airfoil angle of attack
α_{mn}	mass flow passing between wind tunnel stations m and n
β	coefficient of fan pressure drop
$\gamma(x)$	coefficient of viscous losses
Δf	frequency interval between digital data words in frequency domain
ΔP_f	steady pressure drop across fan
Δp_f	unsteady pressure drop across fan
Δt	time interval between digital data words in time domain
Δy	distance between probe measurement and airfoil surface
κ	streamline curvature
μ	coefficient of viscosity of air
ρ	air density
τ_1	time constant associated with area changes upstream of test section, i.e., α_1/RQ_0
τ_3	time constant associated with area changes downstream of test section, i.e., α_3/RQ_0
ϕ_1	vane rotation angle of main-flow vane
ϕ_2	vane rotation angle of bypass-flow vane
$(\bar{\ })$	denotes a time average
$\langle\ \rangle$	denotes an ensemble average

1. INTRODUCTION

1.1 Statement of the Problem

This experiment was conducted to provide information which would lead to a better understanding of the onset of unsteady flow reversal in attached and separated boundary layers. Regions of flow reversal are produced by unsteady flow effects and are often encountered in flows associated with maneuvering aircraft and retreating helicopter blades. These two dynamic applications involve rapid changes of both angle of attack and flow velocity. Previous experimental investigations have considered these parametric variations separately. Experiments conducted on stationary airfoils in oscillatory flows which are described below have involved regions of reversed flow imbedded in attached boundary layers. Other experiments concerned with dynamic stall phenomena have shown that airfoils oscillating in pitch may produce unsteady values of lift and pitching moment which greatly exceed those obtained for a stationary airfoil. In both these cases, the flow unsteadiness produced an unseparated flow reversal region on the airfoil upper surface which subsequently formed a recirculating flow region near the leading edge. The only quantitative measurements of the onset of the flow reversal region have been on the airfoil surface due to the limitations of data collection transducers.

Regions of unsteady boundary layer flow reversal were measured above the stationary airfoil which were related to those measured at the surface of the oscillating airfoil. However, the spatial extent of the flow reversal above the surface could be measured with greater ease and accuracy above the fixed airfoil. Also, this experiment allowed for an investigation of the parameters of the unsteady flow field, without strong coupling with the inertial effects of the airflow about the oscillating airfoil. Variations in the frequency and amplitude of the unsteady velocity oscillations were observed to have a strong influence on the boundary layer flow reversal. This influence was found to be similar to the unsteady effects noted with the dynamic stall of oscillating airfoils.

This experiment was motivated by a desire to investigate the feasibility of constructive applications of dynamic effects for maneuvering flight. Aircraft have classically been designed using aerodynamic characteristics derived from steady flow considerations since experimental data were not available to describe the aerodynamics of unsteady flow. For example, the solutions to the aircraft equations of motion, while dynamic in themselves, have been generated using forcing functions based on steady stability derivatives. These derivatives have been calculated using wind tunnel data collected at fixed values of velocity and angle of attack. A more thorough understanding of the unsteady variations of lift and pitching moment during both dynamic stall and dynamic velocity variation might allow aircraft to be designed to control and utilize the high lift transients generated by this dynamic process for ,

improved maneuvering capabilities. Properly configured aircraft might briefly fly outside the static flight envelope which has classically been used to define aircraft flight limits.

1.2 Oscillating Freestream Velocity Experiments

The boundary layer flow reversals which often initiate the dynamic stall process were difficult to measure in moving-airfoil experiments. Flow sensors could not easily be positioned above the moving airfoil. Flow reversal data have been more conveniently collected on a stationary airfoil immersed in a longitudinally oscillating flow. Such experiments, described below, have proven more suitable for describing the unsteady effects which may provide the mechanisms which lead to dynamic stall. However, the global effects of the classical dynamic stall, namely the separation of a leading edge vortex, and the large hysteresis effects on lift, were not seen with this experimental environment.

A typical reversed flow region observed above the fixed airfoil at one phase point of the freestream velocity oscillation is shown in Figure 1. A thin layer of reversed flow was imbedded within the boundary layer, but flow remained attached to the airfoil surface. This unsteady flow result was markedly different from the steady flow case where flow reversal (or zero skin friction) has defined the onset of boundary layer separation. A typical evolution of the reversed flow region during an oscillation period is shown in Figure 2. Flow reversal was observed to start near the leading edge at approximately the π-radian phase point (Figure 2b) in the oscillation cycle. As the magnitude of the free stream velocity

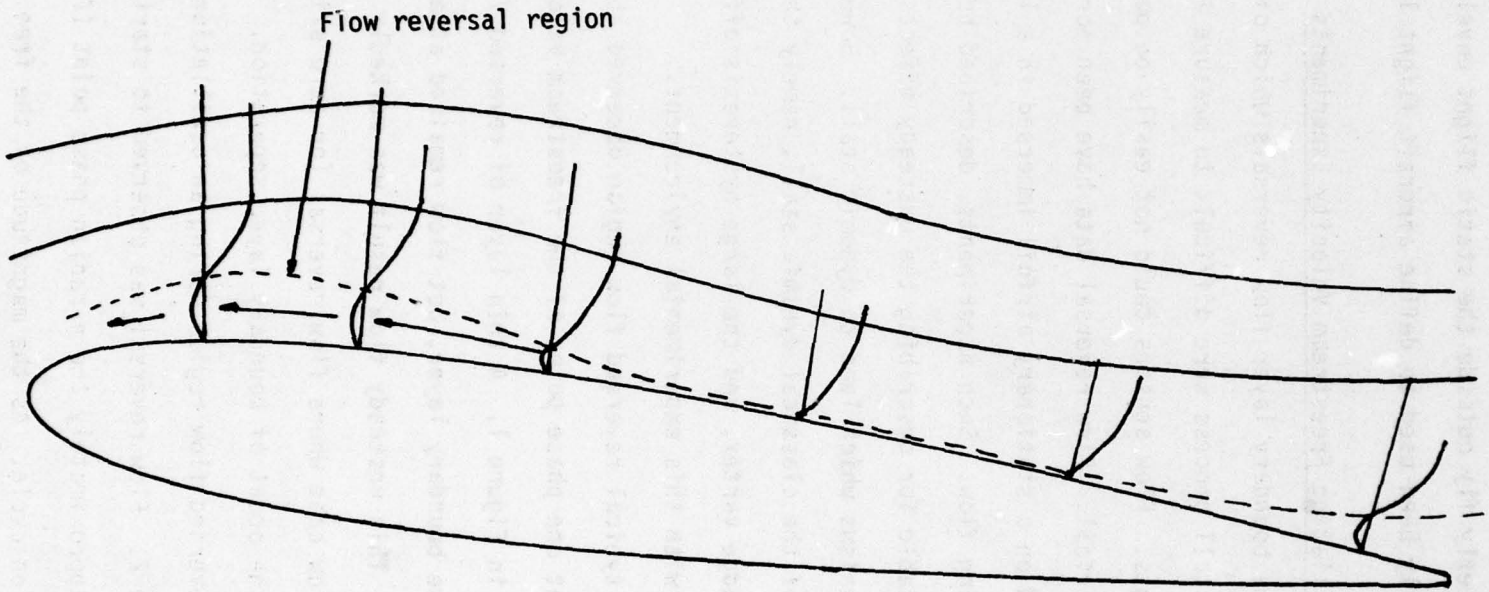
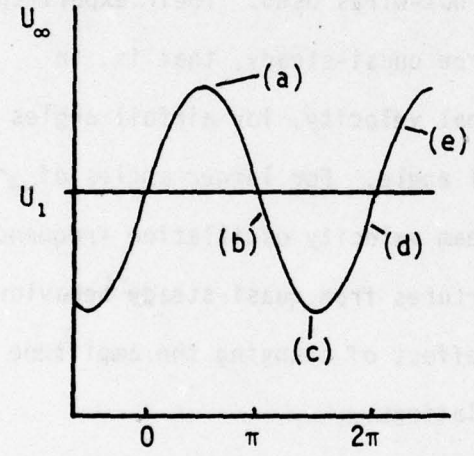


Figure 1
UNSTEADY FLOW REVERSAL ON STATIONARY NACA 0012 AIRFOIL



Oscillating Free Stream Velocity

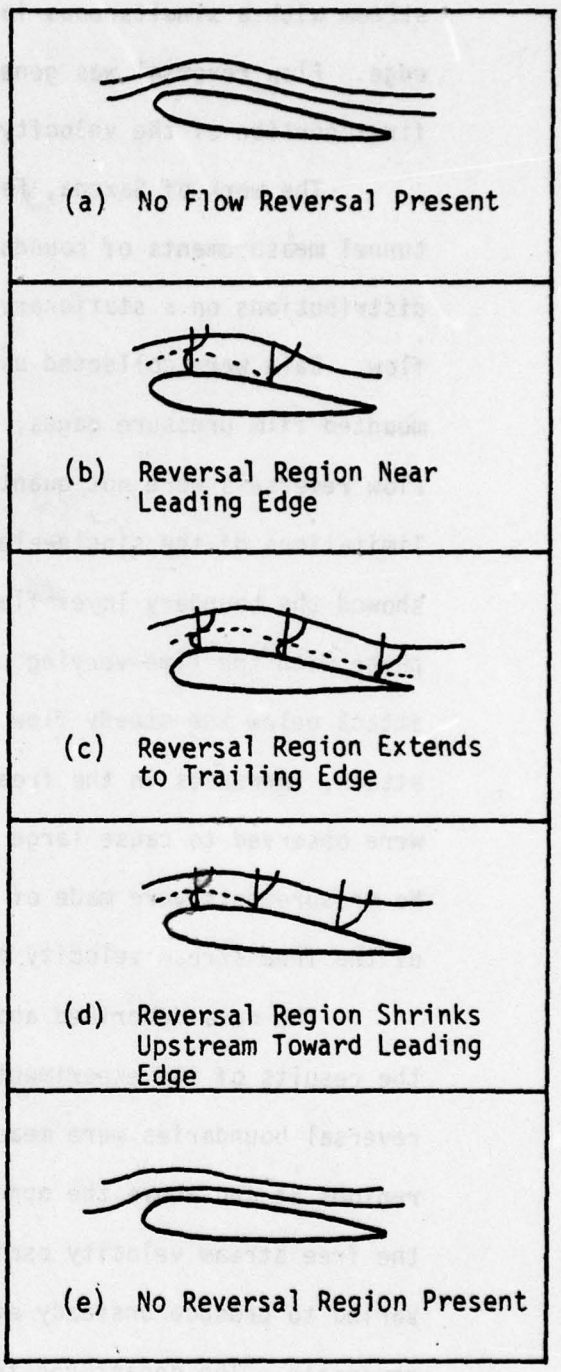


Figure 2
FLOW REVERSAL EVENTS ON STATIONARY NACA 0012 AIRFOIL

decreased (Figure 2c), the reversal region extended further downstream with a simultaneous increase in height near the leading edge. Flow reversal was generally observed to be absent for the first portion of the velocity oscillation period ($0 \leq \omega t \leq \pi$).

The work of Saxena, Fejer, and Morkovin[1] describes wind tunnel measurements of boundary layer profiles and surface pressure distributions on a stationary NACA 0012 airfoil in an oscillating flow. Data were collected using hot-wire anemometers, surface-mounted film pressure gages, and flow visualization using tufts. Flow reversals were not quantitatively measured because of the limitations of the single-element hot-wires used. Their experiments showed the boundary layer flow to be quasi-steady, that is, in phase with the time-varying external velocity, for airfoil angles of attack below the steady flow stall angle. For larger angles of attack, increases in the free stream velocity oscillation frequency were observed to cause large departures from quasi-steady behavior. No measurements were made of the effect of changing the amplitude of the free stream velocity oscillations.

The data described above are supplemented and amplified by the results of the experiment presented below. Boundary layer flow reversal boundaries were measured using a split-film sensor in regions at and above the upper surface of a NACA 0012 airfoil. Both the free stream velocity oscillation amplitude and frequency were varied to produce unsteady effects on the boundary layer flow reversals. The departures from quasi-steady behavior were found to depend on oscillation frequency in a similar manner to that noted by Saxena, Fejer, and Morkovin.[1] However, the results described

here are based upon quantitative measurements of flow reversal rather than inference from surface pressure measurements. These results also show the strong influence of changes in the velocity oscillation magnitude. The effects of large velocity oscillation amplitudes were observed in both the departures from quasi-steady behavior and the large changes in the shape and size of the flow reversal region.

The scheme of oscillating the longitudinal velocity about a mean was used in the analytical studies of Lighthill,[2] Lin,[3] and Nickerson.[4] For the boundary layer above a semi-infinite flat plate, the analyses indicated that both the wall shear and boundary layer thickness were functions of the reduced frequency of velocity oscillation. The reduced frequency, which resembles the Strouhal number in form, depends on the oscillation frequency and the mean velocity. For low frequencies, the boundary layer responded to the flow unsteadiness in a quasi-steady manner, i.e., in phase with the free stream flow. For high frequencies, the analysis predicted that the unsteady effects were confined to a thin shear layer near the wall and that shear response phase in this layer led the free stream by 45 degrees for laminar flow and by about 10-15 degrees for turbulent flow. Experimental data collected by Karlsson,[5] Hill and Stenning,[6] Cousteix, et. al.[7] and Patel[8] confirmed these predictions for both laminar and turbulent boundary layers on semi-infinite flat plates. Additional confirmation was provided by the numerical studies of Patel and Nash[9] and Telionis, Tsahalis, and Werle.[10] Their calculations for flat plates predicted the presence of thin regions of reversed flow ahead of the point of separation

of the unsteady boundary layer. The flow reversal indicated that, for unsteady flows, there was no correlation between zero wall shear and separation. The effects of variations of the unsteady flow parameters (velocity oscillation frequency and amplitude) on the flow reversals were also computed.

Calculations were also made to predict the point of separation of unsteady boundary layers subjected to spatial pressure gradients. Numerical results were used by Sears and Telionis[11] to propose the unsteady boundary layer separation model summarized in Figure 3. At a particular phase point in the velocity oscillation cycle, the point of zero surface shear is followed downstream by a thin layer of reversed flow. The model shows a thickened reversed flow region further downstream. Sears and Telionis contend that the start of this aft thickened region represents the separation point of the unsteady boundary layer. The numerical calculations of Nash and Scruggs,[12] and Nash[13] also predicted an increase in the displacement boundary layer thickness downstream of the initial flow reversal region but made no predictions of flow separation.

Experiments have been conducted to measure the influence of oscillating flows on both boundary layer flow reversals and flow separation. The influence of flow unsteadiness on laminar separation from a semi-infinite flat plate was measured by Despard and Miller.[14] The point of separation was observed to occur upstream of the steady separation point. Changes in the flow Reynolds number and oscillation frequency greatly influenced the separation point location, while almost no effect was noted due to changes in the velocity oscillation amplitude.

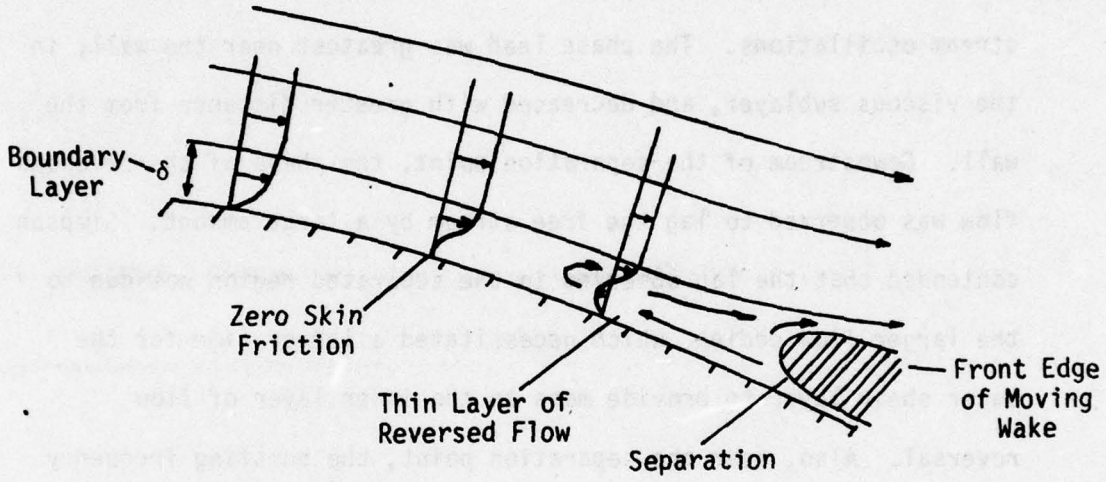


Figure 3
FLOW REVERSAL AND SEPARATION MODEL
(reference 14)

Other experiments measured the phase shift between the unsteady boundary layer response and the oscillating freestream. Simpson[15] measured flow reversals in a turbulent boundary layer on a flat plate with a longitudinal spatial pressure gradient. Data were collected using hot-wire anemometers and a laser flow visualization scheme. The phase of the reversed flow region was noted both upstream and downstream of the flow separation point. Upstream of the separation point, the phase of the reversed flow led the free stream oscillations. The phase lead was greatest near the wall, in the viscous sublayer, and decreased with greater distance from the wall. Downstream of the separation point, the phase of the reversed flow was observed to lag the free stream by a large amount. Simpson contended that the lag observed in the separated region was due to the larger flow eddies, which necessitated a larger time for the outer shear layer to provide mass to the inner layer of flow reversal. Also, near the separation point, the bursting frequency of the turbulent boundary layer was observed to decrease. As this frequency became closer to the free stream oscillation frequency, a greater interaction was noted between the boundary layer and the free stream.

Kennison[16] also measured flow reversals in a turbulent boundary layer on a flat plate with an adverse spatial pressure gradient. However, the oscillating free stream velocity included a traveling wave disturbance which convected downstream at less than the mean free stream velocity. Hot-wire anemometers and hot-film surface gages produced data which, when corrected, measured flow reversals. For this type of flow oscillation, the adverse spatial

pressure gradient was observed to produce a phase lag in the flow reversal region which increased with downstream movement. The greatest magnitude of phase lag was noted in the outer region of the boundary layer. The thin layer of flow reversal ahead of the flow separation point had little effect on the boundary layer momentum thickness, indicating that there was little vorticity transfer into the free stream. The phase lag of the flow reversal was probably due to the presence of the traveling wave disturbance in the free stream velocity.

1.3 Dynamic Stall Experiments

Unsteady flow wind tunnel experiments have also measured the dynamic stall phenomena caused by rapid changes in airfoil angle of attack. Previous experiments have utilized oscillating airfoil motion in steady wind tunnel flows. McCroskey and Philippe[17] used a NACA 0012 airfoil oscillating in pitch about a fixed angle of attack near the steady stall angle. Surface pressure measurements were made to determine the changes in the lift and pitching moment as the angle of attack was varied. Results showed increased values of lift and pitching moment over the steady values, as well as large non-linear hysterisis effects in both parameters. Hot-film gages and hot-wire anemometers were used to measure flow reversal. The dynamic stall events observed on a NACA 0012 airfoil are presented in Figure 4 (reprinted from reference 19). The onset of this process is indicated by the appearance of boundary layer flow reversal in Figure 4(b). This reversed flow is observed to precede the formation of a vortex-like disturbance near the leading edge in

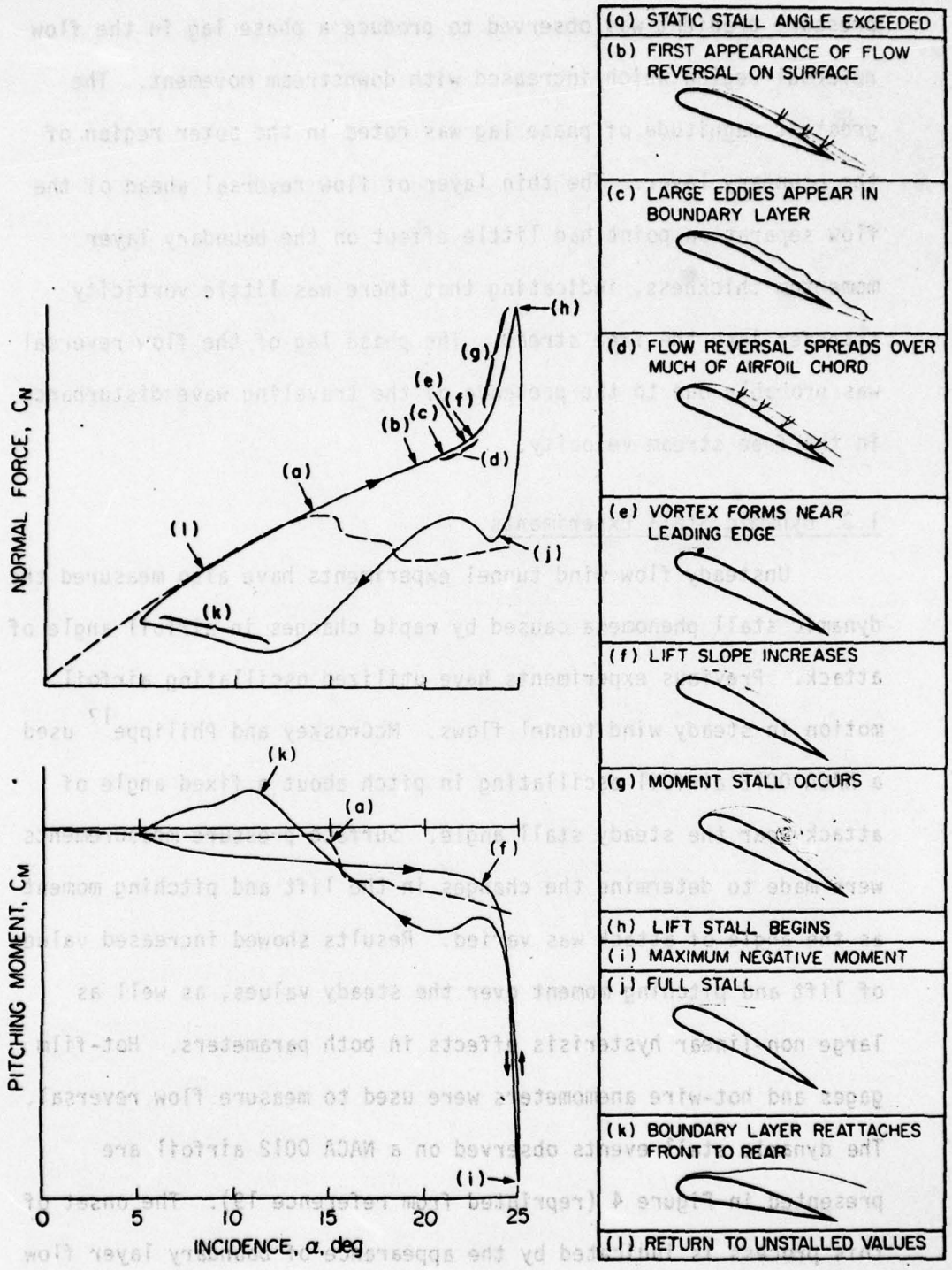


Figure 4
DYNAMIC STALL EVENTS ON OSCILLATING NACA 0012 AIRFOIL
(reference 3)

Figure 4(e). The subsequent separation of this vortex from the airfoil surface produced a rapid drop in the pitching moment (Figure 4(g) - moment stall) and then a drop in normal force (Figure 4(h) - lift stall). Later experiments by McCroskey, et. al.[18] and Carr, et. al.[19] produced data showing the changes in the lift, pitching moment, and flow reversals produced by varying the flow Reynolds number, mean angle of attack, airfoil leading edge geometry, and the airfoil oscillation frequency and amplitude. Their flow reversal measurements made at the airfoil surface are of interest in this discussion. A typical result is presented in Figure 5. The horizontal axis represents nondimensional chord, while the vertical axis represents the phase and magnitude of the sinusoidal variation of angle of attack. The symbols located near a phase of $\pi/4$ represent the start of reversed flow prior to flow separation. The symbols near a phase of $5\pi/4$ represent the reattachment of the boundary layer to the airfoil surface. These investigators also reported that boundary layer separation occurred initially near the trailing edge for the unmodified NACA 0012 airfoil. A modification to decrease the radius of the airfoil leading edge caused separation to initially occur much closer to the leading edge.

Airfoil motion was produced in a different manner with the experimental apparatus described by Rebont, Maresca, Favier and Valensi.[20] They oscillated the airfoil fore and aft in translation at a fixed angle of attack in steady flow. For angles of attack above the steady flow stall angle, their results showed strong unsteady effects on the skin friction. The chronology of the

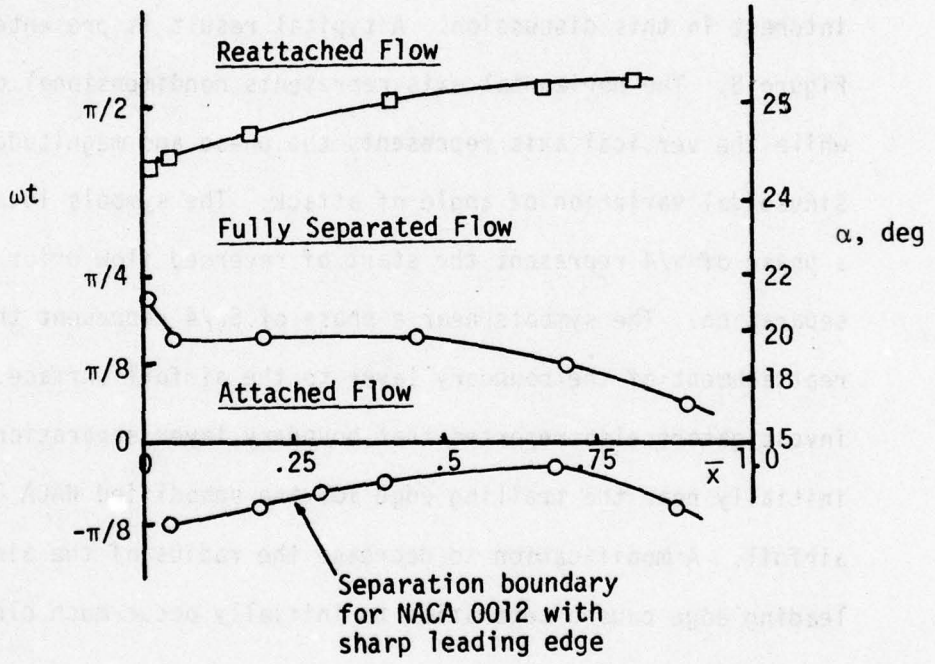


Figure 5
FLOW REVERSAL ON OSCILLATING NACA 0012 AIRFOIL
(reference 3)

dynamic stall events observed was similar to the results obtained for the airfoil oscillating in pitch.

1.4 Optimization of Oscillating Free Stream

The presence of higher harmonic content in the power spectrum of the free stream velocity was observed to produce large unsteady effects in the response of the flow reversal region. In order to reduce these effects, a preliminary experiment was conducted concerning the harmonic optimization of the unsteady velocity oscillations. The wind tunnel modification described below was specifically designed to produce a sinusoidal perturbation to the mean velocity which was free from unwanted higher harmonic effects. A set of rotating vanes at the downstream end of the test section was designed to periodically block the flow to the axial flow fan located further downstream. A nearly constant air flow was provided to the fan by a bypass mechanism which allowed the fan to operate at a nearly constant pressure rise, improving the harmonic suppression in the flow. It was found that this harmonic suppression could be optimized for the various combinations of velocity oscillation amplitude and frequency used in this experiment.

Several experiments in wind tunnels at other institutions have used the rotating vane principle to perturb the flow. Two similar tunnels made no attempt to improve the suppression of higher harmonics. An apparatus on an open-circuit wind tunnel described by Despard[21] used four rotating vanes downstream of the test section to produce velocity variations of up to 40 percent at oscillation frequencies of up to 240 Hz. The second and third harmonics

contributed 23 percent and 4 percent of the velocity power spectrum, respectively. An almost identical apparatus was described by Morkovin, Loehrke, and Fejer[22] which perturbed the flow in a closed-circuit wind tunnel. Resonances were developed corresponding to the tunnel circuit length and also to the distance between the rotating vanes and the tunnel contraction and honeycomb. Large departures from sinusoidality were noted for large velocity oscillation amplitudes. Recent work in this tunnel by Saxena, Fejer, and Morkovin[1] showed plots of the velocity and pressure fluctuations which indicate a higher harmonic content in the pressure fluctuation than in the longitudinal velocity variation.

Several different schemes have been tried to eliminate higher harmonic content in the velocity oscillations of these rotating-vane tunnels, Karlsson[5] used four rotating vanes downstream of the test section of an open-circuit wind tunnel to produce root-mean-square velocity variations of 34 percent of vane rotation frequencies of up to 48 Hz. At high frequencies the higher harmonics were responsible for about 15 percent of the total root-mean-square amplitude of the fluctuation. In an effort to reduce these harmonics, the lowest vane was turned at a higher rate, but no mention is made of the success of this device. Simpson[15] described an apparatus of this type which used five rotating vanes downstream of the test section of an open-circuit tunnel. A programmable motor was used to adjust the angular velocity of the rotating vanes, thereby optimizing the higher harmonic suppression. The resulting velocity waveforms appeared sinusoidal, but no harmonic analysis was presented.

An interesting variation to the rotating vane device was described by Charnay and Mathieu.[23] Their eight rotating vanes were positioned in the settling chamber ahead of the screens and honeycomb sections and upstream of the test section of the open-circuit wind tunnel. They found that the smallest harmonic content occurred when the vane vortex-shedding frequencies matched the tunnel resonant frequencies. Turbulent velocities were measured to evaluate the effect of the upstream-mounted vanes. It was observed that optimum sinusoidality was indicated by maxima of the magnitudes of the longitudinal and vertical turbulent fluctuating velocities, u_1' and u_2', and also by minima of the skewness and flatness factors of u_1'. The turbulence intensity in the test section downstream of the vanes was measured to be on the order of 0.7 percent.

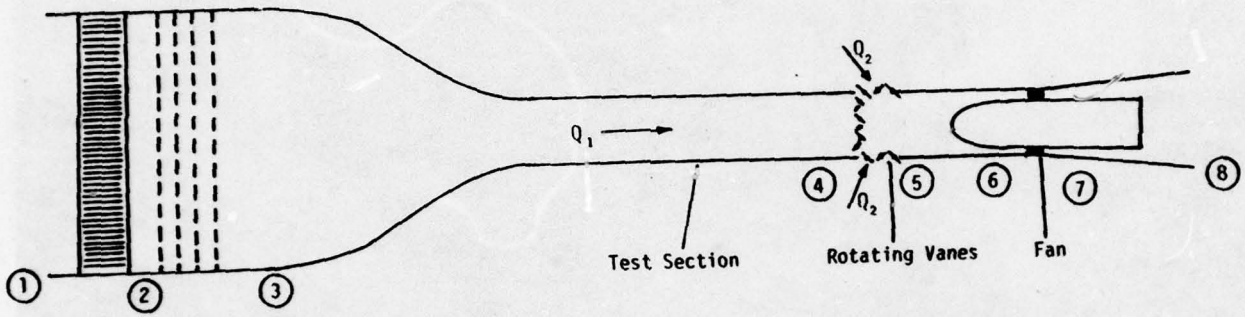
The rotating vane apparatus described below was capable of higher harmonic suppression to a greater degree than the devices described above, with the possible exception of the device described by Simpson.[15] Careful adjustment of the bypass massflow provided regulation of the higher harmonics in the test section for a given tunnel mean velocity and vane rotation frequency. Depending on the vane size and flow conditions, the second harmonic power amplitude could be suppressed as much as 50 db.

2. EXPERIMENTAL APPARATUS AND PROCEDURE

2.1 Unsteady Wind Tunnel Configuration

This experiment was conducted in the two foot by two foot (0.61 meter by 0.61 meter) cross-section low speed wind tunnel at the University of Colorado. It was an open return suction-type wind tunnel with the addition of the unsteady flow apparatus. The unmodified steady flow facility was described in detail by Francis.[24] The wind tunnel schematic is shown in Figure 6. Upstream of the test section were located a plenum with a hexagonal honeycomb, four screens, and a sixteen-to-one area contraction. The test section was 14 feet (4.27 meters) in length with a 10 foot (3.05 meter) long plexiglass wall of 1/2 inch thickness and is shown in Figures 7 and 8. Downstream of the test section were the unsteady flow device, a transition section to the fan, the fan, and the conical diffuser.

A periodic disturbance to the mean flow was produced by a set of six rotating vanes located just downstream of the test section. Figure 9 shows these vanes from upstream in a position of partial flow resistance. Three sets of vanes of varying width were used during this experiment to change the amount of maximum tunnel blockage and thus the velocity amplitude variation, N. The vanes are described in Table 1 below and also in Figure 10. They were made in a modified diamond shape, both for ease of construction and for minimal pressure and friction losses.



Note: Labeling of tunnel stations and mass flow rates corresponds to terms defined in Appendix B

Figure 6
SCHEMATIC OF WIND TUNNEL

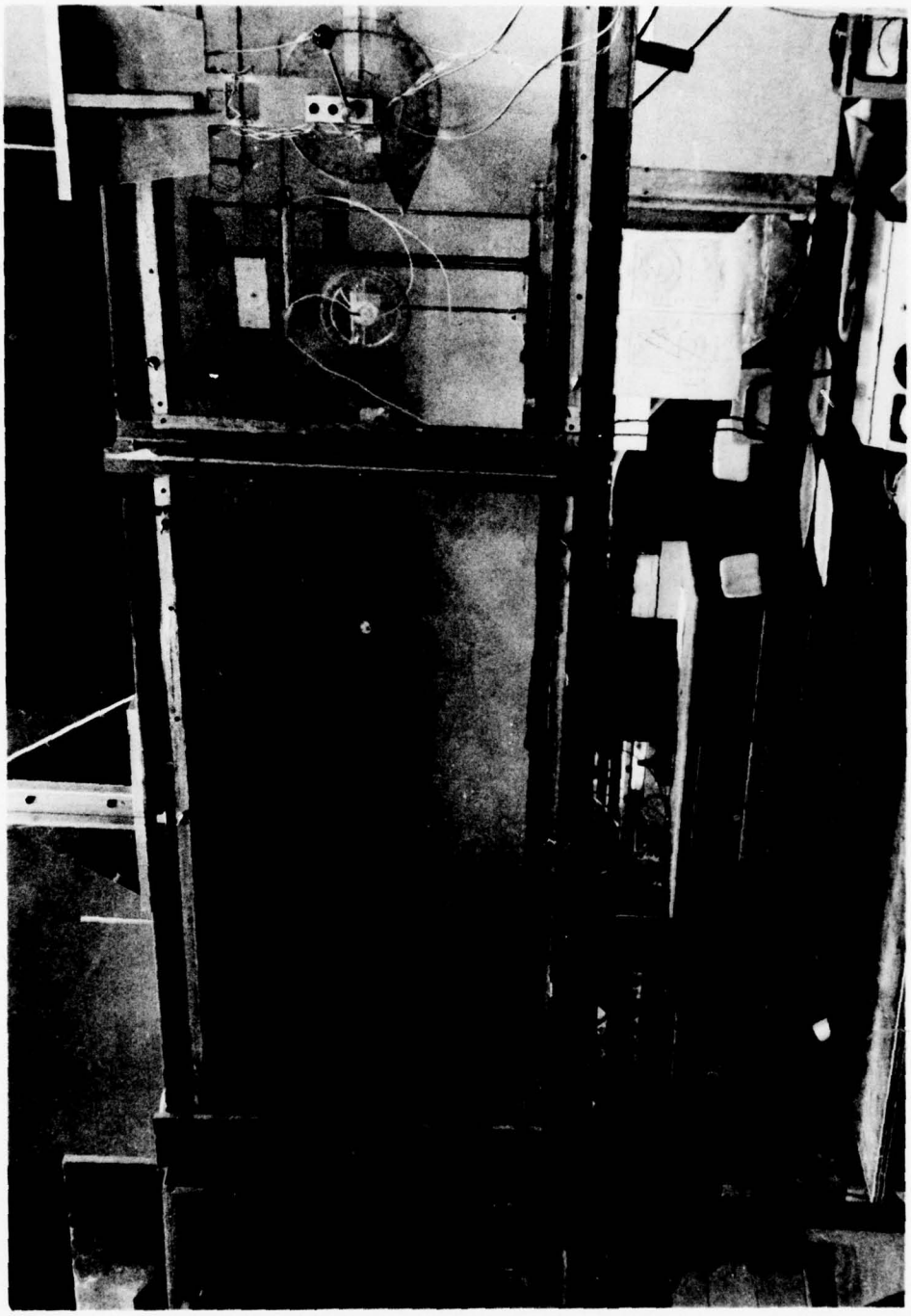


Figure 7
WIND TUNNEL TEST SECTION

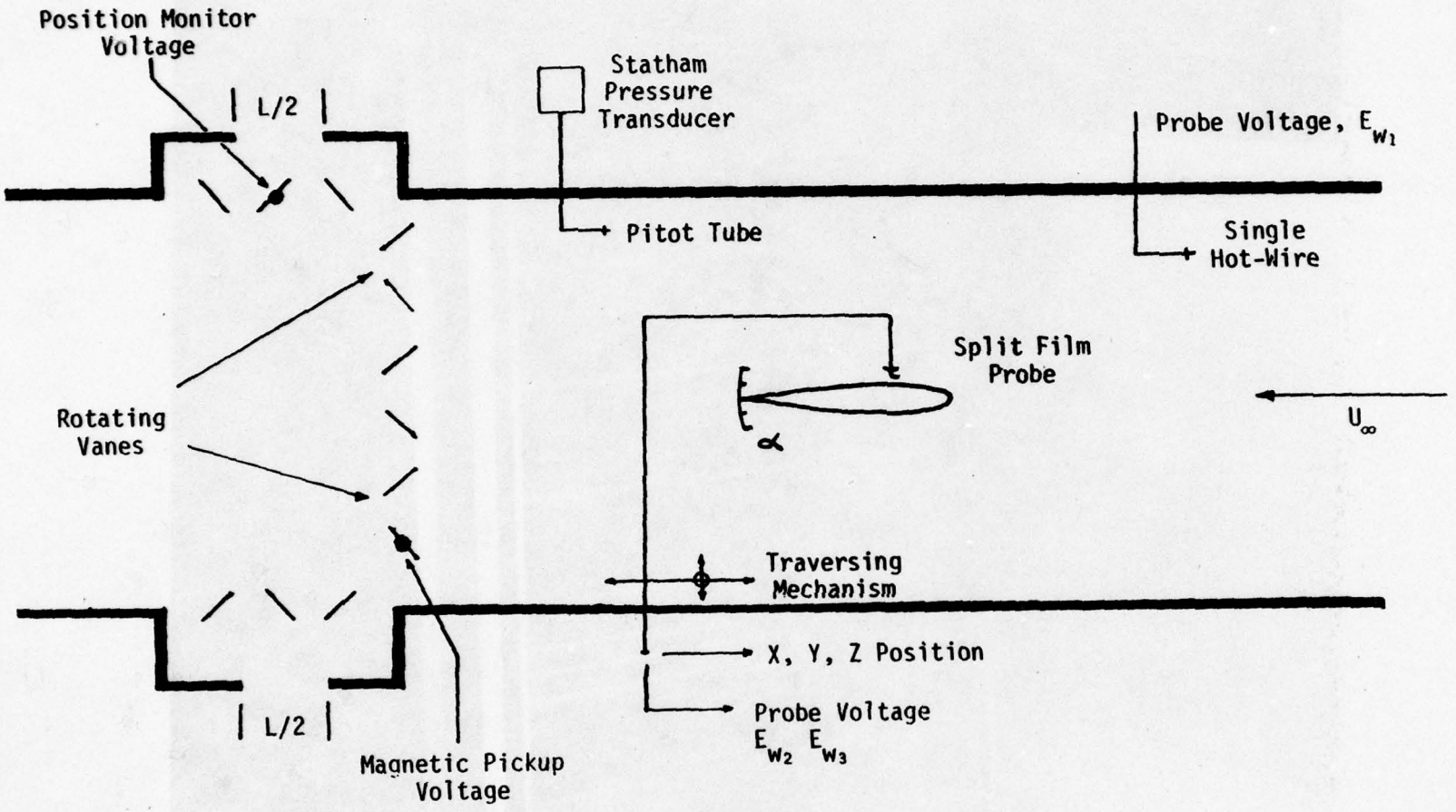


Figure 8
TEST SECTION SCHEMATIC

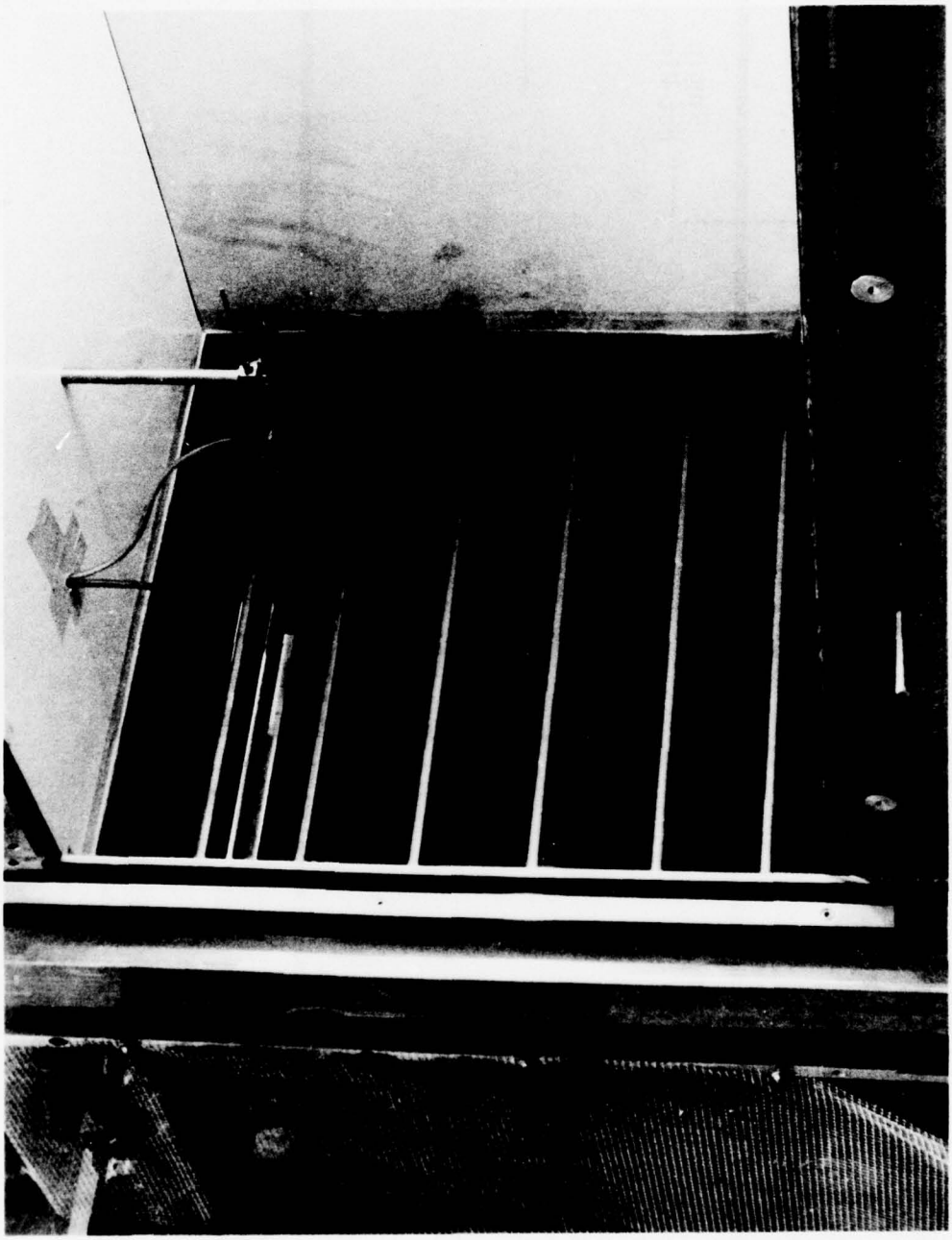
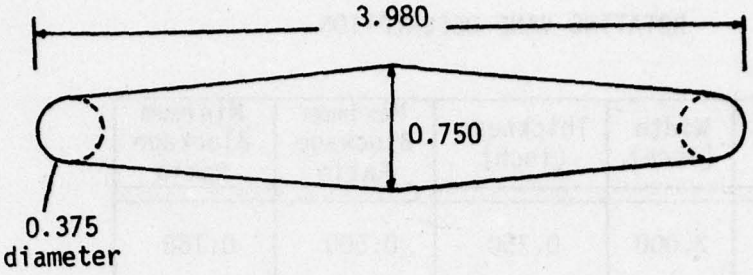
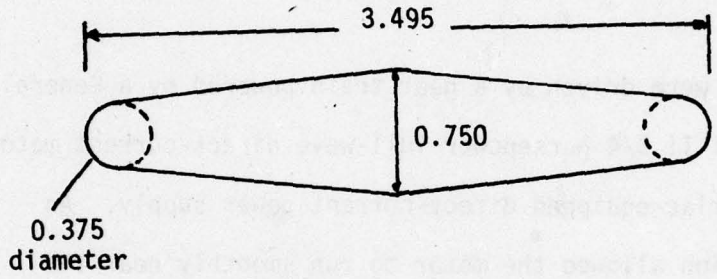


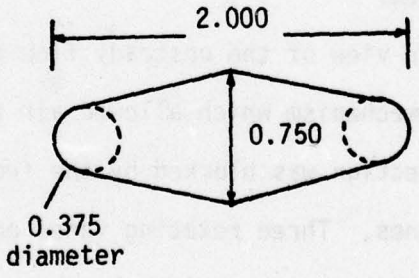
Figure 9
ROTATING VANES



SET C - Large Vane



SET B - Medium Vane



SET A - Small Vane

Figure 10
ROTATING VANE GEOMETRY
(dimensions in inches)

TABLE I

ROTATING VANE DESCRIPTION

Vane Set	Width (inch)	Thickness (inch)	Maximum Blockage Ratio	Minimum Blockage Ratio
Set A (small)	2.000	0.750	0.500	0.188
Set B (medium)	3.495	0.750	0.874	0.188
Set C (large)	3.980	0.750	0.995	0.188

The rotating vanes were driven by a gear train powered by a General Electric Stratitrol II 3/4 horsepower full-wave direct-current motor controlled by a Variac-equipped direct-current power supply. An 8-to-1 gear reduction allowed the motor to run smoothly near the middle of its 0-1759 revolution-per-minute speed range which prevented surging at low speeds. The gear drive was designed to allow the vanes to counter-rotate and, thus, produced no net local lift perturbation to the flow.

Figure 11 shows a top view of the unsteady flow generator. This view shows the bypass mechanism which allowed air to enter the fan section when the test section was blocked by the front, or free stream-controlling, vanes. Three rotating vanes on the top of the device and three on the bottom were driven by the same gear train which also drove the front vanes. The vanes on the top and bottom allowed air from the laboratory to enter the fan section at a varying rate which balanced the disturbance in the test section. The adjustment of the bypass air flow into the fan section was

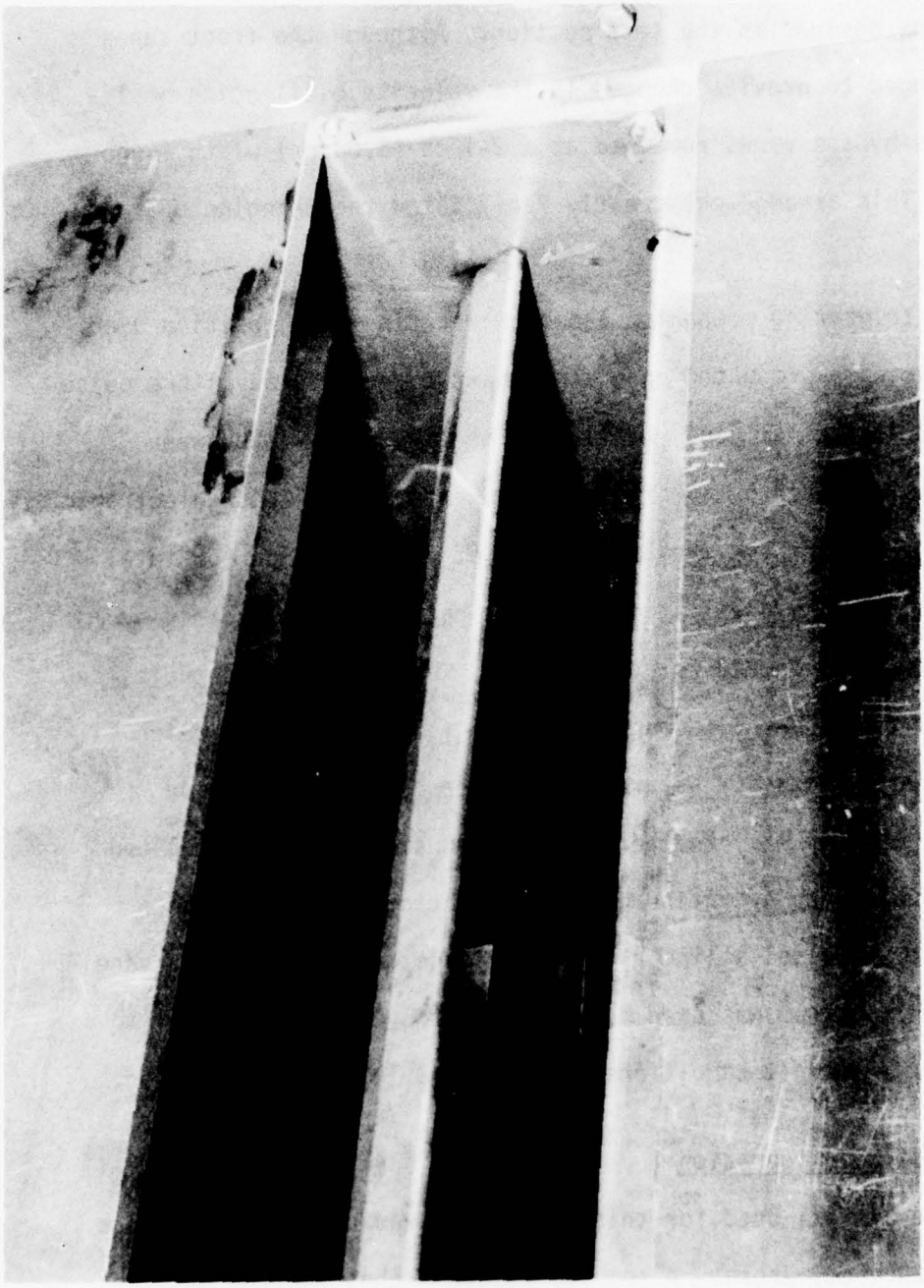


Figure 11
BYPASS VANES AND ADJUSTABLE VANES

controlled by moveable slides which are shown in Figure 11. These slides were set to predetermined bypass openings based on the flow conditions desired in the test section. Although the front vanes were changed to provide changes in the velocity oscillation amplitude, the bypass vanes remained at a 2-inch (5.08 cm) width (vane set A). This arrangement greatly facilitated the changing of vane sets.

A triggering mechanism based on rotating vane position used a magnetic pickup mounted on a vane shaft to produce a voltage pulse every 180 degrees of vane rotation. The time interval between pulses was measured by a Computer Measurements model 605A electronic counter. This enabled the half-period of vane rotation (or total period of velocity oscillation) to be monitored and regulated by adjustments of the vane rotation speed. Monitoring of the velocity oscillation period showed an accuracy of $\pm$ 0.005 seconds, which represented a frequency accuracy of 1.4 percent at a rotation frequency of 1.43 Hz. Another circuit, consisting of a regulated voltage applied to a continuous-turn potentiometer mounted on a vane shaft, provided a linear output voltage corresponding to vane angle. This output was used to align the front vanes parallel to the flow when steady conditions were desired in the test section.

2.2 Airfoil Configuration

The airfoil used for this experiment was a NACA 0012 with a 10 inch (25.4 cm) chord. A span of 23.900 inches (60.706 cm) left a gap of 0.050 inches (0.127 cm) between the wing and each side wall. The solid wing was milled from 7075-T7 aluminum to a $\pm$ 0.002 inch (0.005 cm) tolerance over the entire profile. The wing was supported

at the quarter chord on pins which protruded through oversized holes in the wind tunnel walls. The pins were supported from outside the tunnel on ball-bearings by a U-shaped frame placed across the I-beams which formed the top of the test section. This support served to isolate the airfoil from deflections of the test section side walls caused by the unsteady flow.

The airfoil angle of attack was measured by aligning a line scribed along the airfoil centerline with a leveled protractor attached to the plexiglass test section wall. Parallax errors were minimized by always sighting the angle of attack from the airfoil trailing edge, giving values of angle of attack accurate to within $\pm$ 0.2 degrees.

2.3 Velocity Measurements

Free stream velocity measurements were made using a constant-temperature hot-wire anemometer circuit designed by Bank[25] and shown in Figure 12. The anemometer output voltage, E, can be related to the free stream velocity using King's law:[26]

$$E^2 - E_o^2 = BU_\infty^n,$$

where E_o is a constant voltage level.

An analog circuit, shown in Figure 13, utilized Motorola MC1594 multipliers to linearize the anemometer output. Data collected by Francis[24] in this facility validated the use of this apparatus by showing that the exponent "n" was very close to 0.5 and that the coefficient B was a constant for flow experiments of this type using air and hot-wire probes of this type. It was also

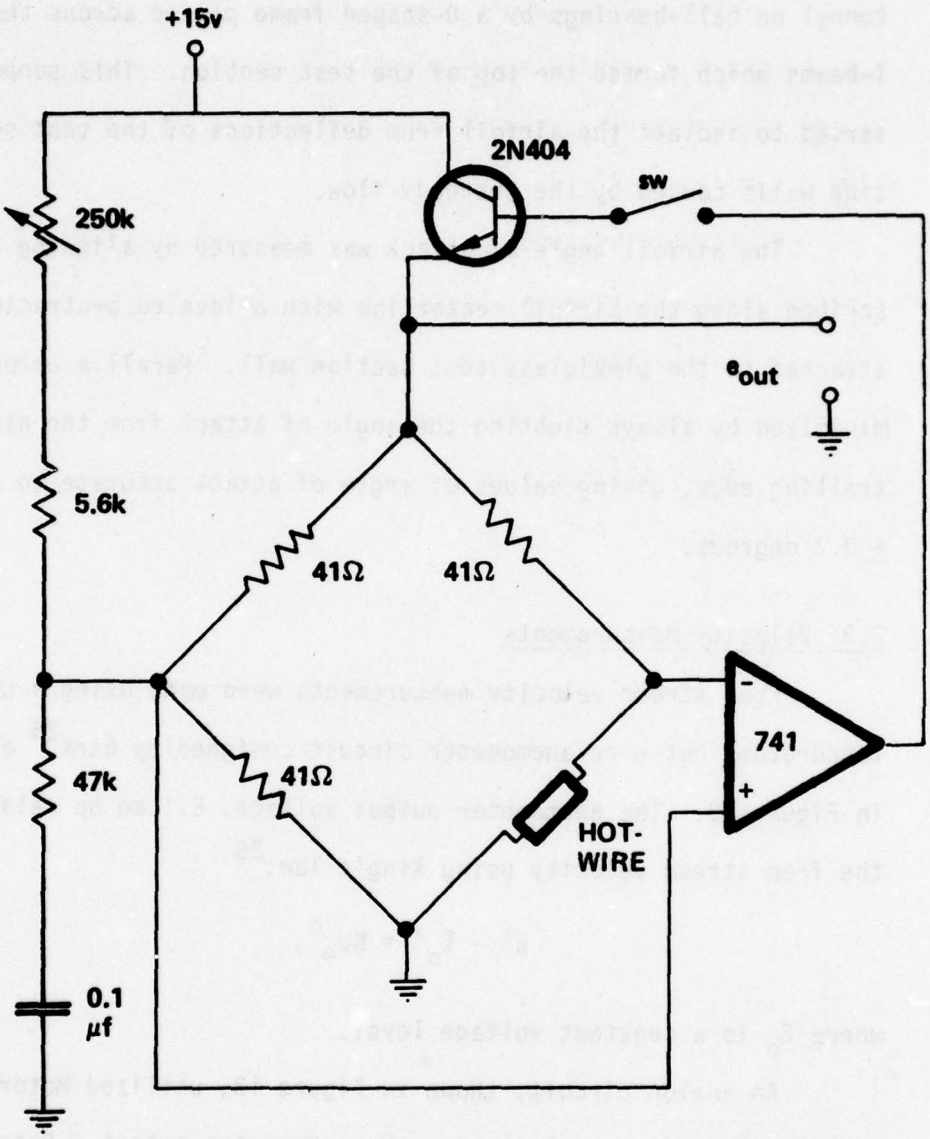


Figure 12
HOT-WIRE ANEMOMETER

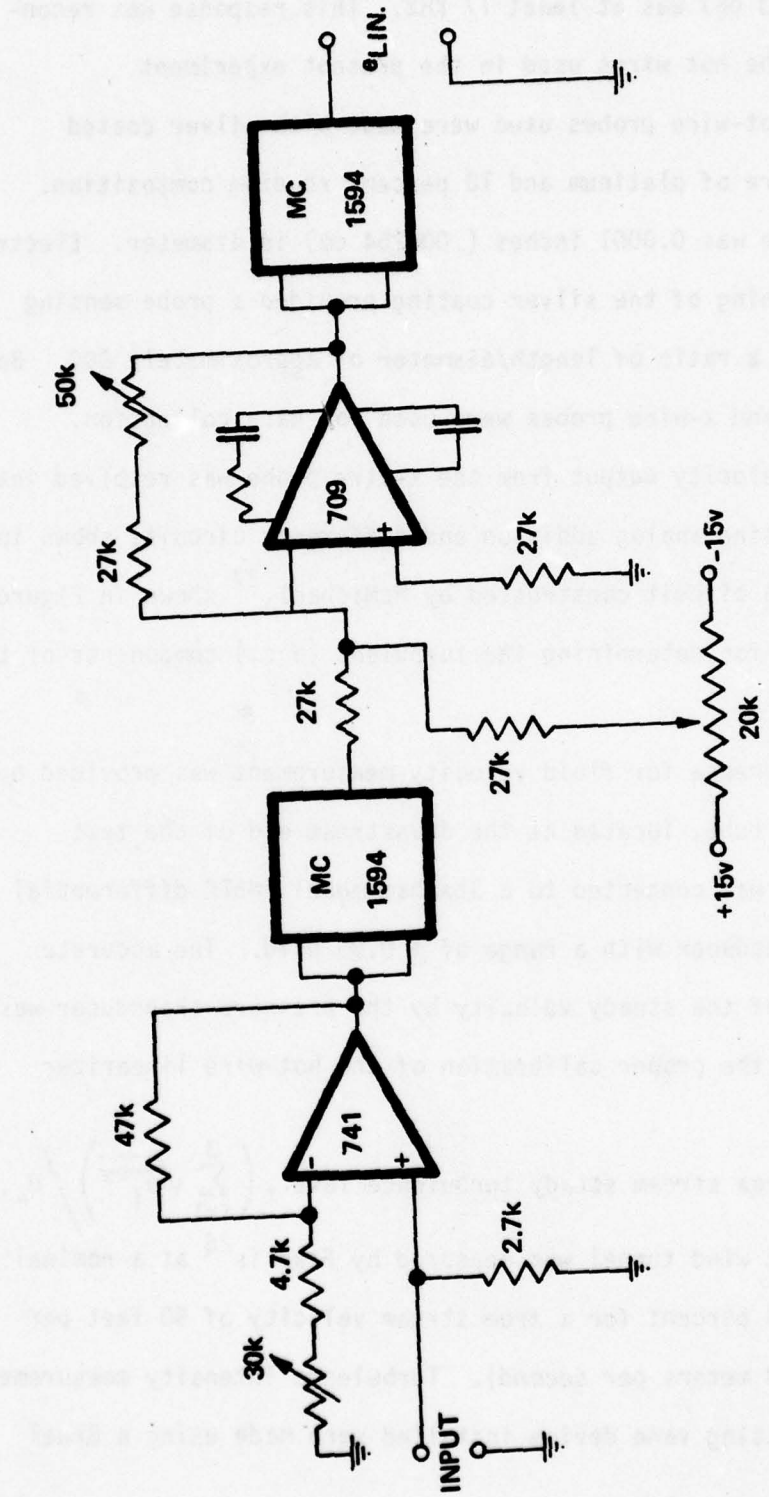


Figure 13
LINEARIZER CIRCUIT

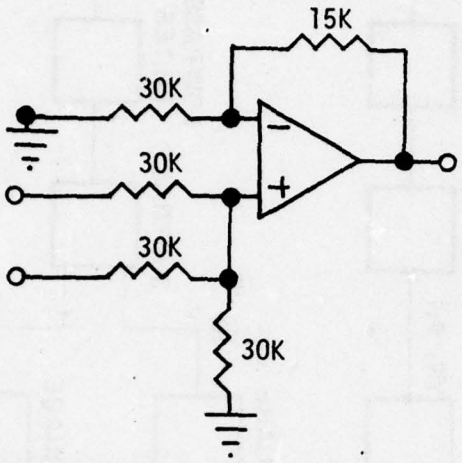
shown, using a square wave test, that the anemometer frequency response ($\pm$ 3 db) was at least 17 KHz. This response was reconfirmed for the hot wires used in the present experiment.

The hot-wire probes used were made with silver coated Wollaston wire of platinum and 10 percent rhodium composition. The wire core was 0.0001 inches (.000254 cm) in diameter. Electrochemical etching of the silver coating provided a probe sensing element with a ratio of length/diameter of approximately 300. Both single-wire and x-wire probes were used for data collection. Linearized velocity output from the x-wire probe was resolved into components using analog addition and difference circuits shown in Figure 14. A circuit constructed by McMichael,[27] shown in Figure 15, was used for determining the turbulent (a.c.) components of the x-wire signals.

A reference for fluid velocity measurement was provided by a pitot static tube, located at the downstream end of the test section. It was connected to a Statham model PM5TC differential pressure transducer with a range of $\pm$ 0.05 psid. The accurate measurement of the steady velocity by the pressure transducer was essential to the proper calibration of the hot-wire linearizer output.

The free stream steady turbulence level, $\left(\sum_{i=1}^{3} \sqrt{\overline{u_i'^2}}\right) \Big/ U_\infty$, for the basic wind tunnel was measured by Francis[26] at a nominal value of 0.06 percent for a free stream velocity of 60 feet per second (18.29 meters per second). Turbulence intensity measurements with the rotating vane device installed were made using a Bruel

Averaging Circuit



Difference Circuit

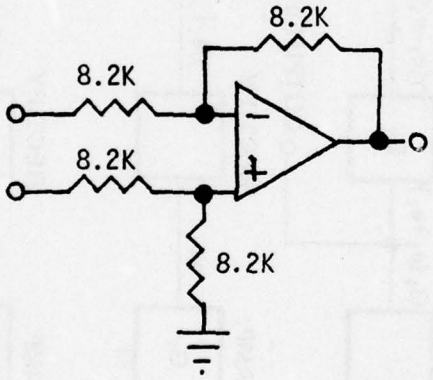


Figure 14
ANALOG CIRCUIT COMPONENTS

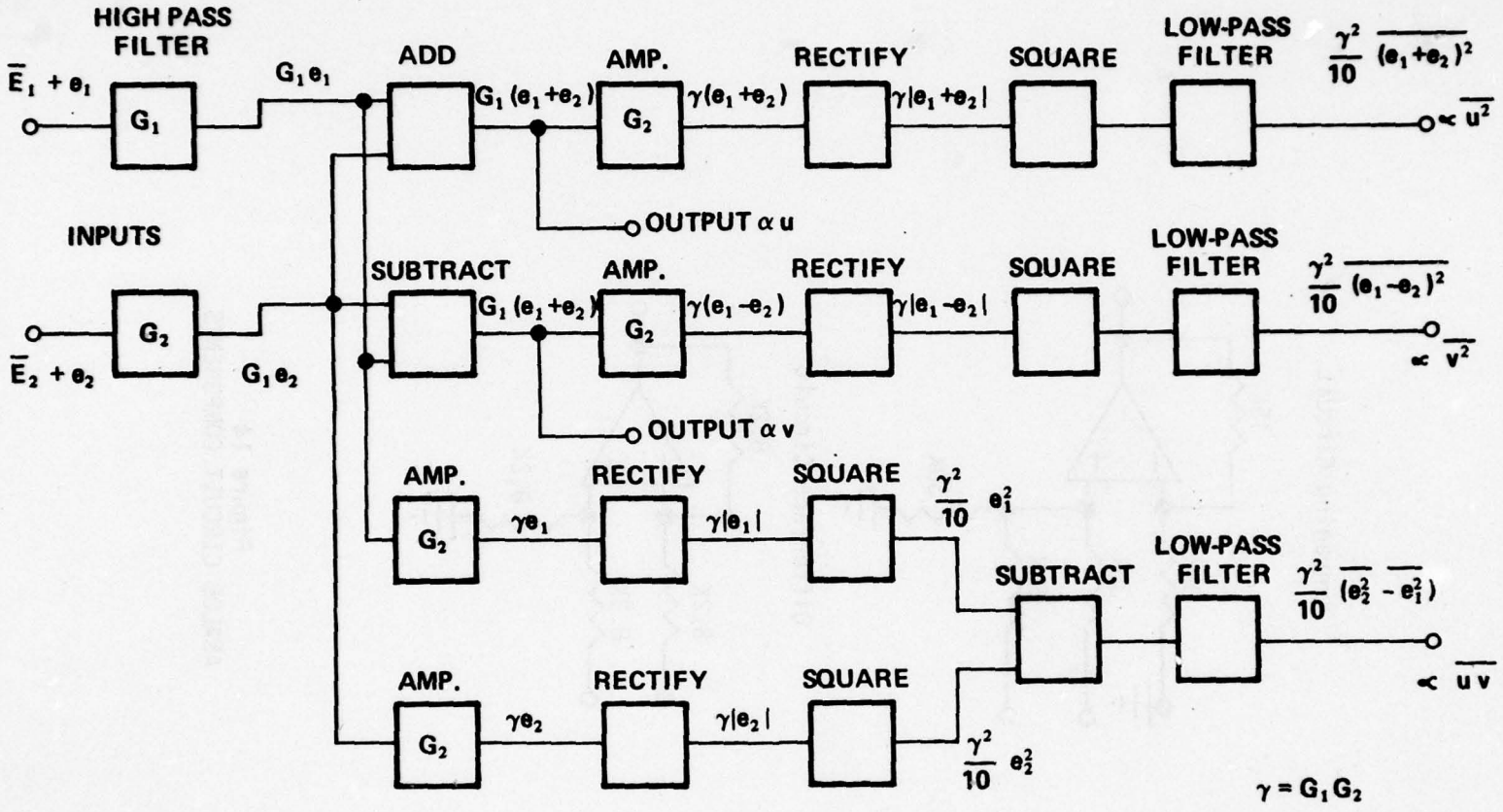
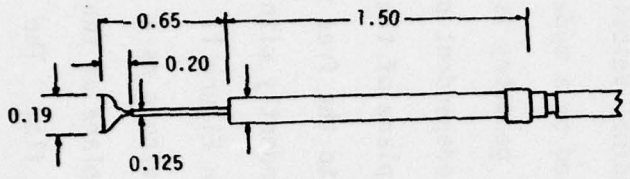


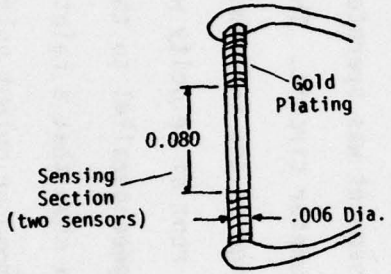
Figure 15
A.C. SIGNAL CONDITIONER

and Kjaer type 2417 Random Noise Voltmeter which had a bandwidth of 2-20,000 Hz. With the large front vanes (set C) fixed at the minimum resistance (full open) position, the steady flow turbulence level was measured to be 0.08 percent at a free stream velocity of 60 feet per second (18.29 meters per second). The vanes were then rotated at 3.33 Hz and the turbulence level was measured to be 0.54 percent at a mean flow velocity of 12 feet per second (3.66 meters per second). To determine the effect of unsteadiness on the higher frequency turbulence, this velocity data signal was filtered through a 4 Hz high-pass filter. The higher frequency root-mean-square turbulence level was then measured to be 0.05 percent.

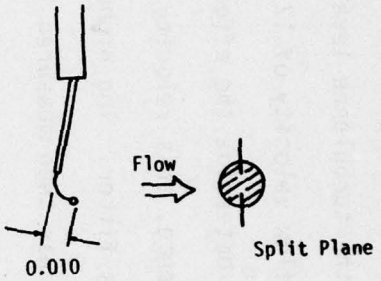
Reversals in flow direction of the longitudinal velocity component in the airfoil boundary layer were sensed by a model 1287V split film sensor made by TSI, Inc.[28] The sensor geometry is shown in Figure 16. In this design, two electrically independent platinum films were plated on a single quartz fiber. The plane of the split between the two films was oriented perpendicular to the free stream direction. Each film segment was operated independently with a separate hot-wire anemometer circuit. The data in Figure 17 show the square of the average of the two anemometer outputs as a function of the square root of velocity with the plane of the split between the probes aligned parallel to the steady flow. The linearity of these data show that a relationship similar to King's law exists between anemometer output voltage and velocity. The exact formulation of this relation may be somewhat altered from King's law, but the linear approximation shown in Figure 17 is sufficient over the velocity range measured in this experiment.



Probe



Sensor



Sensor Orientation

Figure 16
SPLIT FILM SENSOR AND PROBE DETAIL
(distances in inches)
(reference 28)

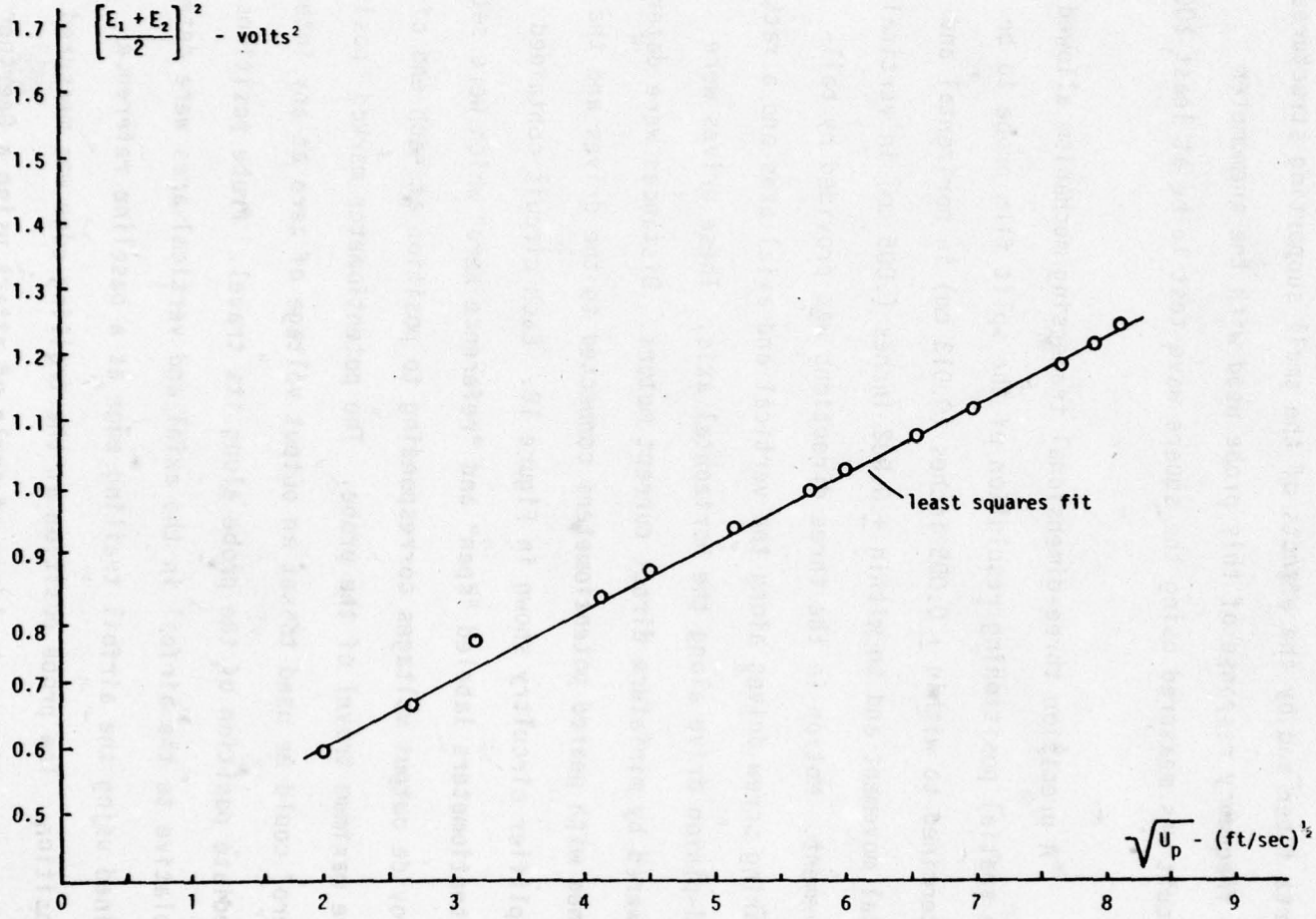


Figure 17
SPLIT FILM PROBE OUTPUT (Split Aligned with Flow)

Measurements by TSI, Inc.[28] showed this probe to be very insensitive to errors caused by both fluid velocities along the axis of the quartz fiber and by the effects of the small supporting structures. The frequency response of this probe used with the anemometer circuit was measured using the square wave test to be at least 200 Hz.

A precision three-dimensional traversing mechanism allowed the spatial positioning resolution of the split film probe to be determined to within $\pm$ 0.005 inches (0.013 cm) in horizontal and axial movement and to within $\pm$ 0.002 inches (.005 cm) in vertical movement. Motion in the three directions was provided by ball-bearing screw drives along the vertical and axial axes and a rack-and-pinion drive along the horizontal axis. These drives were powered by miniature direct current motors. Distances were determined with geared potentiometers connected to the drives and the amplifier circuitry shown in Figure 18. Each circuit contained potentiometers labeled "span" and "reference zero" which were set to provide output voltages corresponding to position at each end of the maximum travel of the probe. The potentiometer marked "position zero" could be used to set an output voltage of zero at any intermediate position of the probe along its travel. Probe positions relative to the airfoil in the axial and vertical axes were determined using the airfoil trailing edge as a baseline reference position. The probe position at the trailing edge was measured optically after each change of angle of attack using a Gaertner optical cathotometer. The distances of the probe vertically above the airfoil surface and horizontally along the chord during data

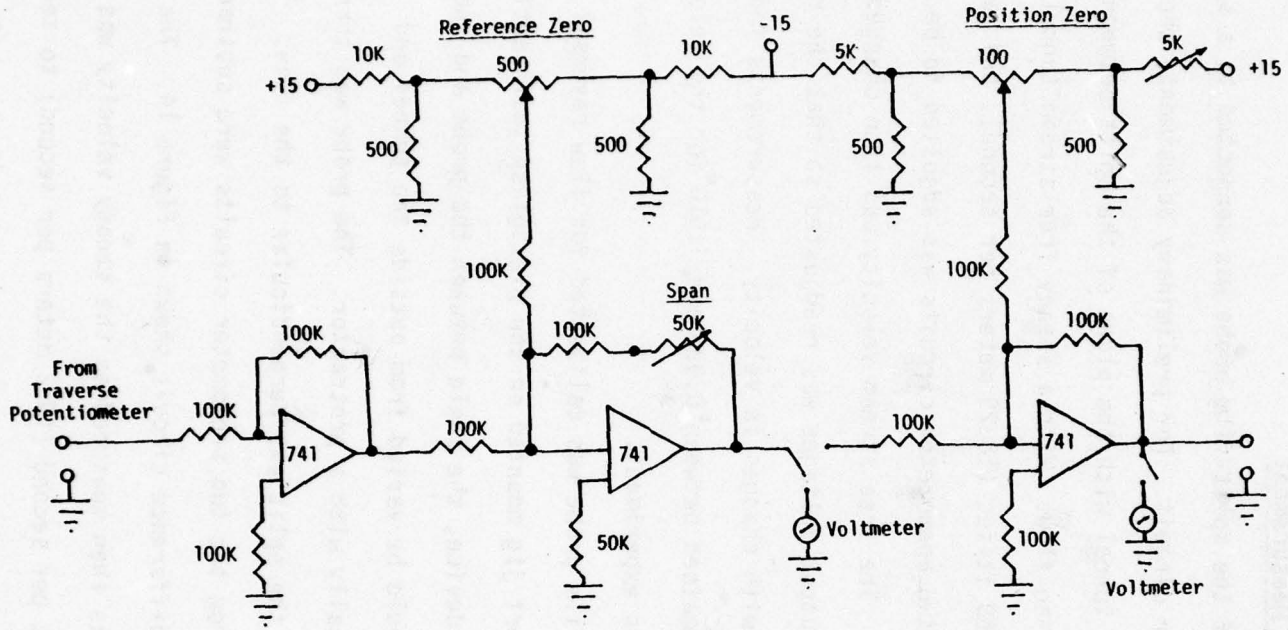


Figure 18
TRAVERSE POSITIONING CIRCUIT

collection were then computed using programs for a Texas Instrument TI-58 programmable calculator which are shown in Appendix A.

2.4 Flow Reversal Measurement

Each film of the split-film probe was connected to a separate hot-wire anemometer circuit. For preliminary adjustment, the probe was mounted in the tunnel with the plane of the split between the films parallel to the flow. With a steady free stream tunnel velocity of about 60 ft/sec (18.29 meters per second), the ratio of the output of the two anemometer circuits was adjusted to be approximately one. The free stream velocity was then changed and the ratio of the output voltages was readjusted so that the ratio remained constant with changes in velocity. Measurements indicated that this ratio remained between 0.990 and 1.010 for the velocities encountered in this experiment.

The split-film probe was calibrated for flow reversal indication using a support jig mounted on the plexiglass test section wall. Using this device, the angle between the probe and the free stream velocity could be varied from outside the tunnel and measured geometrically with a protractor. The probe was turned so that the plane of the split was perpendicular to the flow. The output voltages from the two anemometer circuits were subtracted using the analog difference circuit shown in Figure 14. The output of this circuit was then measured as the steady velocity was varied from about 60 feet per second (18.3 meters per second) to zero feet per second. This procedure was then repeated with the probe turned 180 degrees. A sample calibration curve of the difference circuit

voltage as a function of steady velocity is shown in Figure 19. Flow reversal was attributed to a voltage level of 0.49 volts for this calibration. The probe was then mounted on the traverse mechanism and was calibrated for forward velocities only. The data shown in Figure 19 show that the threshold voltage indicating flow reversal remained essentially the same when the probe was moved from the jig to the traverse. This threshold voltage was not zero, since the ratio of the anemometer output voltages set above, with the plane of the splits parallel to the flow, was never exactly equal to one. This threshold reversal voltage was rechecked prior to data collection and showed excellent repeatability. The total drift of the reversal threshold voltage was observed to be $\pm$ .05 volts over seven consecutive days of data collection. The probe response shown is non-linear since the linearizer circuits were not used. This was done to improve accuracy, since the low velocities near flow reversal would produce linearizer voltages within the noise levels of the multiplier elements.

The split film probe was used to indicate flow reversal, that is, the point when the sign of the longitudinal velocity becomes negative. The actual magnitude of the reversed velocity was not measured because of the inability of the split film probe to resolve the reversed velocity components accurately. Characteristics provided by the probe manufacturer showed that flows aligned closely with the plane of the split could be accurately resolved into components. However, the measured magnitudes of the components of flows perpendicular to the plane of the split, such as the reversed flows, were shown to be in error by up to 10 percent. For this,

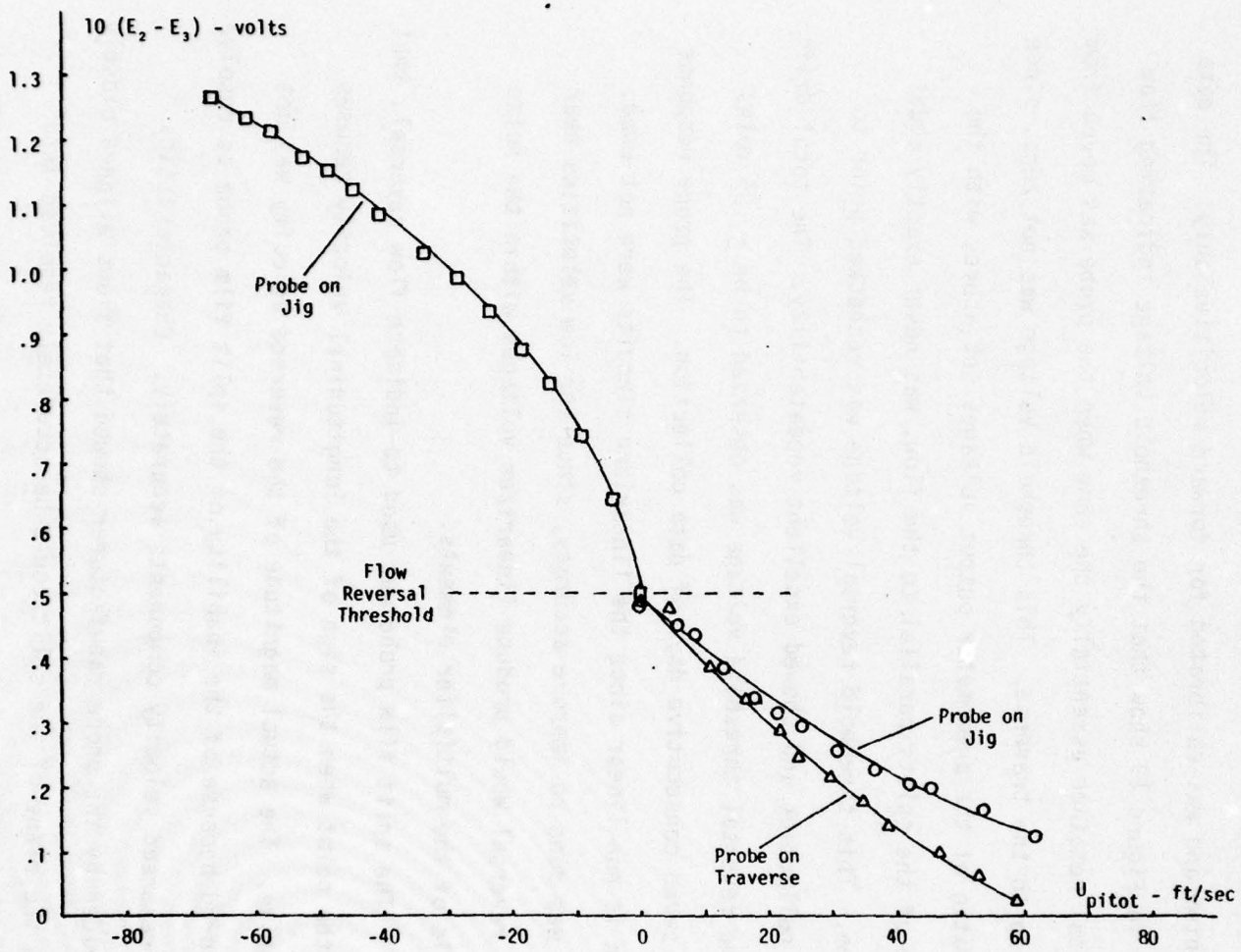


Figure 19
FLOW REVERSAL INDICATION (Split Film Probe)

reason, only the onset of flow reversal was measured. The error band on the probe indication of flow reversal onset depended strongly on the ensemble averaging technique used in this experiment and will be discussed below.

2.5 Data Processing

The complete signal processing apparatus is shown in Figure 20. The heart of the data analysis was a Hewlett-Packard model 5452B Fourier Analyzer System.[29] This device is a digital instrument capable of analysis of analog input data in either the time domain or the frequency domain. The analog input amplitude range extended to 10 volts with a maximum frequency response of 25 KHz. The system included an analog-to-digital converter, a digital computer with an 8192-word memory, and a digital oscilloscope. A hardwired function keyboard was provided to initiate analyzer operations. It was also used for programmable scaling of the digitally converted input and the programming of repetitive operations.

The analog input data was digitized so that each word represented a value of the input at a given point in time for a time domain input, or a value of a spectrum at a given frequency for frequency domain input. Each data word was a 16-bit binary number representing an integer from -32768 to +32767. Groups of data words were collected in data blocks containing a quantity of data words equal to any power of 2 from $2^7 = 128$ to $2^{10} = 1024$. Computer operations were then carried out on the data blocks, in either the frequency or time domain, as appropriate. The sizing of

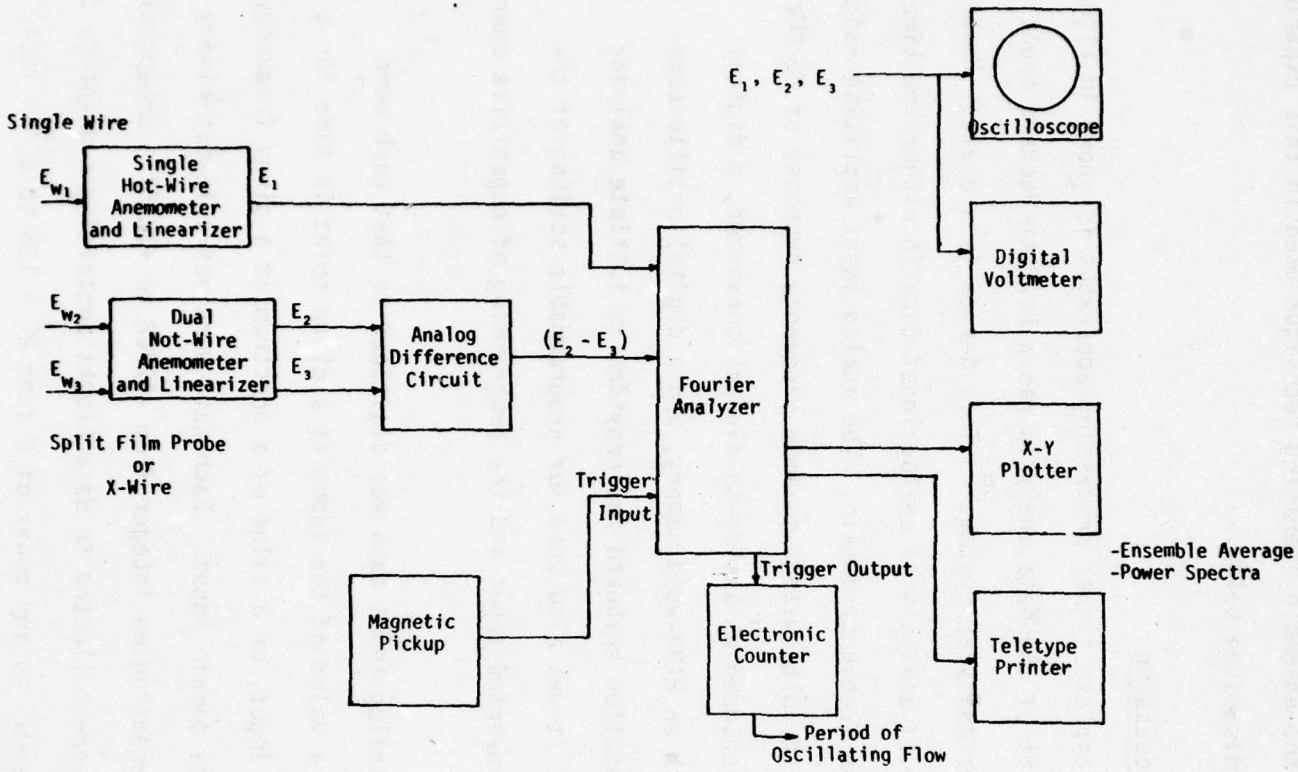


Figure 20
SIGNAL PROCESSING APPARATUS

the data blocks in both domains represented a compromise between the accuracy required and the period of time required to analyze all the data generated by this experiment. In the time domain, the maximum size of the time sample, T, was chosen to be 1.0 seconds and the number of data words in the data block, N, was selected to be 256. This choice allowed the analyzer output to be generated quickly using the relationship

$$T = N[\Delta t].$$

This provided an interval of 0.0039 seconds between time domain data words which was found to give sufficient accuracy. In the frequency domain, the maximum frequency was set at 10 Hz after an inspection of higher frequencies revealed no power spectral data of significance to this experiment (turbulence neglected). Using the same block size of 256 words, the relationship

$$F_{max} = \left[\frac{N}{2}\right]\left[\Delta f\right]$$

showed that the frequency resolution was 0.078 Hz between frequency domain data words. The number of frequency data words per block was N/2, or half the block size, since the frequency information was broken into real and imaginary displays.

An important feature of the Fourier Analyzer was its ability to perform ensemble averages using either time or frequency domain data. The concept of the ensemble average may be understood by considering, for example, velocity measurements taken in the time domain. The velocity ensemble average was determined by averaging over a collection of data blocks, where each block had a common

phase with respect to the varying free stream velocity. The velocity field $U_i(\underset{\sim}{x},t;\ p)$, as a function of a position vector $\underset{\sim}{x}$ and a time t, was given an ensemble counter parameter p. The ensemble average was then:

$$\langle U_i(\underset{\sim}{x},t;\ p)\rangle = \lim_{m\to\infty}\left[\frac{u_i(\underset{\sim}{x},t;\ p_1) + \ldots + u_i(\underset{\sim}{x},t;\ p_m)}{m}\right].$$

Writing the velocity as a mean plus a deviation about a mean:

$$U_i(\underset{\sim}{x},t) = \langle U_i(x,t)\rangle + u_i'(\underset{\sim}{x},t)$$

it can be seen that the process of ensemble averaging eliminates the deviations about the mean, since $\overline{u_i'} = 0$. For this experiment, the number of data blocks, m, used for each ensemble average was chosen to be large enough so that the deviations from the mean tended to zero, but small enough so that the period of time required for data collection was not excessive. Experience showed that ensemble averages of fifty blocks for the flow field analysis were sufficient to separate the mean velocity from the input velocity data. When the flow reversal data was subsequently collected, only twenty data blocks were averaged. The use of this smaller number of blocks reduced the total time required to calculate the many averages necessary to describe the flow. This smaller number was found to be sufficient to eliminate the deviations from the mean. The phase of the data blocks used in averaging was held constant by the trigger mechanism connected to the rotating vanes. The trigger voltage pulse was used to start the input of data into each block.

2.6 Sources of Error

The error band on the flow reversal indication measured by the split film probe depended on the ensemble averaging process. The reversal threshold voltage indicated in Figure 19 is actually an average value based on an ensemble of 20 data blocks. The root-mean-square deviation of the threshold voltages from each block, V_i; from the ensemble averaged threshold voltage of $\langle V \rangle = 0.49$ volts; was determined using the expression

$$\sum_{i=1}^{20} \left[\overline{(V_i - \langle V \rangle)^2} \right]^{\frac{1}{2}} \Big/ V_{average}.$$

For the data used in Figure 19, this root-mean-square error ratio was calculated to be 1.1 percent for an average threshold voltage of 0.49 volts. Through the calibration shown in Figure 18, this corresponds to an error in the reversal velocity of less than one-half foot per second (0.15 meters per second).

In addition to the measurement errors already mentioned, there was some concern over tunnel-induced three-dimensional effects. At high oscillation frequencies, the time-varying velocity due to the large vanes (set C) caused considerable physical deflection of the plexiglass test section wall. Unsteady velocity measurements, made at several spanwise locations in the wing boundary layer, showed that these three-dimensional effects were negligible. The measured vertical and longitudinal velocity components varied by less than $\pm$ 0.2 percent along the wing span outside of the side-wall boundary layer.

Ambient temperature variations were minimized by operating the wind tunnel at or below about 60 feet per second (18.29 meters per second) for at least two hours before starting data collection. This allowed the temperature of the laboratory environment to stabilize at approximately 70 degrees Fahrenheit (21 degrees Celsius). Errors due to electronic drift were then negligible. Calibrations of the hot-wire anemometer system accomplished before and after data collection showed that the changes of the tunnel mean velocity as a function of time were also negligible.

3. UNSTEADY FLOW FIELD HARMONIC OPTIMIZATION

Examination of the unsteady boundary layer equations shows the strong influence of higher harmonics in the free stream velocity on the unsteady flow effects. A detailed presentation and discussion of these equations is given in section 4.2. The goal of the unsteady flow optimization was to provide a longitudinally oscillating velocity at a desired amplitude ratio, reduced frequency, and mean velocity, whose power spectrum was as free as possible of harmonic content. Of the four controllable tunnel parameters, a combination of vane size, tunnel steady velocity, and vane rotation frequency (or rotation period) were selected to give the desired reduced frequency and velocity oscillation amplitude ratio. The upper and lower bypass openings, each at a setting of L/2, were then adjusted for maximum second harmonic suppression. The variable bypass was intended to provide a more uniform flow to the fan over the period of vane rotation. The relationship of the bypass resistance to the tunnel flow resistance is described in the flow analysis by McMichael[30] and summarized in Appendix B. This analysis showed that the smallest temporal change in the pressure rise across the fan occurred when the pressure and frictional losses across the bypass ports and vanes were equal to the sum of the pressure drop across the main tunnel vanes and the frictional losses in the test section. Careful adjustment of the bypass port openings

permitted a fine tuning of the bypass frictional losses and permitted an almost steady flow to reach the fan.

The actual unsteady flow characteristics generated by the smallest set of rotating vanes (set A) can be compared most easily to the analysis because, for this case, the size of the tunnel and bypass vanes were the same. The analysis showed that this arrangement provided a great simplification and, ideally, generated only even harmonics in the oscillating velocity field. The absence of add harmonics was difficult to confirm experimentally since, for the small vanes, usually only the second harmonic was large enough to be detected by the Fourier Analyzer on a logrithmic-magnitude power spectrum (maximum scale of 80 db).

A typical power spectrum of the linearized velocity signal for the small vanes (set A) is shown in Figure 21 for k = 0.873 and L/2 = 1 inch (2.54 cm). The velocity data had been ensemble-averaged over 50 data block entries. The measurements were conducted in an empty test section, without the wing installed. The second harmonic power was observed to be approximately 48 db lower than the power of the fundamental. The db differences between the voltage power levels of the first and second harmonics, $20 \log_{10} (V_1/V_2)$, are plotted in Figure 22 for a variation of L/2 at this flow condition. The optimum or maximum power difference is observed to be approximately 48 db and the smallest difference is 32 db. The power differences between the fundamental and third harmonic and between the fundamental and fourth harmonic were also noted, if measurable. In no case were they measured to be less than 60 db and 70 db respectively for the small vanes.

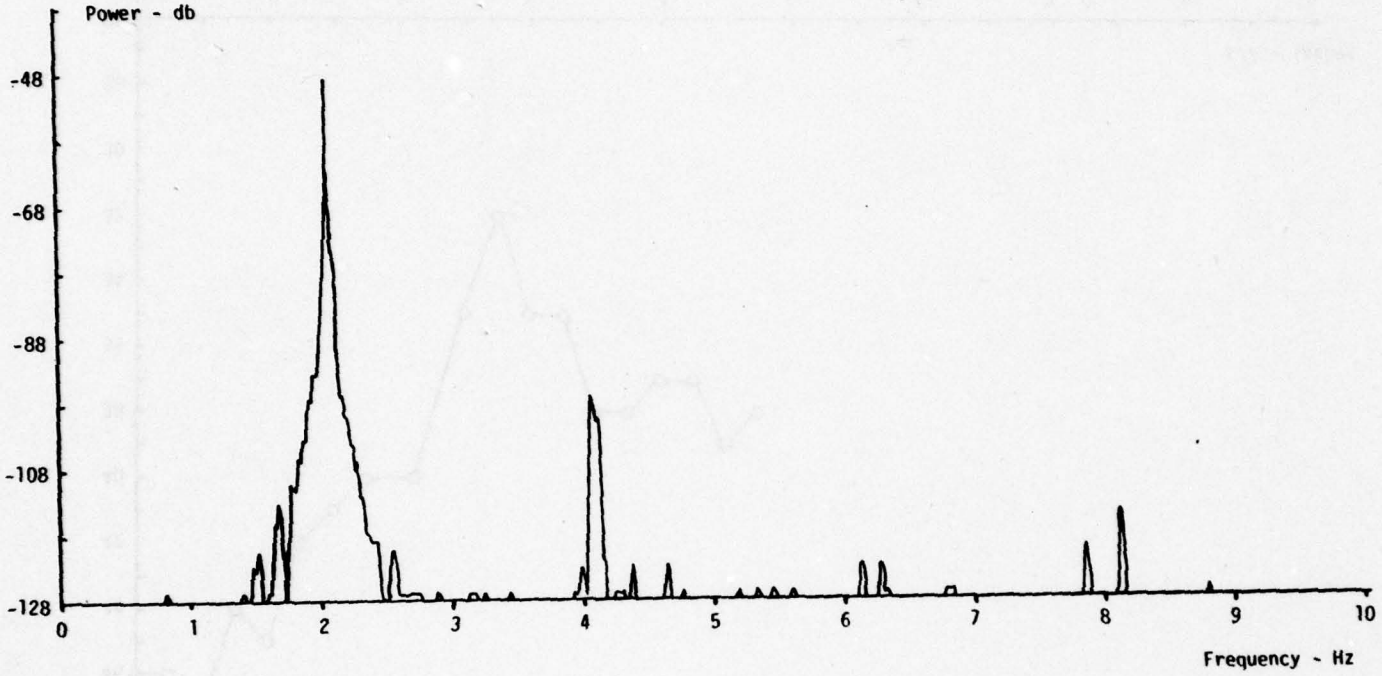


Figure 21
POWER SPRCTRUM (AC)
Small Vanes (set A)
k = 0.0873 (2 Hz)

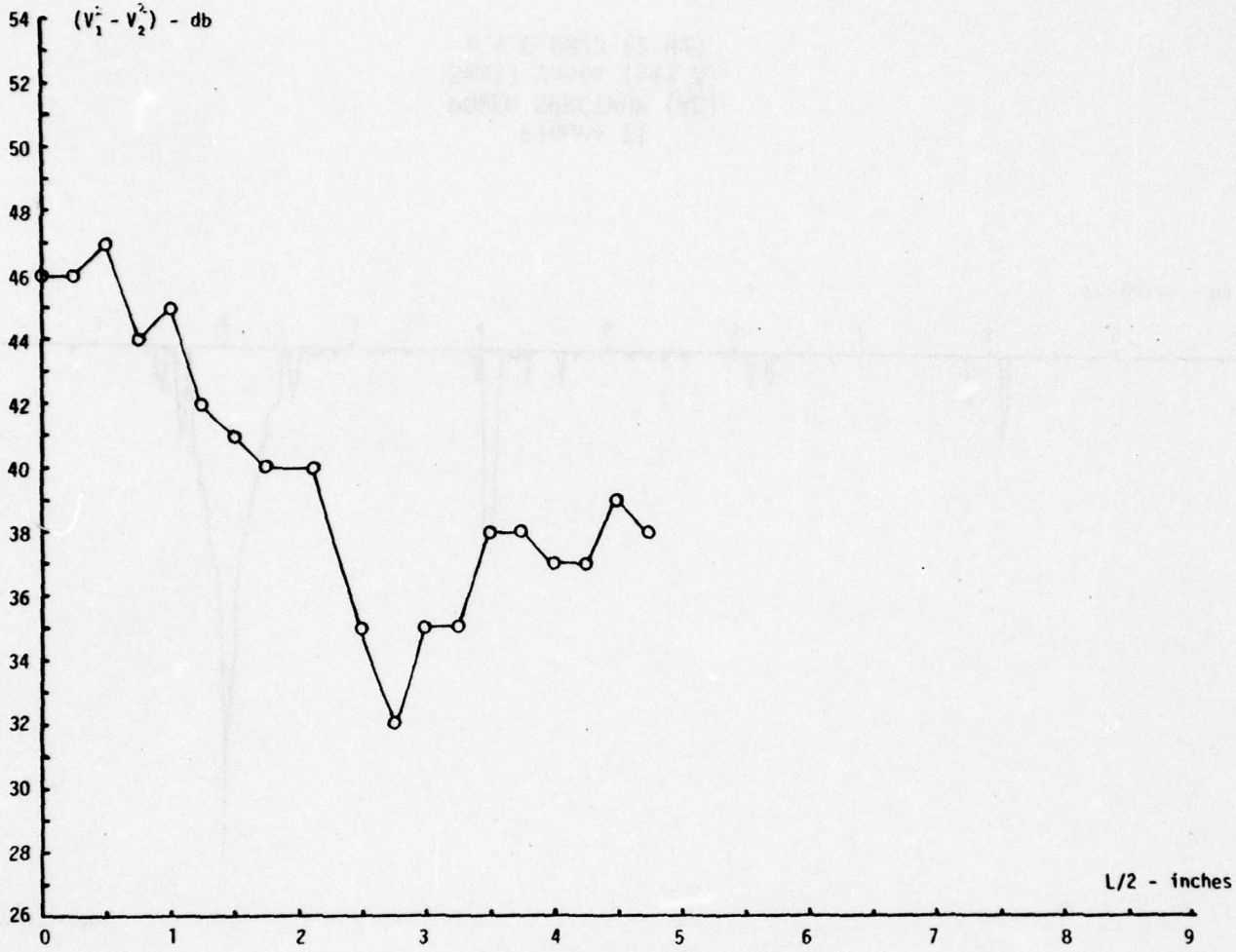


Figure 22
DIFFERENCE IN FIRST AND SECOND HARMONIC POWER LEVELS
Small Vanes (set A), k = 0.0873 (2 Hz)

The power spectrum results for the larger vane sets were acceptable, but not as free from harmonics as those for the smallest vanes. The power differences between the fundamental and second harmonic as functions of L/2 are presented in Figure 23 for the medium vanes (set B) and a mean velocity of 31 feet per second (9.45 meters per second) and in Figure 24 for the large vanes (set C) and a mean velocity of 12 feet per second (3.66 meters per second). These data were collected with the airfoil installed in the test section. At these flow conditions, the medium and large vane sets were observed to produce maximum harmonic differences of 15 db and 11 db, respectively. The maxima can be clearly distinguished, but they are not as large in magnitude as those measured with the small vane set (set A) installed. It must be remembered that, for mechanical simplicity, only the main-flow vanes were replaced when changing vane sets. The bypass vanes were not replaced. This arrangement greatly complicated the flow analysis, and the relationships developed in Appendix B do not clearly show that a maximum exists for the second harmonic suppression. The experimental results show that, even with different sizes of main and bypass vanes, the maxima can be achieved with the proper setting of L/2.

In order to obtain the parameters required for the flow reversal experiments, the optimum setting of L/2 could not always be used. The objectives of the flow reversal experiments required two separate parametric variations of the flow. The first varied the reduced frequency and held the mean velocity and oscillation amplitude nearly constant. The second varied the oscillation

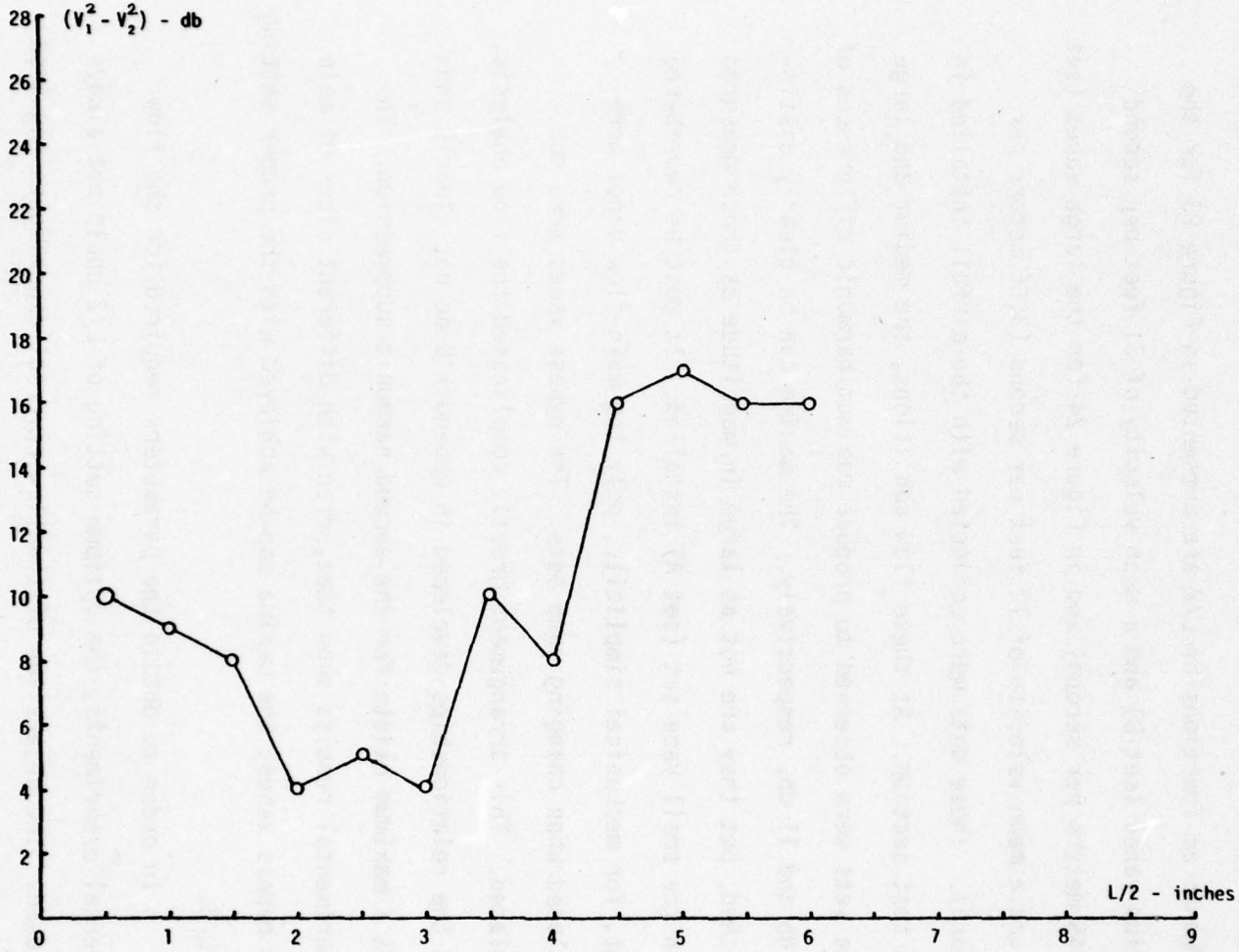


Figure 23
DIFFERENCE IN FIRST AND SECOND HARMONIC LEVELS
Medium Vanes (set B)

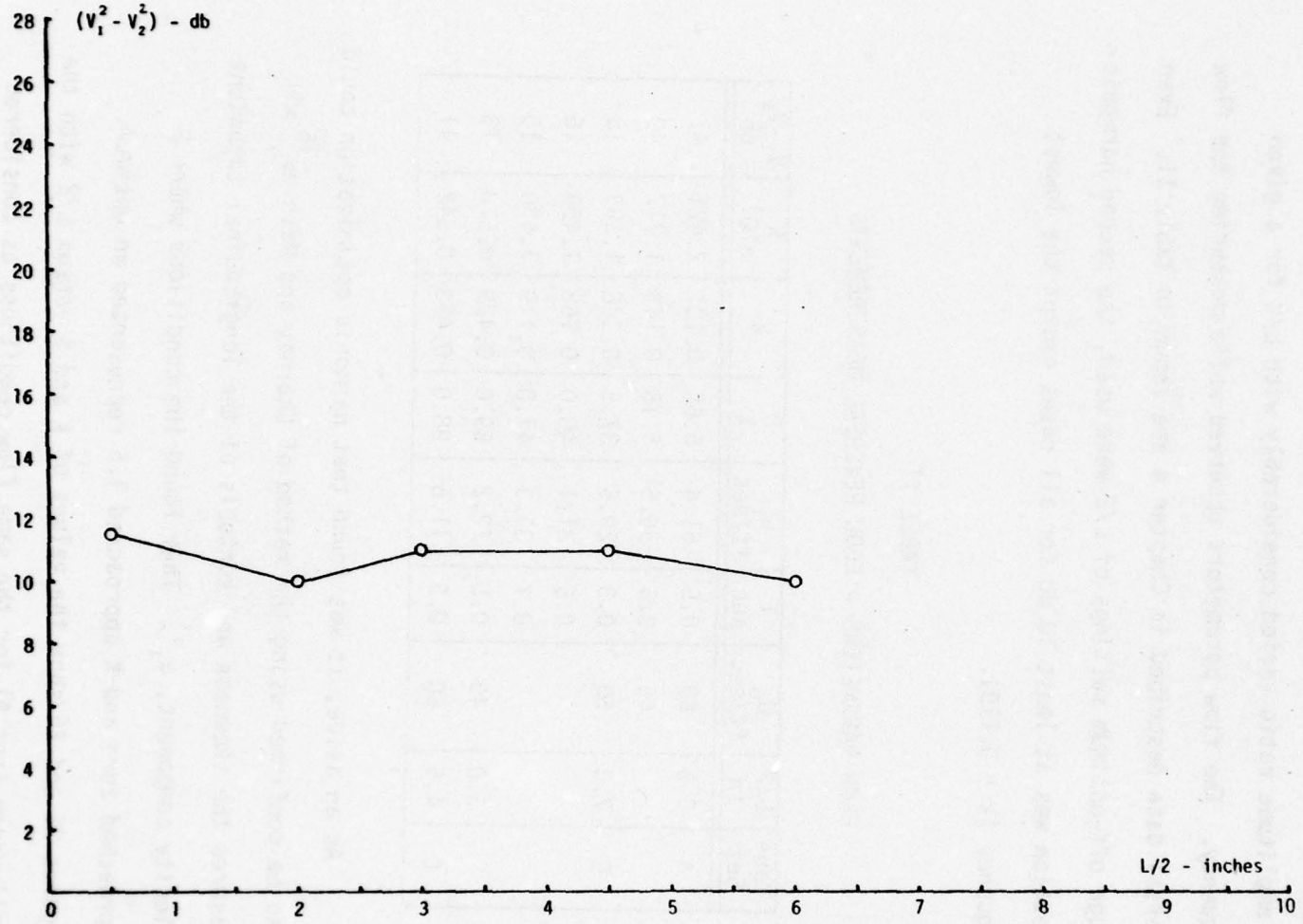


Figure 24
DIFFERENCE IN FIRST AND SECOND HARMONIC LEVELS
Large Vanes (set C)

amplitude, with the reduced frequency and mean velocity almost constant. It was observed that the magnitudes of the mean velocity and amplitude ratio varied considerably with L/2 for a given frequency. The flow parameters observed while measuring the flow reversal data described in Chapter 4 are shown in Table II. Even though off-optimum settings of L/2 were used, the second harmonic rejection was at least 10 db for all cases except the lowest frequency (k = 0.119).

TABLE II

FLOW PARAMETERS - FLOW REVERSAL MEASUREMENTS

Vane Set	L/2 in	U_o ft/sec	T sec	U_1 ft/sec	N %	k	R $x10^5$	V_1-V_2 db
A	0.5	60	0.5	51.6	5.65	0.101	2.421	47
		45	0.5	36.6	5.15	0.143	1.717	49
B	7.0	60	0.3	29.5	37.5	0.296	1.383	18
			0.5	31.1	40.0	0.168	1.459	16
			0.7	31.3	47.0	0.119	1.470	10
	3.0	40	0.5	12.2	59.0	0.429	0.570	13
C	4.5	60	0.5	11.6	98.0	0.453	0.542	11

As an aside, it was found that harmonic optimization could also be confirmed using the method of Charnay and Mathieu[16] who measured the skewness and kurtosis of the longitudinal turbulent velocity component, u_1'. They found the conditions where S approached zero and K approached 1.5 represented an optimum. Figures 25 and 26 show the values of K and S versus L/2 with the small vanes (set A) for the same flow conditions as considered above. It can be seen that the optimum values of L/2 are the same

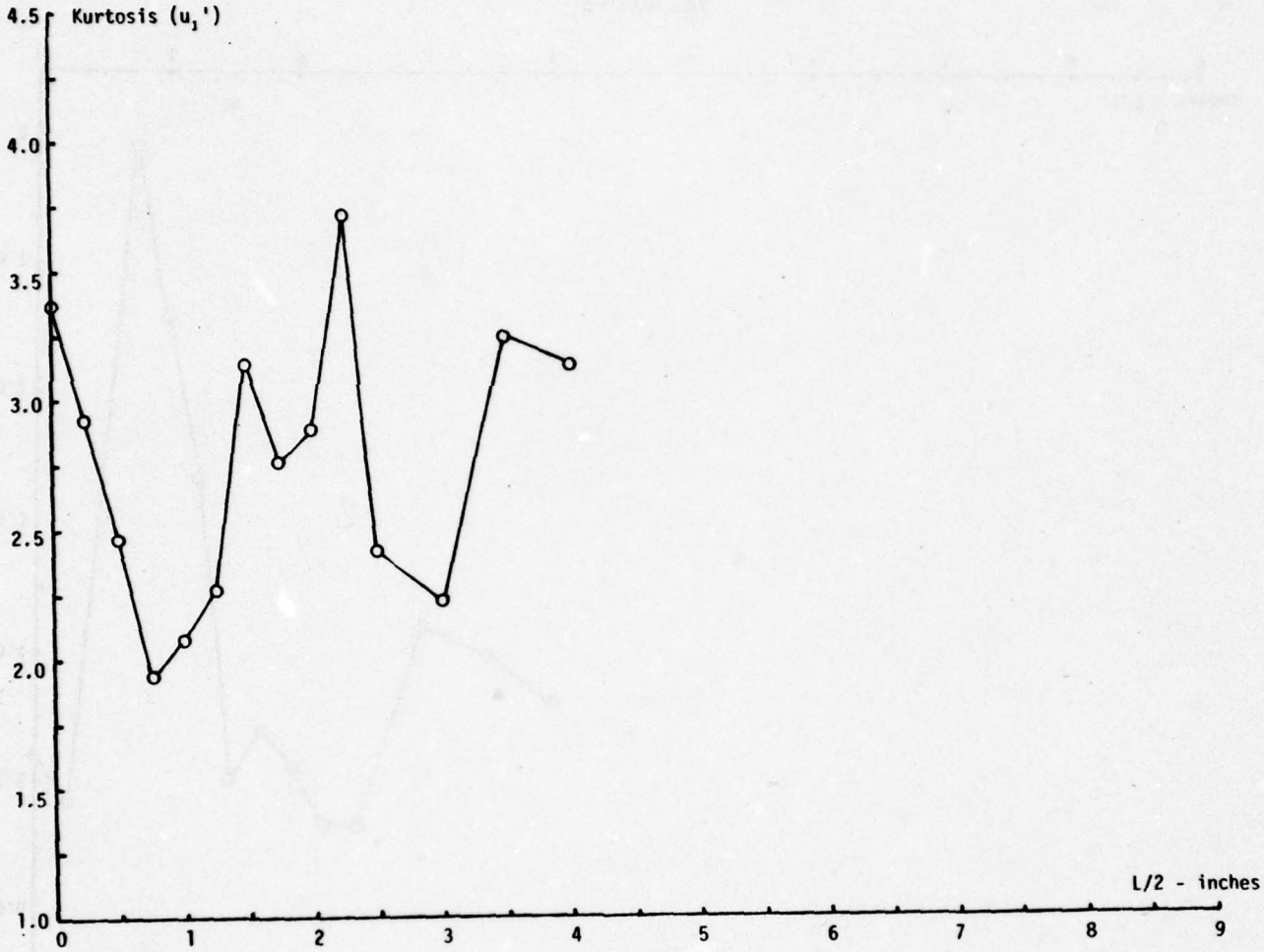


Figure 25
KURTOSIS OF u_1' (k = 0.0873)

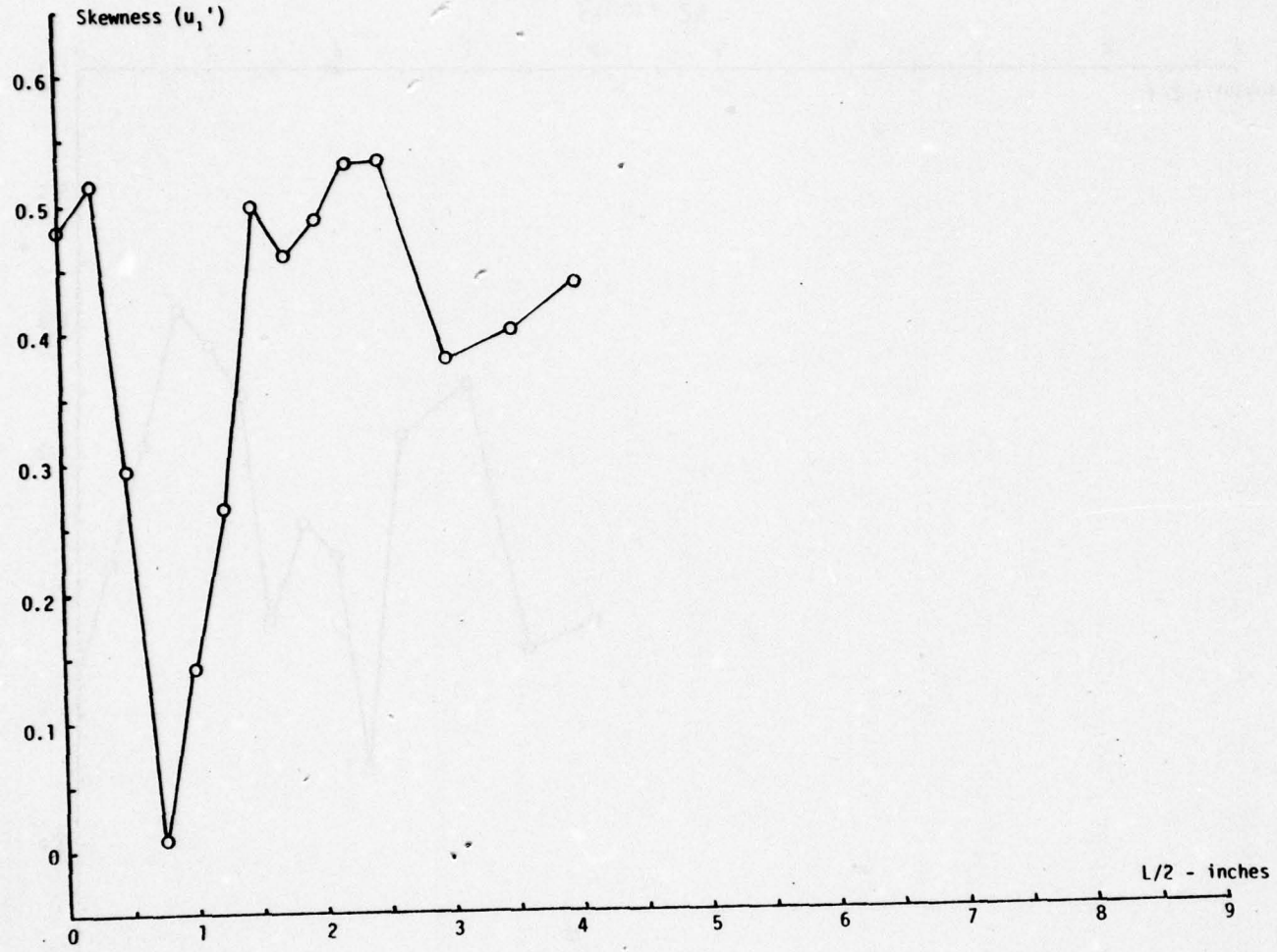


Figure 26
SKEWNESS OF u_1' (k = 0.0873)

as predicted by the spectral analysis. Also, the points of maximum S and K correspond to the points of minimum harmonic suppression. The zero value of S indicates that the distribution of the velocity harmonics is Gaussian and that the disturbance caused by the vanes only affects the pressure field. The low value of K shows that the u_1' distribution is broad for the optimized tunnel condition.

4. RESULTS AND DISCUSSION OF FLOW REVERSAL MEASUREMENTS

4.1 Steady Flow Boundary Layer Reversal

Boundary layer flow reversal was measured for a variety of steady flow conditions prior to examining the unsteady case. The steady data were considered to be the zero-frequency limit of the unsteady flow measurements. These regions of reversed flow, which occurred near the airfoil leading edge, represented the lower portion of the so-called laminar separation bubble. A model of this bubble is presented in Figure 27 taken from reference 31. This region of separated flow is caused by the large curvature of the airfoil surface near the leading edge. After the laminar boundary layer separates, it transitions to turbulent flow and then reattaches to the airfoil surface. The dividing streamline shown in Figure 27 defines the boundaries of the recirculating region contained in the bubble. Flow reversal measurements obtained in this experiment determined the position of the reversal boundary shown in the figure. Previous data[20] for the NACA 0012 airfoil have shown a separation bubble from the leading edge to approximately twenty percent chord at an angle of attack of 11 degrees and a Reynolds number of 250,000.

A typical steady flow reversal observed in this experiment is shown in Figure 28. The vertical axis represents the non-dimensional height of the sensor above the airfoil surface and the horizontal

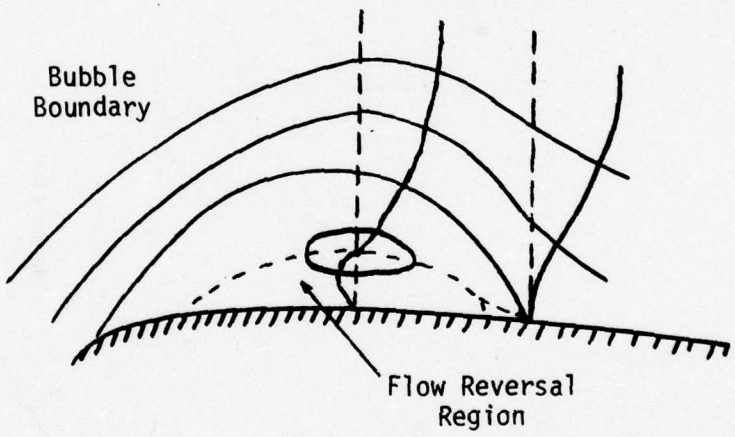


Figure 27
LAMINAR SEPARATION BUBBLE

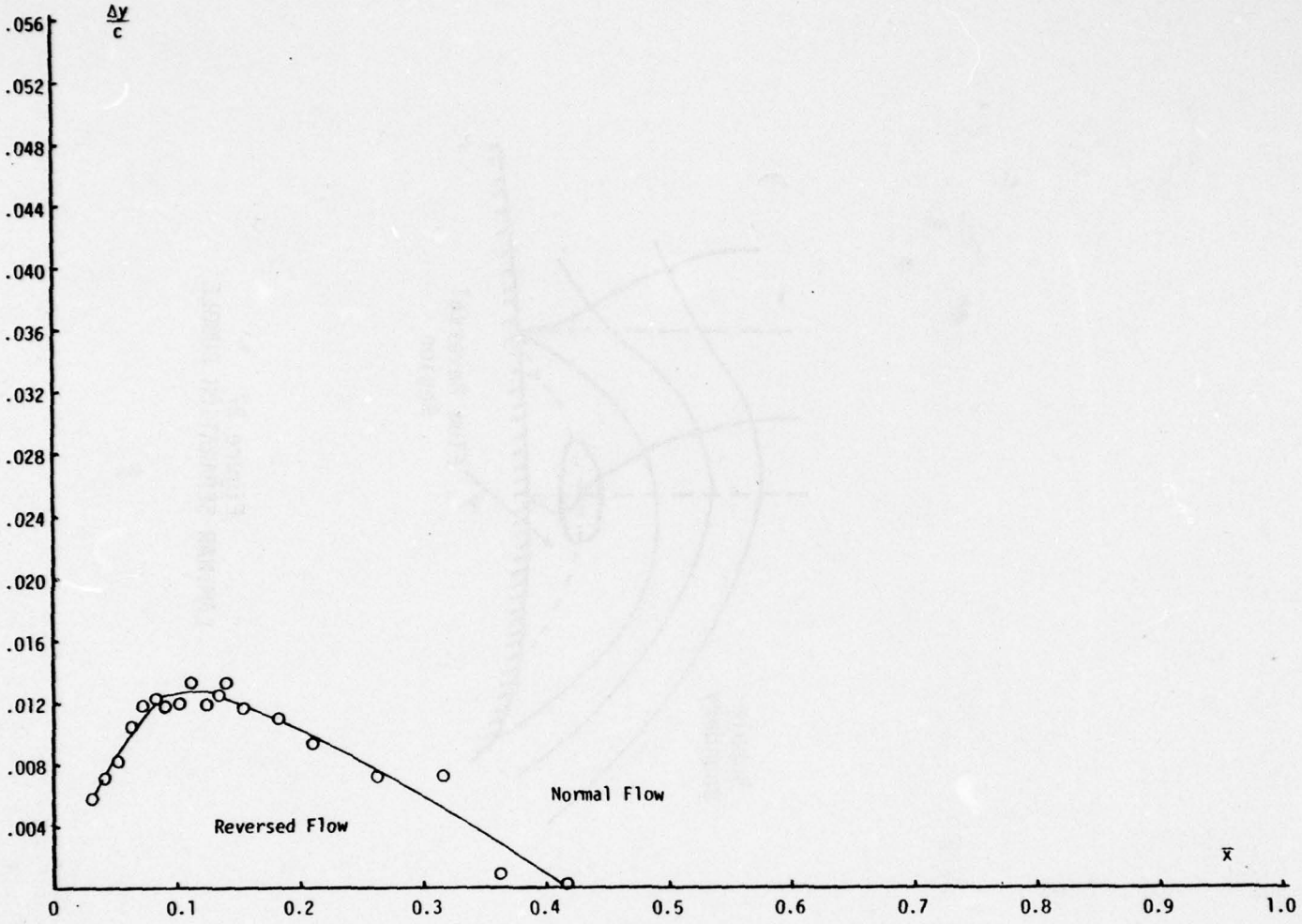


Figure 28
FLOW REVERSAL REGION
Steady Flow, U = 31 ft/sec, α = 10 degrees

axis represents the non-dimensional distance of the sensor from the airfoil leading edge. The region below the line shown on the graph represents a region of reversed flow. Figure 29 shows the steady flow reversal for other angles of attack at the same free stream velocity of 31 feet per second (9.45 meters per second). These data were used to define the steady-flow stall angle of attack (10.5 degrees) as the angle where the flow on the entire airfoil upper surface becomes reversed. Figure 30 shows similar results for a lower free stream velocity of 12 feet per second (3.66 meters per second). The steady-flow stall angle of attack was measured to be unchanged at this lower velocity. This would be expected since the airfoil stall is a function only of angle of attack and is insensitive to the small change in Reynolds number between these two velocities.

The steady-flow reversal measurements provided a comparison for the subsequent unsteady flow measurements. The unsteady flow reversal, described below, indicates that the reversed flow region starts near the leading edge, in a manner similar to the steady flow case, and then spreads downstream. This extended flow reversal feeds mass upstream towards the leading edge.

4.2 Unsteady Boundary Layer Equations

The effects of the velocity oscillation frequency and amplitude on the reversal regions on the airfoil may be more clearly understood by considering the unsteady boundary layer equations. These are developed below following the discussion of McCroskey,[33] who considers the unsteady terms to be perturbations to a

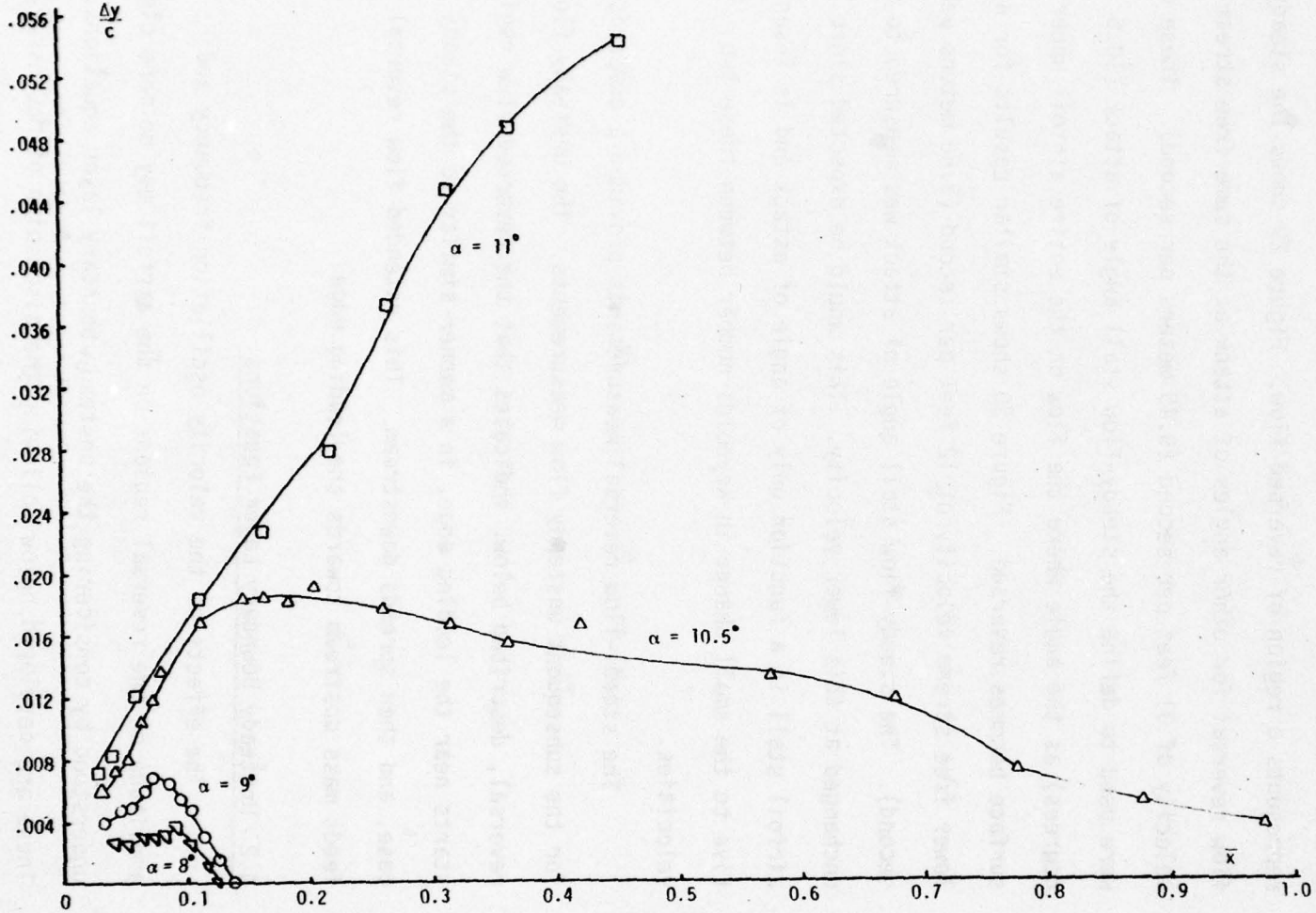


Figure 29
STEADY FLOW REVERSAL REGION (U_1 = 31 ft/sec)

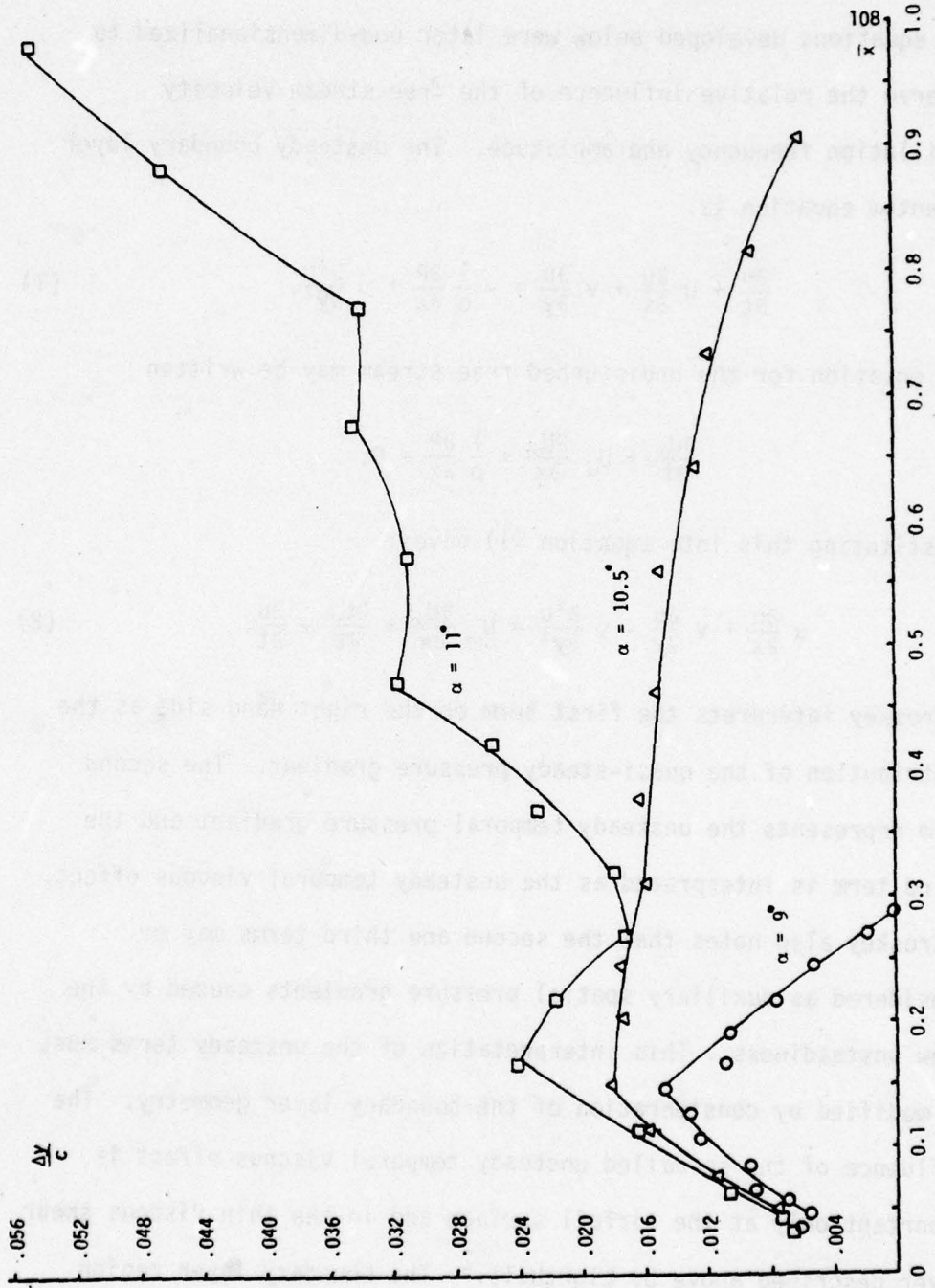


Figure 30
STEADY FLOW REVERSAL REGION (U_1 = 12 ft/sec)

quasi-steady flow. A quasi-steady boundary layer response is one which is always in phase with the oscillating free stream velocity. The equations developed below were later non-dimensionalized to observe the relative influence of the free stream velocity oscillation frequency and amplitude. The unsteady boundary layer momentum equation is:

$$\frac{\partial u}{\partial t} + u \frac{\partial u}{\partial x} + v \frac{\partial u}{\partial y} = - \frac{1}{\rho} \frac{\partial P}{\partial x} + \nu \frac{\partial^2 u}{\partial y^2}. \tag{1}$$

The equation for the undisturbed free stream may be written

$$\frac{\partial U_\infty}{\partial t} + U_\infty \frac{\partial U_\infty}{\partial x} + \frac{1}{\rho} \frac{\partial P}{\partial x} = 0.$$

Substituting this into equation (1) gives:

$$u \frac{\partial u}{\partial x} + v \frac{\partial u}{\partial y} - \nu \frac{\partial^2 u}{\partial y^2} = U_\infty \frac{\partial U_\infty}{\partial x} + \frac{\partial U_\infty}{\partial t} - \frac{\partial u}{\partial t}. \tag{2}$$

McCroskey interprets the first term on the right hand side as the contribution of the quasi-steady pressure gradient. The second term represents the unsteady temporal pressure gradient and the third term is interpreted as the unsteady temporal viscous effect. McCroskey also notes that the second and third terms may be considered as auxiliary spatial pressure gradients caused by the flow unsteadiness. This interpretation of the unsteady terms must be modified by consideration of the boundary layer geometry. The influence of the so-called unsteady temporal viscous effect is important only at the airfoil surface and in the thin viscous shear layer described above by Lighthill.[2] The boundary layer region above this shear layer will be more strongly affected by the temporal and spatial gradients. Also, the results described abpve

obtained by Simpson[15] have indicated that the effects of turbulent mixing must be considered after boundary layer separation has occurred. The boundary layer equation resulting from including the turbulent velocities would include additional unsteady terms due to the Reynolds stresses.

For the moment, the external oscillating flow velocity is assumed to be

$$U_\infty(x,t) = U_1(x)\ [1 + N \sin(\omega t)] \tag{3}$$

where U_1 is the steady mean velocity and N is the amplitude ratio, $\Delta U/U_1$. This oscillating velocity may be used to determine the effect of the free stream oscillations on equation (2). After substitution, the second term on the right hand side of equation (2) becomes:

$$\frac{\partial U_\infty}{\partial t} = U_1(x)\, N\omega \cos(\omega t) = U_1(x)\, N\omega \sin(\omega t + \pi/2)$$

$$= A_1(x) \sin(\omega t + \pi/2). \tag{4}$$

The unsteady temporal pressure gradient is observed to lead the phase of the external velocity by a quarter-period. The first term on the right hand side of equation (2) becomes:

$$U_\infty \frac{\partial U_\infty}{\partial x} = U_1 \frac{dU_1}{dx} + 2NU_1 \frac{dU_1}{dx} \sin(\omega t) + N^2 U_1 \frac{dU_1}{dx} \sin^2(\omega t)$$

$$= B_1(x) + C_1(x) \sin(\omega t) + D_1(x) \sin^2(\omega t). \tag{5}$$

Substitution of equations (4) and (5) into equation (2), using the following non-dimensionalization, yields:

$$u' \frac{\partial u'}{\partial x'} + v' \frac{\partial u'}{\partial y'} - \frac{\partial^2 u'}{\partial y'^2} = 2kN \cos(t') - 2k \frac{\partial u'}{\partial t'} + \frac{1}{U_1} \frac{dU_1}{dx'}$$

$$+ \frac{2N}{U_1} \frac{dU_1}{dx'} \sin(t') + \frac{N^2}{U_1} \frac{dU_1}{dx'} \sin^2(t')$$

$$= A_2 \sin(t' + \pi/2) - 2k \frac{\partial u'}{\partial t'} + B_2(x)$$

$$+ C_2(x) \sin(t') + D_2(x) \sin^2(t') \qquad (6)$$

where:

$$x' = x/c \qquad t' = \omega t = \left(\frac{2kU_1}{c}\right) t$$

$$y' = \frac{R^{1/2} y}{c} \qquad k = \frac{\omega c}{2U_1}$$

$$u' = u/U_1 \qquad N = \frac{\Delta U}{U_1} .$$

$$v' = R^{1/2} v/U_1$$

The first two terms on the right hand side of equation (6) represent, in a non-dimensional form, the unsteady temporal gradient, and the last three terms represent the unsteady spatial gradient. The airfoil geometry provides a boundary condition which determines whether the unsteady spatial pressure gradient is favorable (negative) or adverse (positive). The airfoil angle of attack provides a boundary condition which determines the relative magnitude of the favorable or adverse condition. The favorable or adverse nature of the spatial unsteady pressure gradient depends principally on the sign of the coefficient $C_2(x)$, for small values of the amplitude ratio, N. For large oscillation amplitude ratios near one, however, the coefficient $D_2(x)$ becomes equally important. Large oscillation amplitude ratios can have a large influence on the

phase lead or lag of the unsteady boundary layer response through the trigonometric relationship:

$$D_2(x) \sin^2 t' = \frac{D_2(x)}{2} [1 + \cos 2t'].$$

The three terms of the unsteady spatial gradient are observed to be functions of the mean velocity, U_1, and velocity oscillation amplitude ratio, N, but not of the reduced frequency, k. The unsteady temporal pressure gradient, which is the first term on the right hand side of equation (6), depends on both the reduced frequency and the oscillation amplitude ratio. Because of differentiation, the contribution of this term leads the phase of the free stream velocity by $\pi/2$ radians. The influence of this term is opposed by the effect of the unsteady viscous term, the second term on the right hand side of equation (6). The viscous term is observed to be a function of the reduced frequency, and is independent of the oscillation amplitude ratio. This term will be of very small influence away from the airfoil surface.

The effect of the unsteady spatial and temporal gradients on the shear at the wall are summarized in Figure 31, from McCroskey.[32] The graphs on the left hand side of the figure show the influence of a favorable unsteady spatial pressure gradient ($C_2(x) \geq 0$), while the right hand sides show the effect of an adverse gradient ($C_2(x) < 0$). This unsteady contribution is similar to the effect of an adverse spatial pressure gradient in steady flow, which causes steady boundary layer separation. The unsteady adverse pressure gradient, however, is shown to be of opposite phase as well as opposite sign. The graphs of wall shear at the bottom of Figure 31

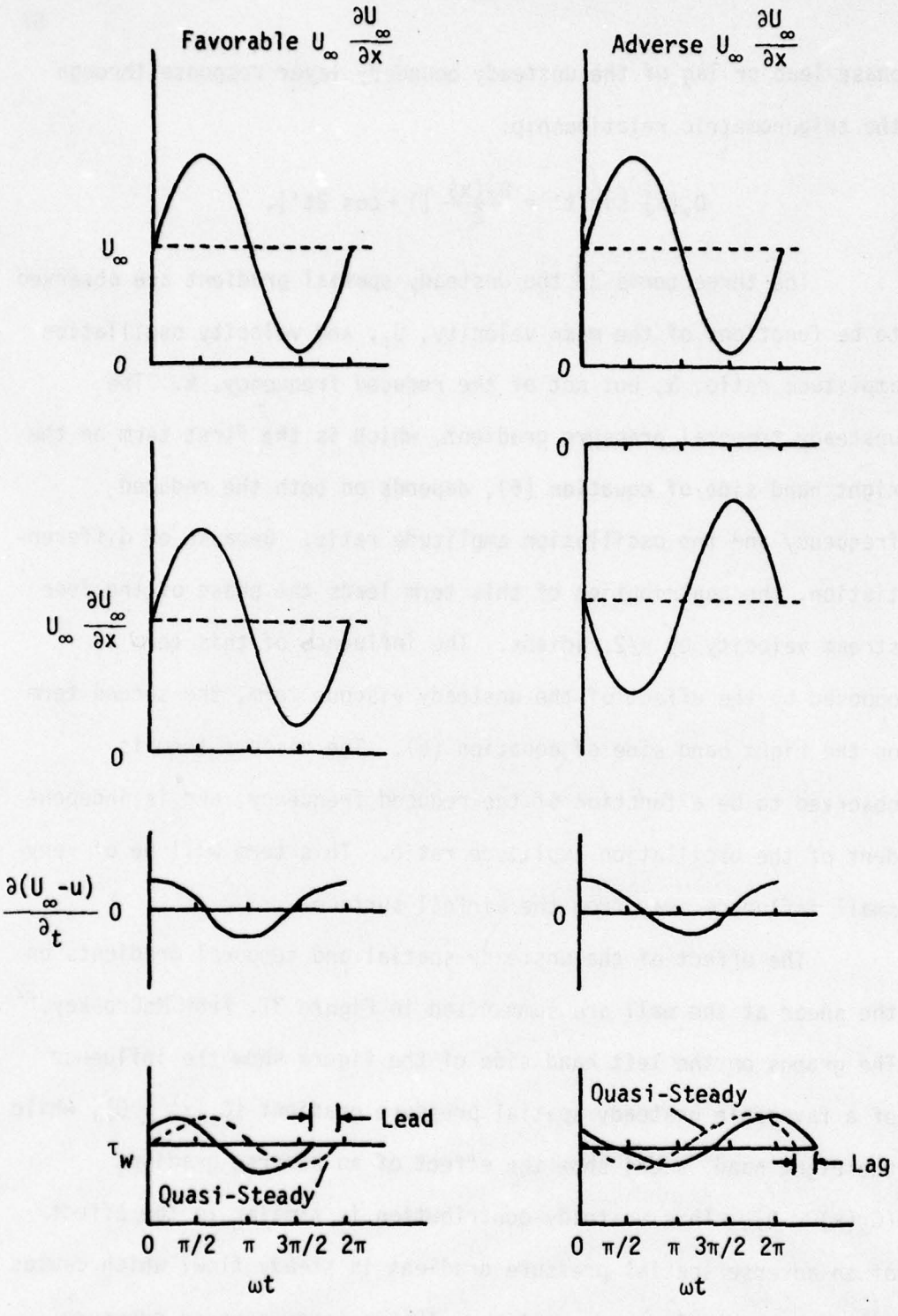


Figure 31
UNSTEADY EFFECTS ON BOUNDARY LAYER FLOWS
(reference 32)

indicate how the unsteady gradients cause the shear to depart from the quasi-steady response. This presentation shows that the shear leads the phase of the quasi-steady response for a favorable, unsteady spatial pressure gradient, and lags the quasi-steady response for an adverse spatial gradient. It must be remembered that this shear was produced by a small oscillation amplitude ratio. The actual phase lead or lag will ultimately depend on whether the spatial or temporal gradients dominate the boundary layer response. Both phase leads and lags from the quasi-steady response were noted in the experimental data presented below. These data use flow reversal in the velocity field measured above the airfoil surface, rather than wall shear, to indicate the onset of unsteady flow effects.

The manner in which the term "quasi-steady" is used in this experiment should be more clearly defined, since the term has several different meanings in the literature. Some authors[1] consider a quasi-steady boundary layer response to be one which is in phase with the time-varying external velocity. Others[17] define a quasi-steady response as one which is identical in magnitude to an equivalent series of steady-flow responses measured for the fixed values of the free stream velocity occurring at each phase of the unsteady velocity oscillations. In this experiment, for flow reversal measured at the airfoil surface, the flow reversal is defined to be quasi-steady if it initially appears when the instantaneous free stream velocity magnitude drops below the mean velocity magnitude, and disappears when the velocity magnitude increases above the mean. If the onset of flow reversal is noted

before or after the phase where the varying free stream velocity passes through the mean value ($t' = 0,\pi$), it is said to lead or lag the phase of the free stream velocity. A quasi-steady flow reversal response is more difficult to describe for regions above the airfoil surface. The reversal region is said to be quasi-steady if the region is symmetrical with respect to the free stream velocity. The reversal region will have a maximum vertical height when the magnitude of the free stream velocity is a minimum. If the reversal region is skewed to the left or right, it is said to lead or lag, respectively, the phase of the free stream.

If the assumed form of the free stream velocity given in equation (3) is not correct, that is, if the flow is not sinusoidal but varies as:

$$U_\infty(x,t) = U_1(x)\left\{1 + N\sum_{n=1}^{\infty}\left[a_n \cos(n\omega t) + b_n \sin(n\omega t)\right]\right\}, \qquad (7)$$

then the momentum equation must be altered as follows:

$$u'\frac{\partial u'}{\partial x'} + v'\frac{\partial u'}{\partial y'} - \frac{\partial^2 u'}{\partial y'^2} = 2kN\sum_{n=1}^{\infty}\left[nb_n \sin(nt' + \pi/2) - na_n \sin(nt')\right]$$

$$- 2k\frac{\partial u'}{\partial t'} + \frac{1}{U_1}\frac{dU_1}{dx'}$$

$$+ \frac{2N}{U_1}\frac{dU_1}{dx'}\sum_{n=1}^{\infty}\left[a_n \sin(nt' + \pi/2) + b_n \sin(nt')\right]$$

$$+ \frac{N^2}{U_1}\frac{dU_1}{dx'}\sum_{n=1}^{\infty}\left[a_n \sin(nt' + \pi/2) + b_n \sin(nt')\right]^2 \qquad (8)$$

It can be seen in equation (8) that the viscous term, the second term on the right hand side, is not affected by the higher harmonics. The higher harmonics manifest themselves as pressure waves and not as viscous shear. The higher harmonic terms could, however, drastically alter the influence of both the spatial and temporal unsteady terms. The complicated interaction of the high frequency terms in equation (8) shows the desirability of having the free stream velocity oscillations as free as possible of high harmonic content.

A more detailed investigation should consider the oscillating velocity at the outer edge of the airfoil boundary layer, of the form

$$U_\infty(x,t) = U_1(x)\left\{1 + N(x)\sin\left[\omega t + \theta(x)\right]\right\}$$

where both the amplitude ratio, N, and a phase angle, θ, are functions of distance along the airfoil chord. After substitution, several additional terms are observed in the non-dimensional boundary layer equation:

$$u'\frac{\partial u'}{\partial x'} + v'\frac{\partial u'}{\partial y'} - \frac{\partial^2 u'}{\partial y'^2} = 2kN\cos(t'+\theta) - 2k\frac{\partial u'}{\partial t'}$$

$$+ \frac{1}{U_1}\frac{dU_1}{dx'} + \frac{2N}{U_1}\frac{dU_1}{dx'}\sin(t'+\theta) + \frac{N^2}{U_1}\frac{dU_1}{dx'}\sin^2(t'+\theta)$$

$$+ \frac{dN}{dx'}\sin(t'+\theta) + n\frac{dN}{dx'}\sin^2(t'+\theta)$$

$$+ N\frac{d\theta}{dx'}\cos(t'+\theta) + N^2\frac{d\theta}{dx'}\sin(t'+\theta)\cos(t'+\theta).$$

Using the Fourier series presentation:

$$U_\infty(x,t) = U_1(x)\left\{1 + N(x)\sum_{n=1}^{\infty}\left[a_n(x)\cos(n\omega t) + b_n(x)\sin(n\omega t)\right]\right\},$$

the non-dimensional boundary layer equation becomes

$$u'\frac{\partial u'}{\partial x'} + v'\frac{\partial u'}{\partial y'} - \frac{\partial^2 u'}{\partial y'^2} = 2kN\sum_{n=1}^{\infty}\left[nb_n\cos(nt') - na_n\sin(nt')\right]$$

$$- 2k\frac{\partial u'}{\partial t'} + \frac{1}{U_1}\frac{dU_1}{dx'}$$

$$+ \frac{2N}{U_1}\frac{dU_1}{dx'}\sum_{n=1}^{\infty}\left[a_n\cos(nt') + b_n\sin(nt')\right]$$

$$+ \frac{N^2}{U_1}\frac{dU_1}{dx'}\sum_{n=1}^{\infty}\left[a_n\cos(nt') + b_n\sin(nt')\right]^2$$

$$+ \frac{dN}{dx'}\sum_{n=1}^{\infty}\left[a_n\cos(nt') + b_n\sin(nt')\right]$$

$$+ N\frac{dN}{dx'}\sum_{n=1}^{\infty}\left[a_n\cos(nt') + b_n\sin(nt')\right]^2$$

$$+ N\sum_{n=1}^{\infty}\left[\frac{\partial a_n}{\partial x'}\cos(nt') + \frac{\partial b_n}{\partial x'}\sin(nt')\right]$$

$$+ N^2\sum_{n=1}^{\infty}\left[a_n\cos(nt') + b_n\sin(nt')\right]\left[\frac{\partial a_n}{\partial x}\cos(nt')\right.$$

$$\left. + \frac{\partial b_n}{\partial x}\sin(nt')\right]$$

The additional terms described above were considered to be very small since the wavelength of the free stream velocity

oscillation was longer than the length of the wind tunnel test section. Preliminary correlation measurements of velocity near the airfoil leading and trailing edges showed almost exact correlation.

4.3 Unsteady Flow Reversal for Angles of Attack Below the Steady Flow Stall Angle

The locus of points which indicated the onset of reversed flow was used to define the flow reversal region. Figure 32 presents unsteady flow reversal measurements for an airfoil angle of attack of 9 degrees (below the measured steady flow stall angle of 10.5 degrees) and a mean velocity of 31 feet per second (9.45 meters per second). The spatial extent of the flow reversal region, expressed by nondimensional chord and height above the airfoil surface, is indicated for several phase points in the oscillation period. The regions below the curves represent reversed flow. The limited upstream extent of the reversal measurements was due to the geometry of the split-film probe. Although data was collected for 256 phase points in the half-period shown, the limitations of the graphical data presentation dictated that only a small number of phase points be plotted. Two-dimensional presentations of these data, shown below, include data for more phase points. Figure 33 presents similar data collected at a higher reduced frequency, but with approximately the same oscillation amplitude ratio. Flow reversal measured at this same angle of attack, but at a much larger oscillation amplitude ratio, are shown in Figure 34.

For this angle of attack, the reversed flow region was observed to be similar in size and shape to the flow reversal which formed the separation bubble noted in steady flow. The flow

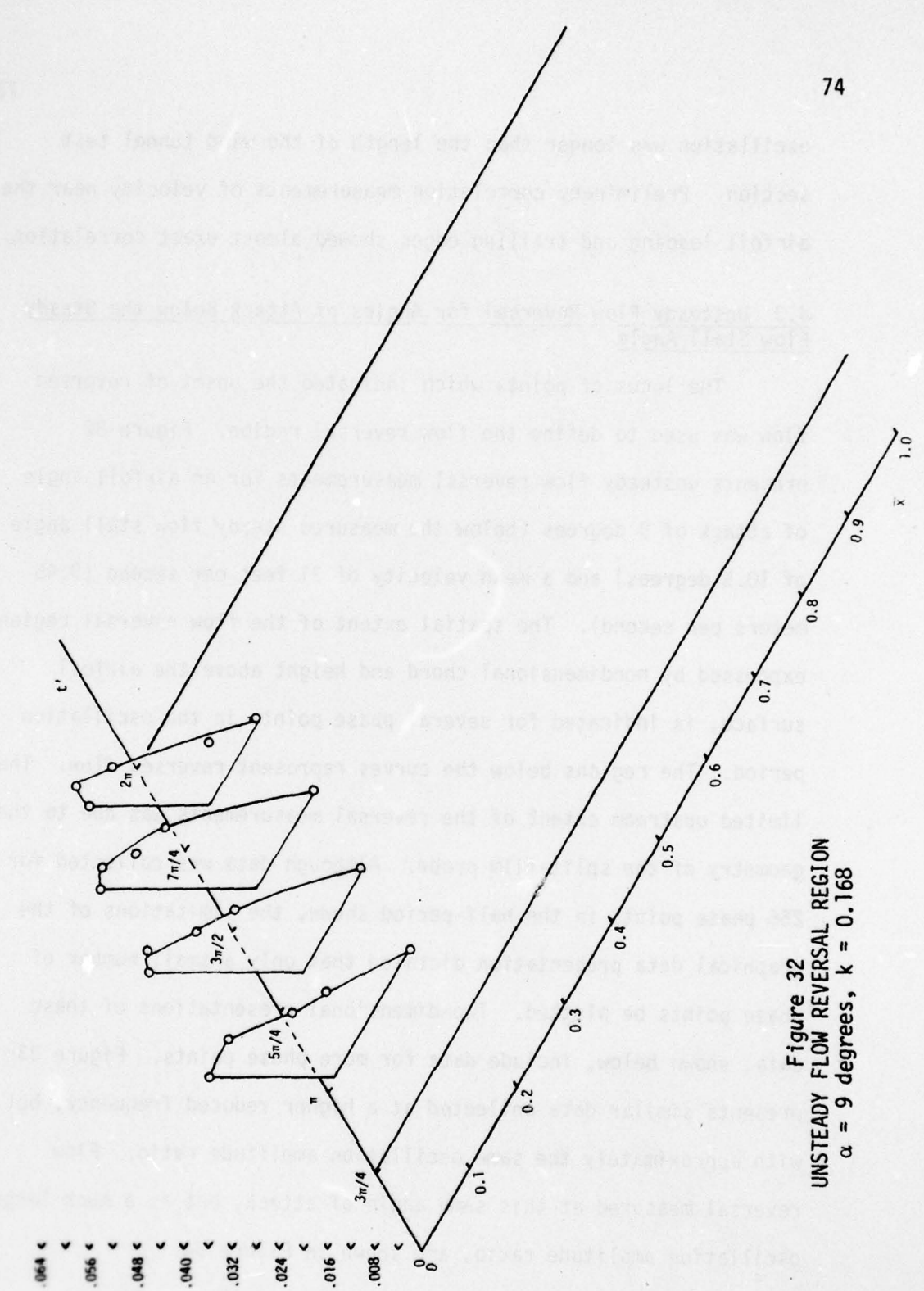


Figure 32
UNSTEADY FLOW REVERSAL REGION
α = 9 degrees, k = 0.168

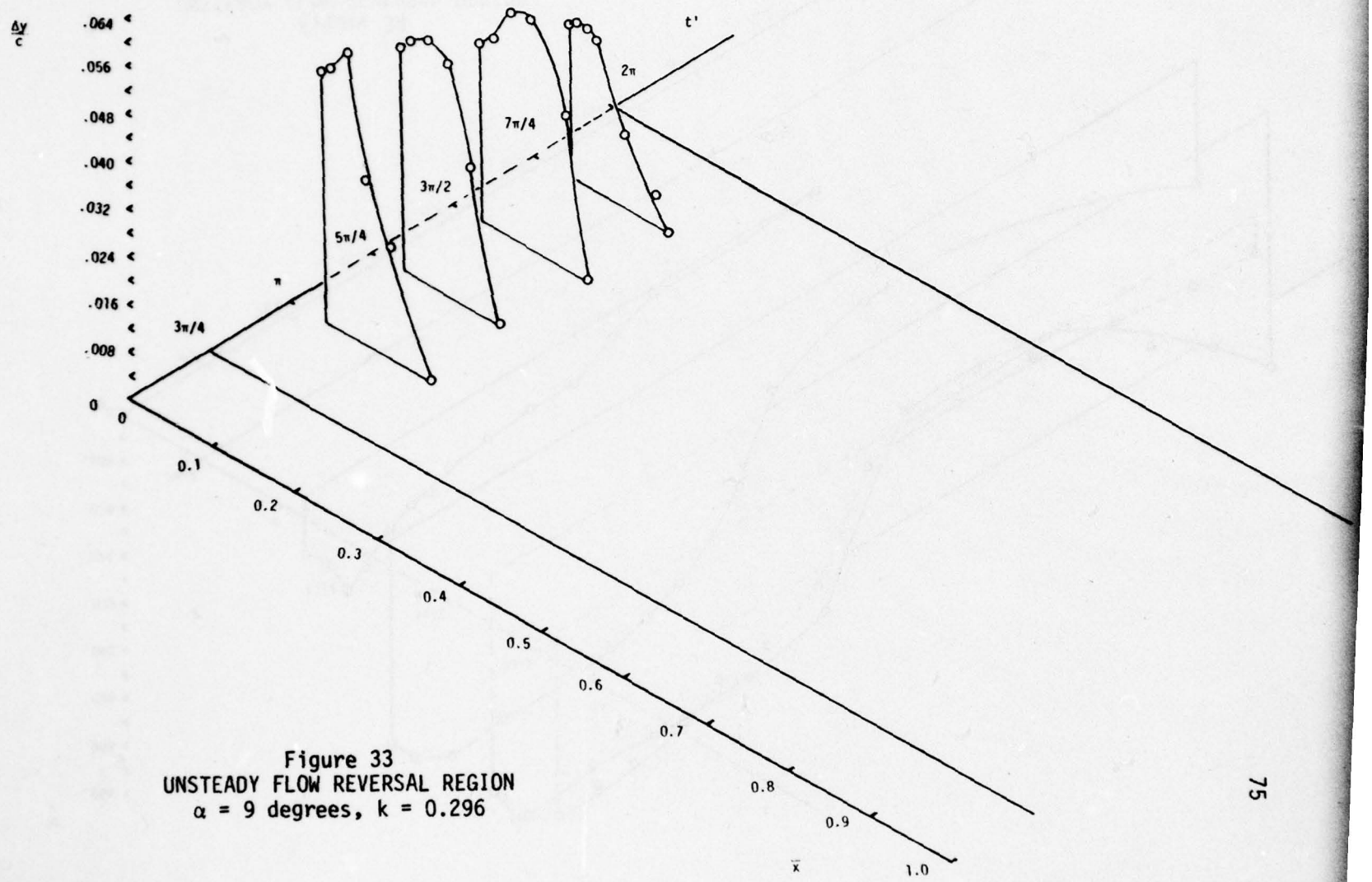


Figure 33
UNSTEADY FLOW REVERSAL REGION
α = 9 degrees, k = 0.296

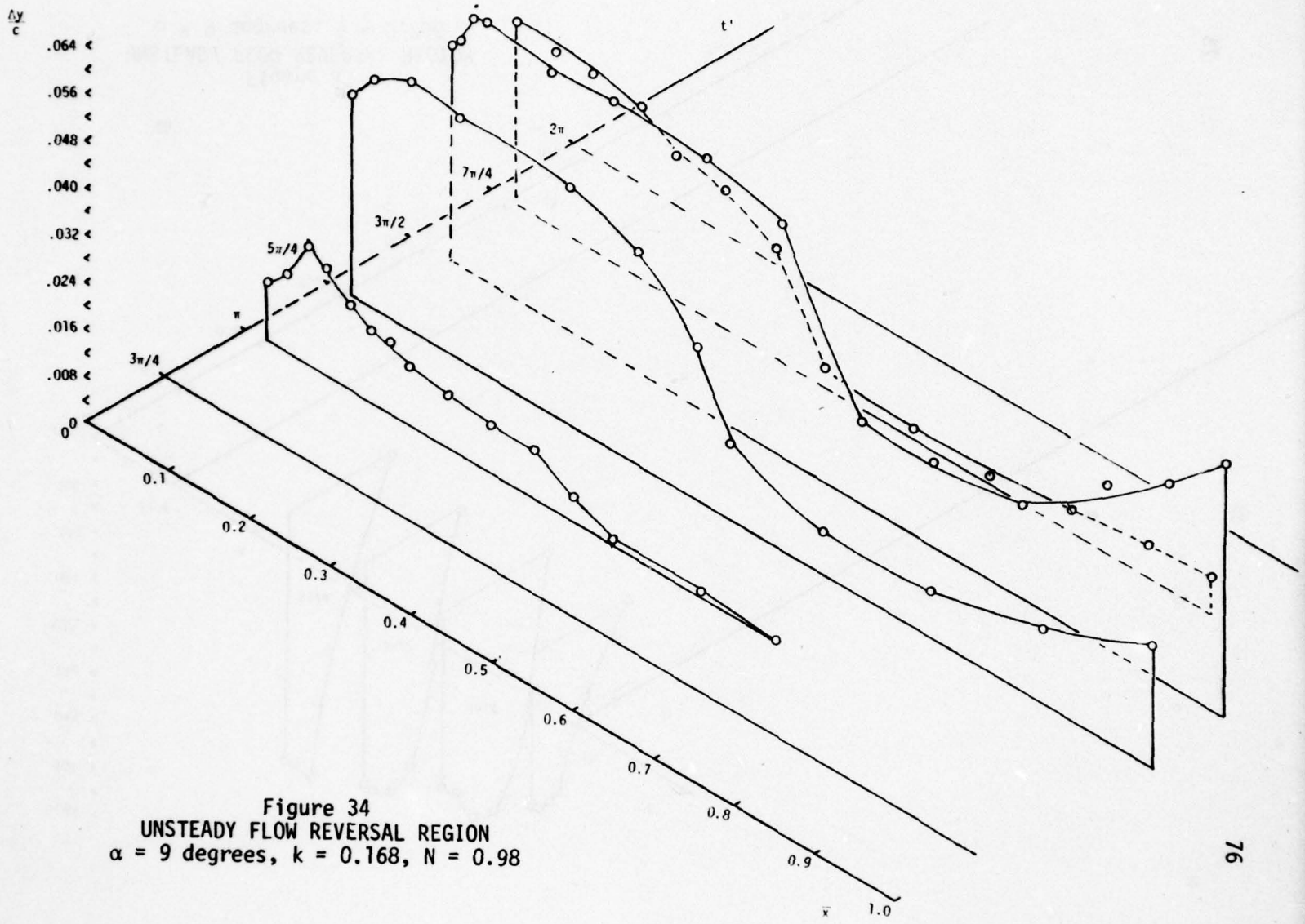


Figure 34
UNSTEADY FLOW REVERSAL REGION
α = 9 degrees, k = 0.168, N = 0.98

reversal was observed only during the second half of the velocity oscillation period ($\pi \leq t' \leq 2\pi$) when the magnitude of the free stream velocity was smaller than the mean velocity. At other oscillation phase points the reversed flow disappeared, indicating that the laminar flow near the airfoil leading edge never separated.

4.4 Unsteady Flow Reversal for Angles of Attack Above the Steady Flow Stall Angle

Reversal data measured at the higher angles of attack indicated that the flow reversal region extended over the entire airfoil upper surface and, in many cases, thickened near the trailing edge. The adverse unsteady pressure gradient appeared to exert a stronger influence on the onset of flow reversal than noted at lower angles of attack. Measurements were made at an angle of attack of 11 degrees, just above the steady flow stall angle, and also at an angle of attack of 12 degrees. Reversal data shown in Figure 35 were measured at an intermediate reduced frequency (vane rotation speed of 2.0 Hz) and a low oscillation amplitude ratio. Similar data for two higher frequencies are presented in Figures 36 and 37. Figure 38 shows measurements made at a much lower reduced frequency of $k = 0.119$, produced by using a lower vane rotation speed of 1.43 Hz. An increase in the angle of attack to 12 degrees produced the flow reversals presented in Figures 39 and 40, measured at intermediate and high reduced frequencies, respectively. The influence of a large oscillation amplitude ratio was measured only at an angle of attack of 11 degrees and is shown in Figure 41.

It was observed that the flow reversal region initially appeared near the airfoil leading edge. This result is in contrast

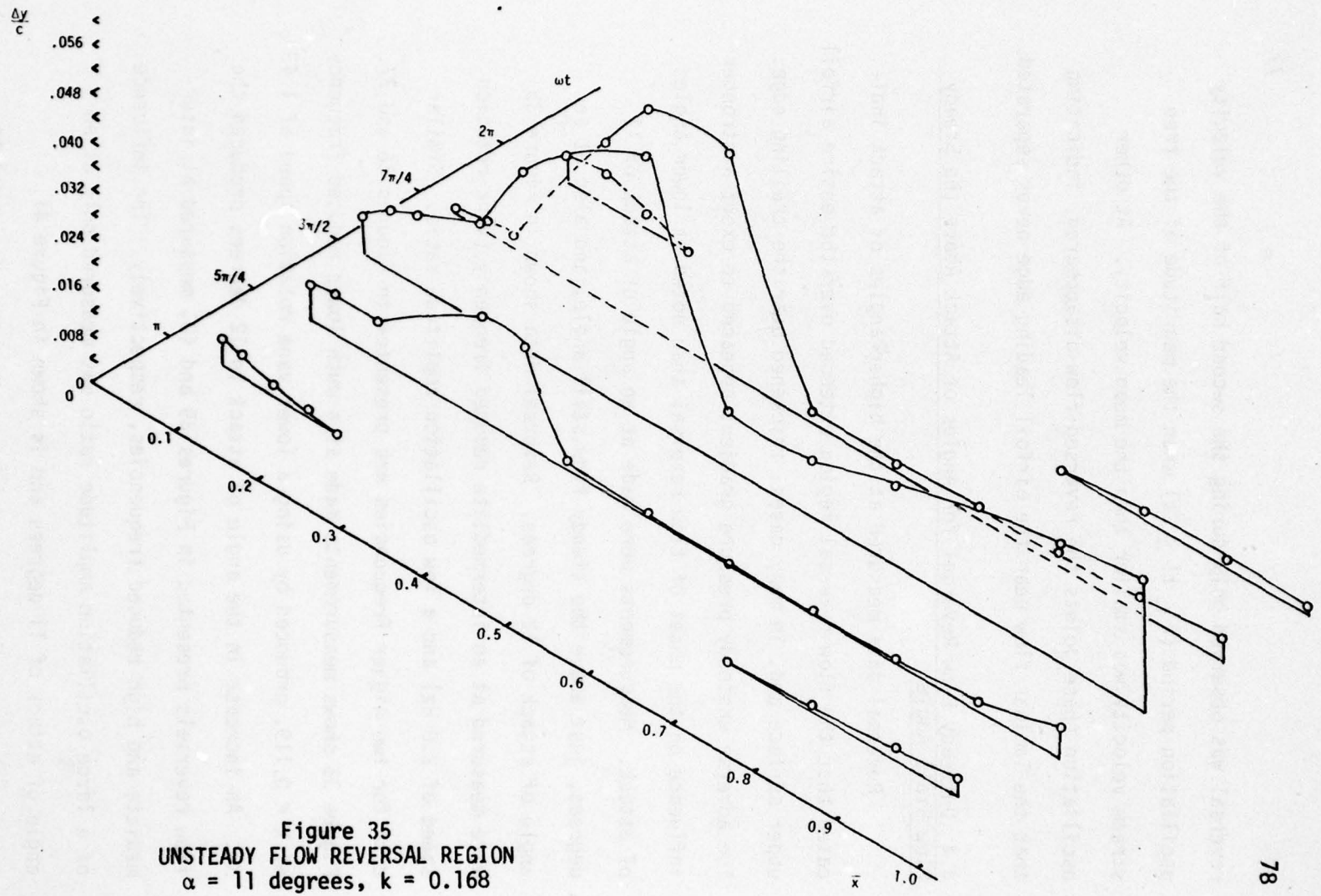


Figure 35
UNSTEADY FLOW REVERSAL REGION
α = 11 degrees, k = 0.168

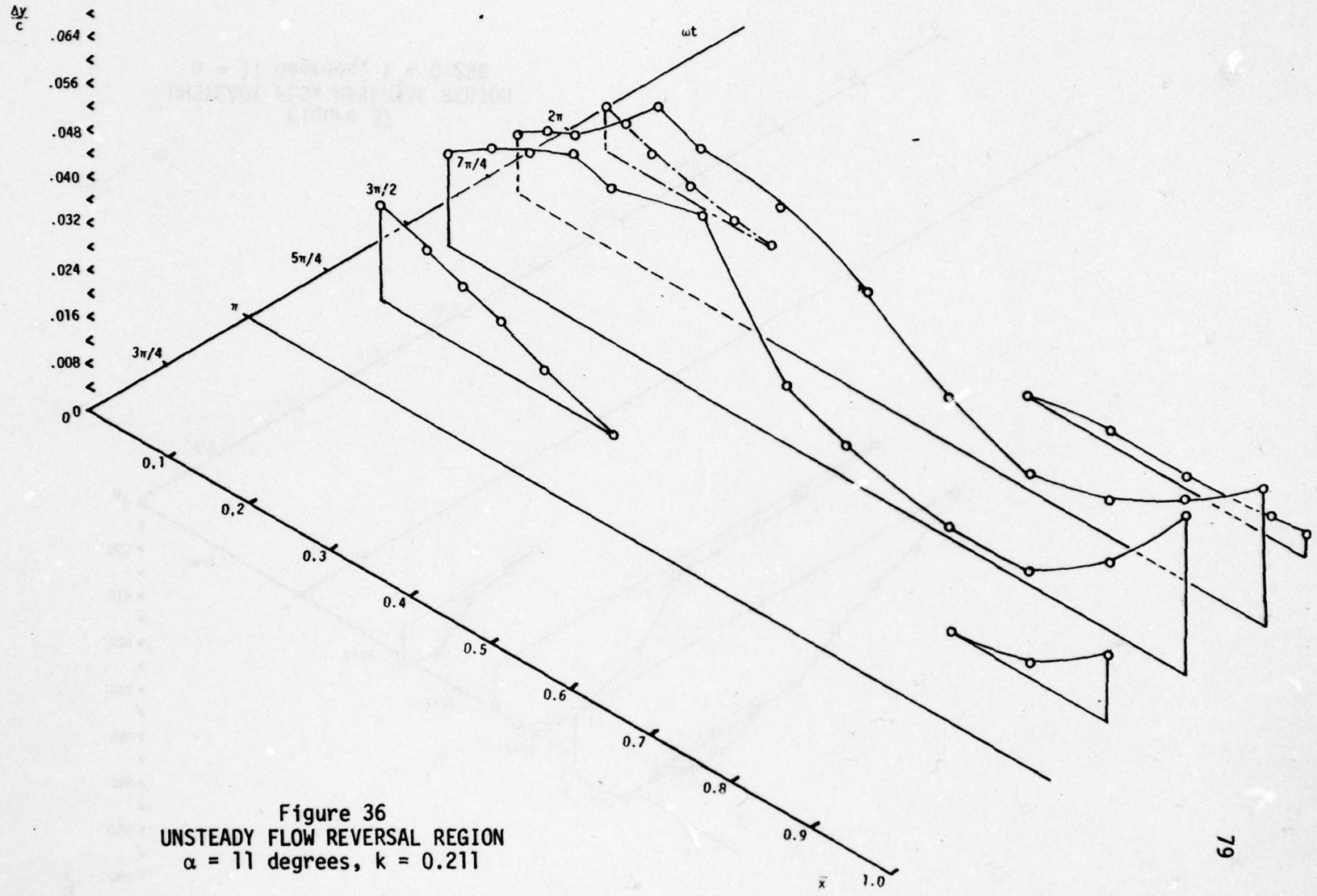


Figure 36
UNSTEADY FLOW REVERSAL REGION
α = 11 degrees, k = 0.211

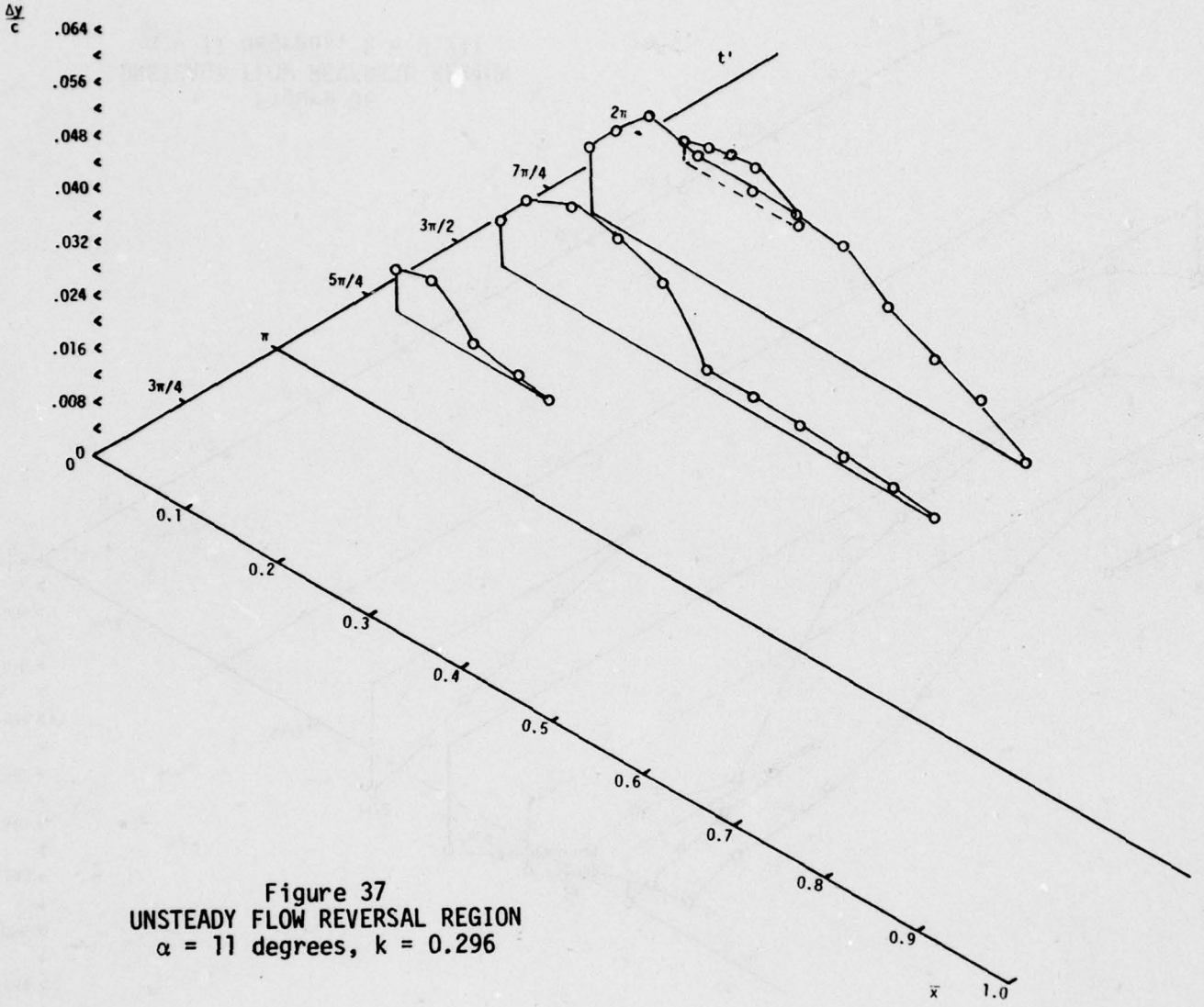


Figure 37
UNSTEADY FLOW REVERSAL REGION
α = 11 degrees, k = 0.296

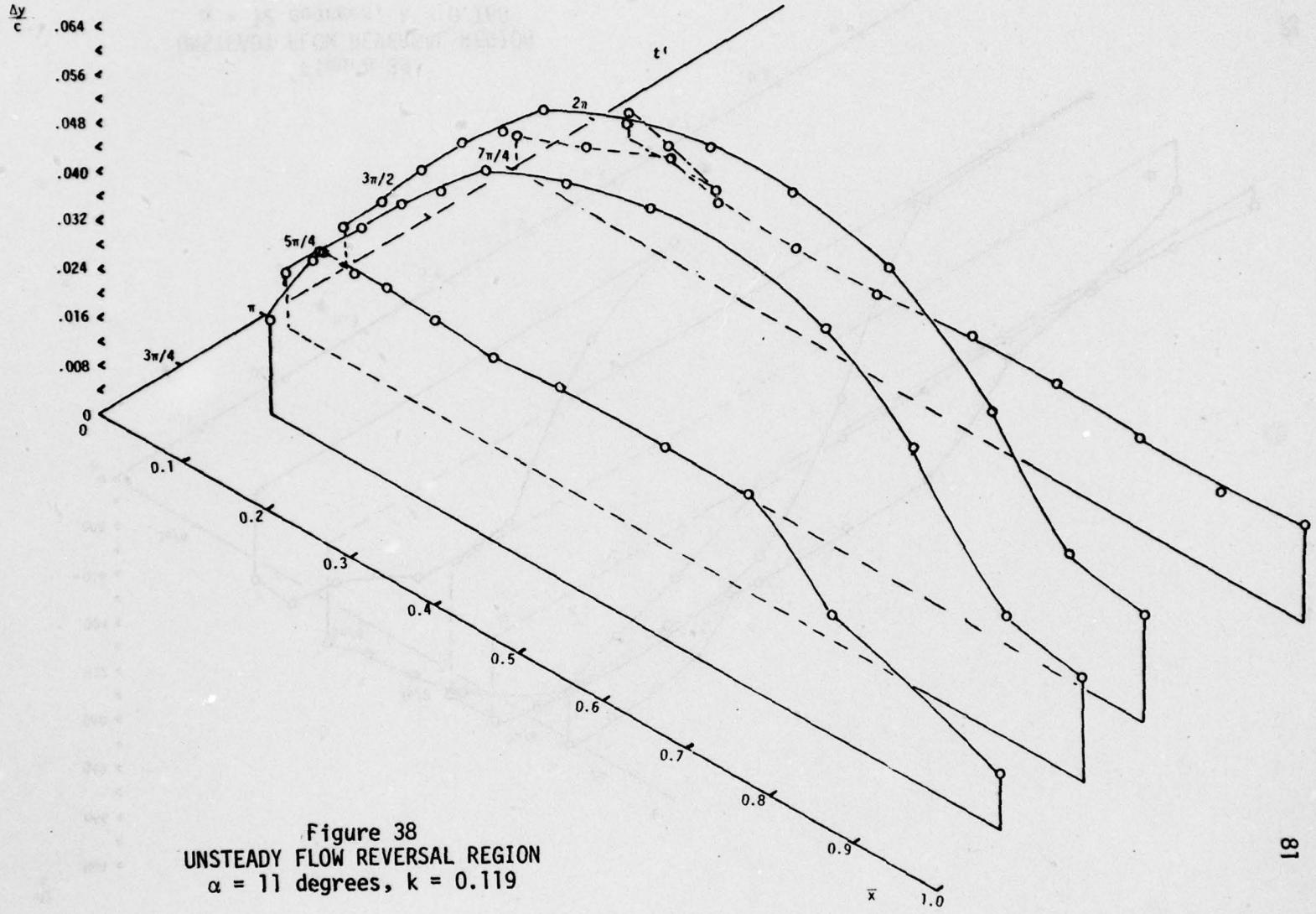


Figure 38
UNSTEADY FLOW REVERSAL REGION
α = 11 degrees, k = 0.119

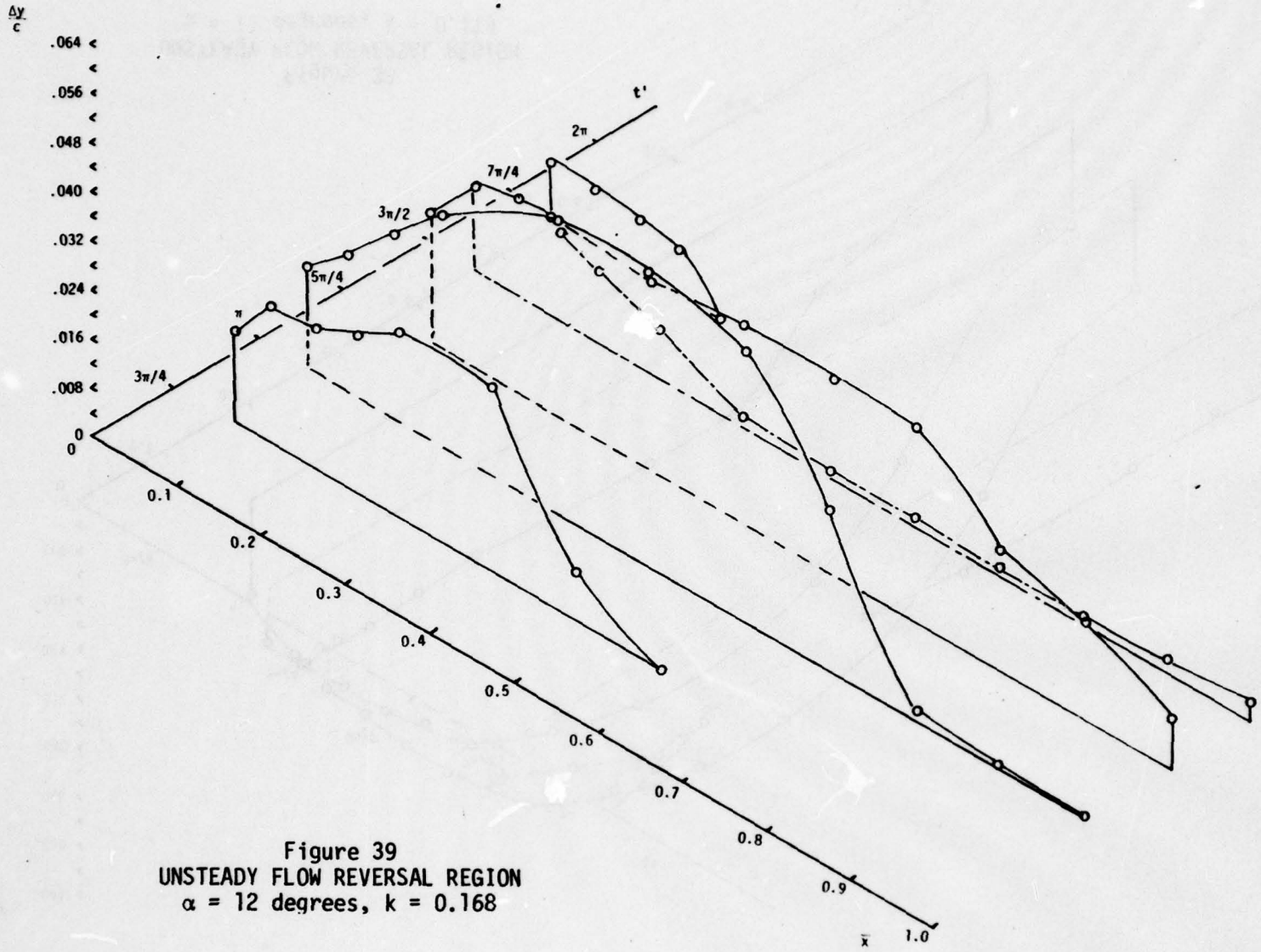


Figure 39
UNSTEADY FLOW REVERSAL REGION
α = 12 degrees, k = 0.168

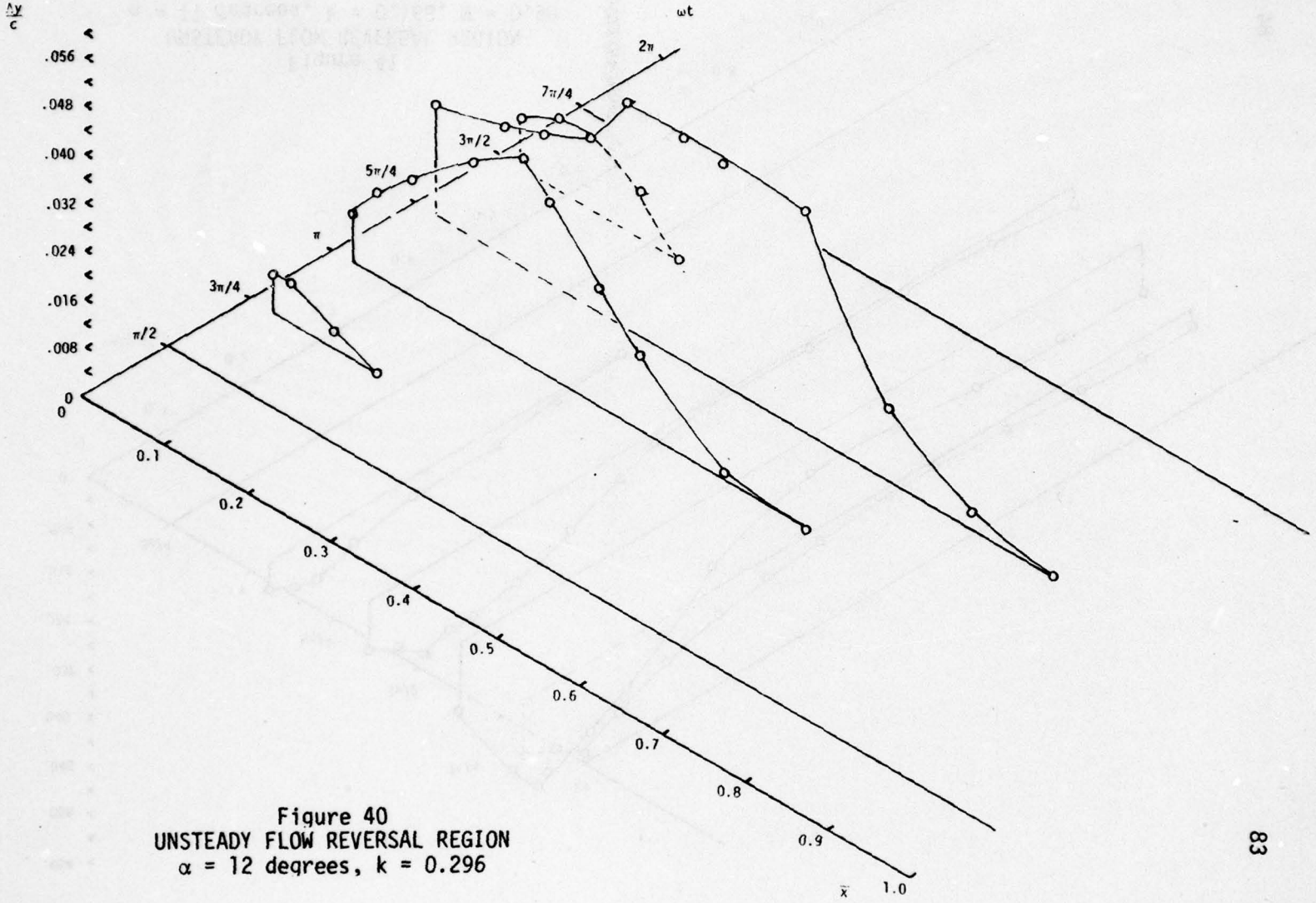


Figure 40
UNSTEADY FLOW REVERSAL REGION
α = 12 degrees, k = 0.296

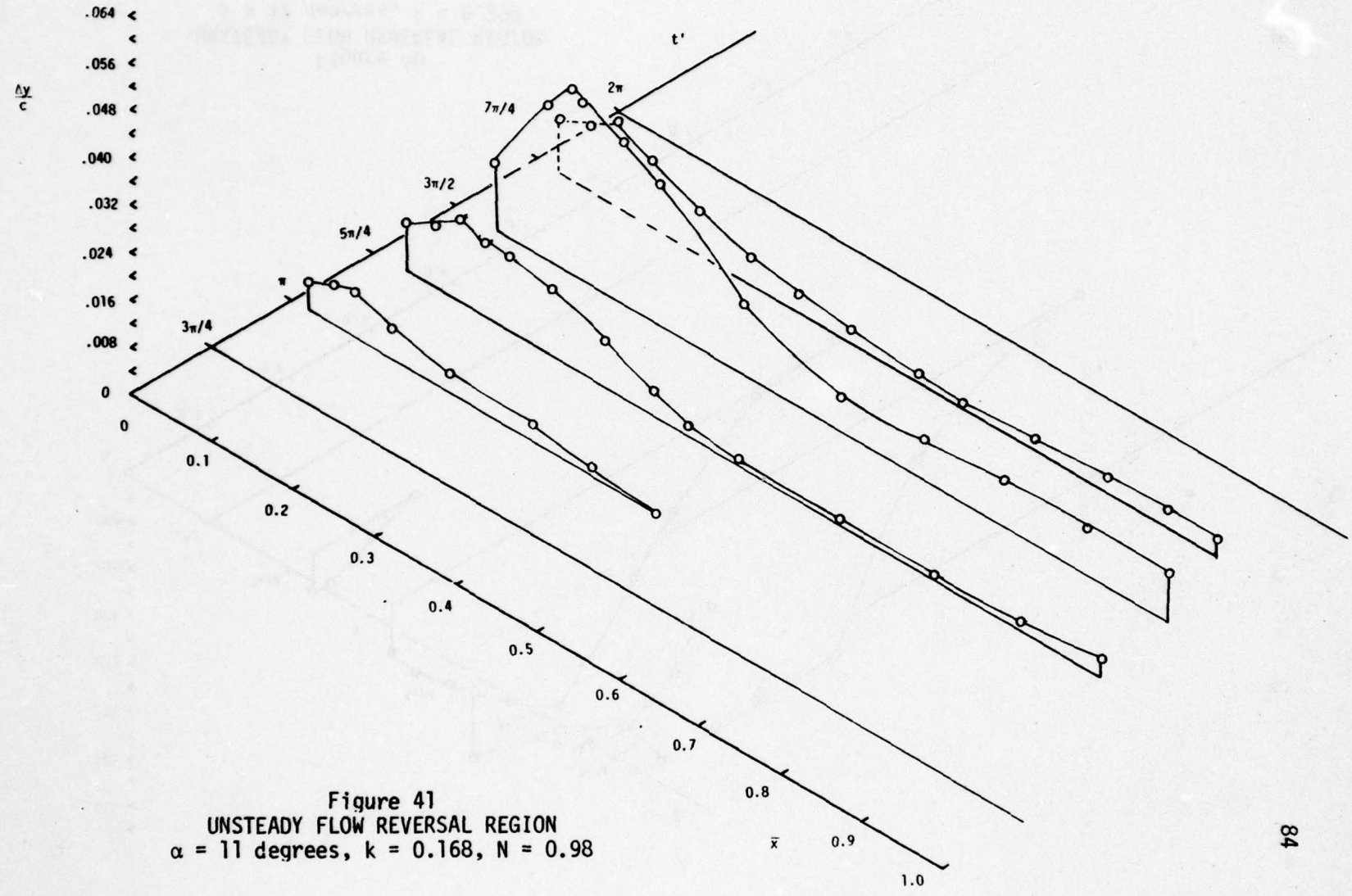


Figure 41
UNSTEADY FLOW REVERSAL REGION
α = 11 degrees, k = 0.168, N = 0.98

to trailing edge flow reversal noted by Carr, McAlister and McCroskey[3] for the oscillating NACA 0012 airfoil. At first consideration, the leading edge flow reversal would appear to be closer in nature to the results noted in Figure 2 for the NACA 0012 airfoil with the sharp leading edge. However, this leading edge reversal phenomena was identified as a "bursting" of the leading edge laminar bubble, and was not considered the classical dynamic stall flow model. It is felt that, for the stationary airfoil in the oscillating flow, the initial onset and downstream growth of the flow reversal region is due to the energy being transferred to the laminar reversal region by the turbulent flow. The reversal region is not due to a downstream extension of the leading edge laminar bubble. It is also felt that the trailing edge reversal was not observed on the stationary airfoil because of the absence of pitch rate effects. The increased unsteady spatial pressure gradients near the trailing edge caused by the inertia of the airflow close to the moving airfoil were not present.

The shape of the reversal regions described in the figures above bears a strong resemblance to the reversal and separation model of Sears and Telionis,[11] shown in Figure 3. The thickening of the flow reversal near the trailing edge in Figure 37 may be indicative of unsteady boundary layer separation. The larger reversal region for the larger angle of attack of 12 degrees would seem to indicate that unsteady separation has occurred further upstream. The model described in Figure 37 considered only one phase point of the unsteady flow period and did not include the formation of any leading edge vortex disturbances. Higher

frequencies were observed, in Figure 39, to eliminate the reversal region thickening near the trailing edge. According to the above model, this would represent the absence of unsteady boundary layer separation throughout the oscillation period. This is an important result when applied to the problem of dynamic stall. At higher oscillation frequencies, the flow reversal could be responsible for feeding mass to the leading edge vortex-like disturbance without separation occurring near the trailing edge.

5. FREQUENCY EFFECTS ON FLOW REVERSAL

5.1 Frequency Effects for Angles of Attack Below the Steady Flow Stall Angle

The changes of the shape of the flow reversal region produced by varying the reduced frequency of oscillation are indicated in Figure 42 for an airfoil angle of attack of 9 degrees. Close to the airfoil surface, there appeared to be very little influence caused by the flow unsteadiness, since the chordwise extent of the flow reversal was almost the same for all frequencies, including steady flow. As the reduced frequency was increased, however, the reversal region increased in height above the airfoil surface.

These height increases are believed to be caused by changes in the unsteady centrifugal forces along the streamlines, rather than the unsteady terms described in equation (6). The unsteady effects may be interpreted using boundary layer equations written in generalized orthogonal coordinates aligned with the airfoil surface. Consider first the steady momentum equation for flow normal to the airfoil surface (along the y axis):

$$-\kappa u^2 = -\frac{1}{\rho}\frac{\partial P}{\partial y} . \qquad (9)$$

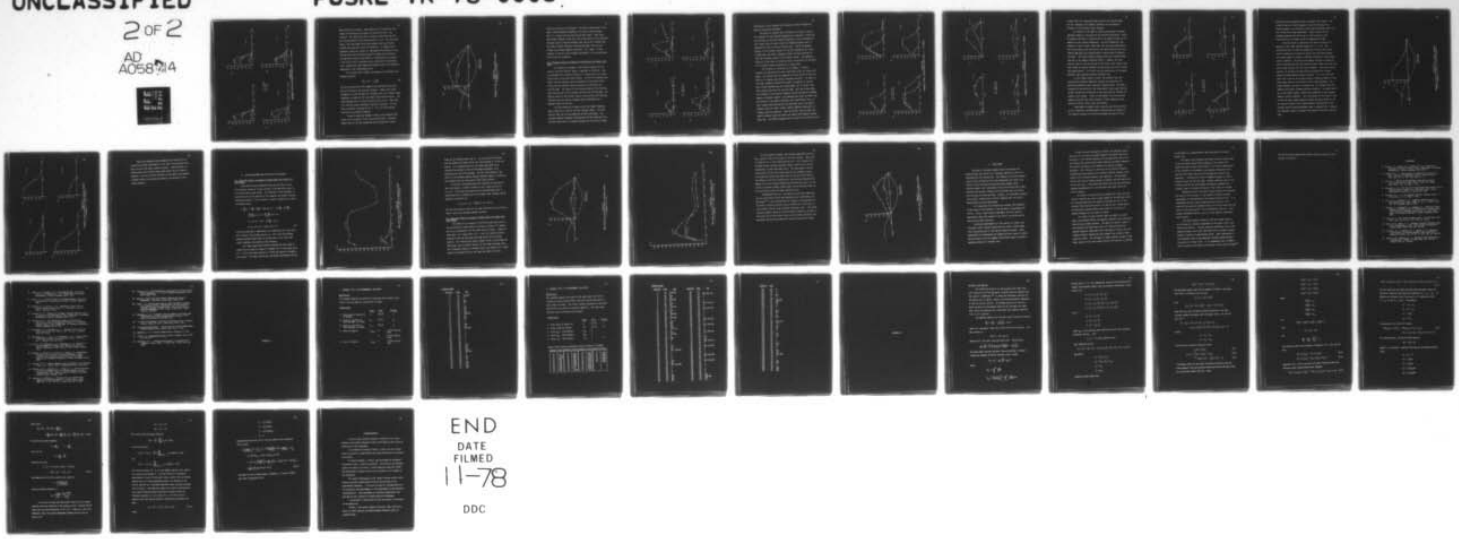
This equation indicates the pressure gradient, on the right hand side, necessary to balance the centrifugal force, on the left hand side. These forces are due to the local streamline curvature, κ,

AD-A058 714 FRANK J SEILER RESEARCH LAB UNITED STATES AIR FORCE --ETC F/G 20/4
UNSTEADY BOUNDARY LAYER FLOW REVERSAL IN A LONGITUDINALLY OSCIL--ETC(U)
AUG 78 J P RETELLE
FJSRL-TR-78-0006

UNCLASSIFIED NL

2 OF 2

AD A058 714



END
DATE FILMED
11-78
DDC

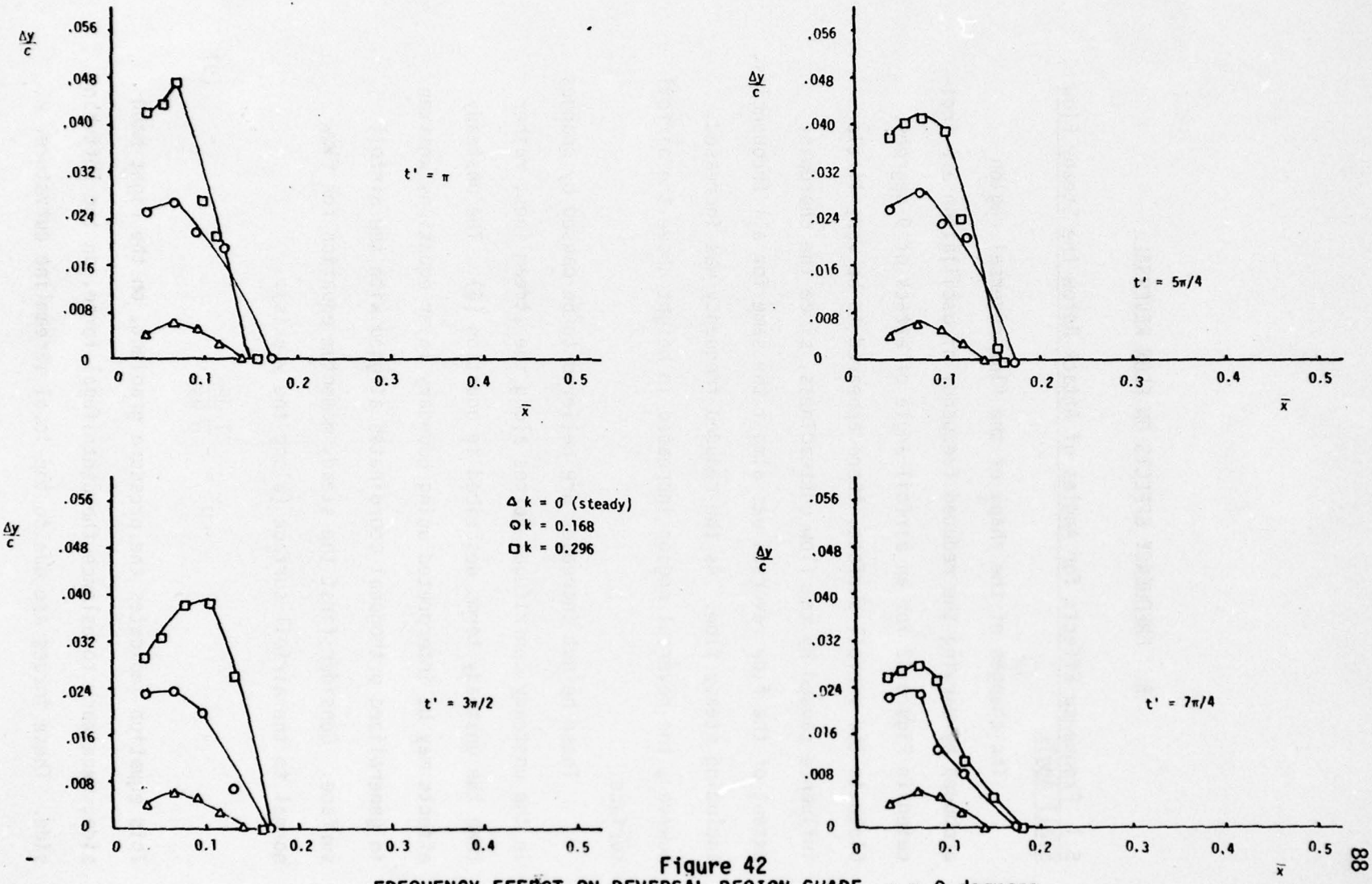


Figure 42
FREQUENCY EFFECT ON REVERSAL REGION SHAPE, α = 9 degrees

above the airfoil surface. When equation (9) is satisfied, the steady flow follows the curvature of the airfoil and is not reversed. The steady flow data in Figure 42 show that the flow was reversed ahead of the chord position $\bar{x} = 0.14$. For this small region, the centrifugal forces were greater than the pressure gradient and equation (9) was not satisfied. It appears that a separation bubble was formed, as indicated by the presence of the reversed flow near the leading edge for steady flow conditions. The chordwise extent of the bubble is limited both by a decrease in the local airfoil curvature and by a transition to turbulent flow. Experimental data showed the boundary layer to be turbulent downstream of the reattachment point.

For unsteady flow, another term appears in the normal-flow momentum equation:

$$\frac{\partial v}{\partial t} - \kappa u^2 = -\frac{1}{\rho}\frac{\partial P}{\partial y} . \qquad (10)$$

The local acceleration term augments the centrifugal force that must be balanced by the pressure gradient. Higher oscillation frequencies, acting through this unsteady term, will produce larger imbalances in equation (10) and larger flow reversal regions. The high frequency data in Figure 30 confirm this trend. These data also show the strong influence of the wall curvature. For the lower curvatures occurring aft of $\bar{x} = 0.17$, no flow reversals occurred at any reduced frequency.

Figure 43 shows the change in phase of the reversed flow region over one period of the velocity oscillation. Reversal height data for the two frequencies were plotted for a fixed

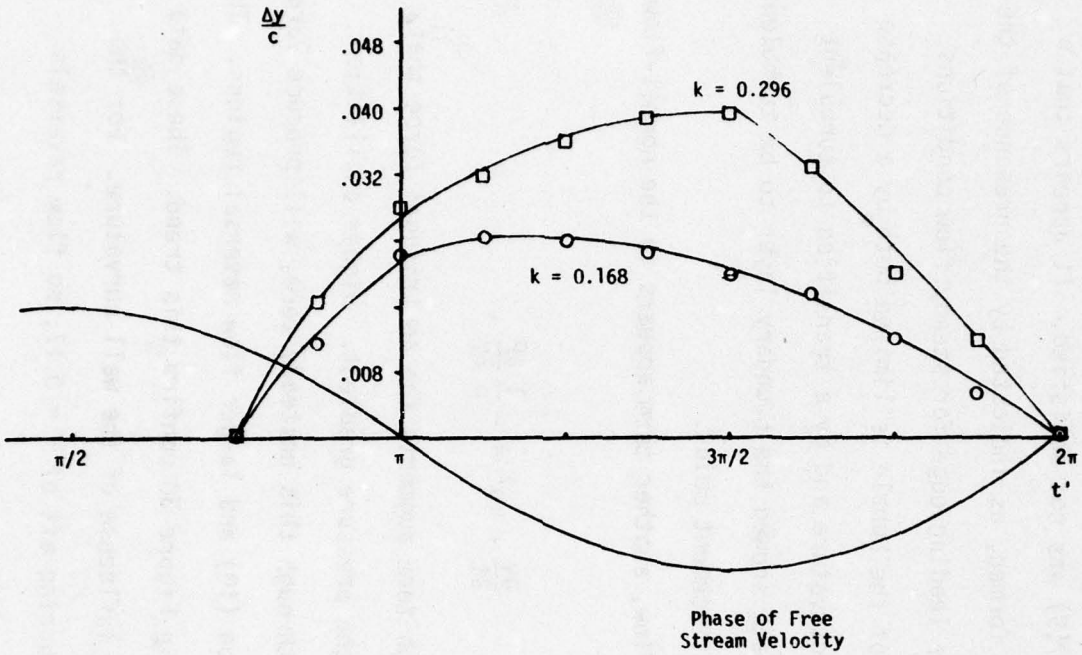


Figure 43
FREQUENCY EFFECT ON PHASE OF FLOW REVERSAL RESPONSE
α = 9 degrees, $\bar{x}$ = 0.10

chord-wise position of 10 percent. The phase relationships of the data at both frequencies appeared to be close to quasi-steady, that is, in phase with the oscillating free stream. Both curves were skewed slightly to the left, due to the effect of the favorable unsteady spatial pressure gradients near the airfoil leading edge. The higher reduced frequency increased the phase lead, but not through the unsteady temporal gradients. This, again, is most probably an effect of the unsteady contribution to the centrifugal force along the streamline.

5.2 Frequency Effects for Angles of Attack Above the Steady Stall Angle

The influence of changes in the reduced frequency on the shape of the flow reversal region is observed in Figure 44. Data are presented for an angle of attack of 11 degrees and for several phase points in the oscillation period. For the low frequency case shown, the flow reversal region extended over the entire airfoil surface and the reversal region increased in height near the trailing edge. The region of flow reversal ahead of the mid-chord position grew due to the reversed flow from the trailing edge. The spatial extent of the reversal region to the airfoil trailing edge indicates that the adverse unsteady spatial gradients had a dominant effect on the flow.

The data presented in Figure 44 for the higher frequency show a reduction in size of the flow reversal region. The flow reversal near the trailing edge was entirely eliminated. The unsteady temporal gradients from equation (6) were observed to be directly proportional to reduced frequency and thus made a larger

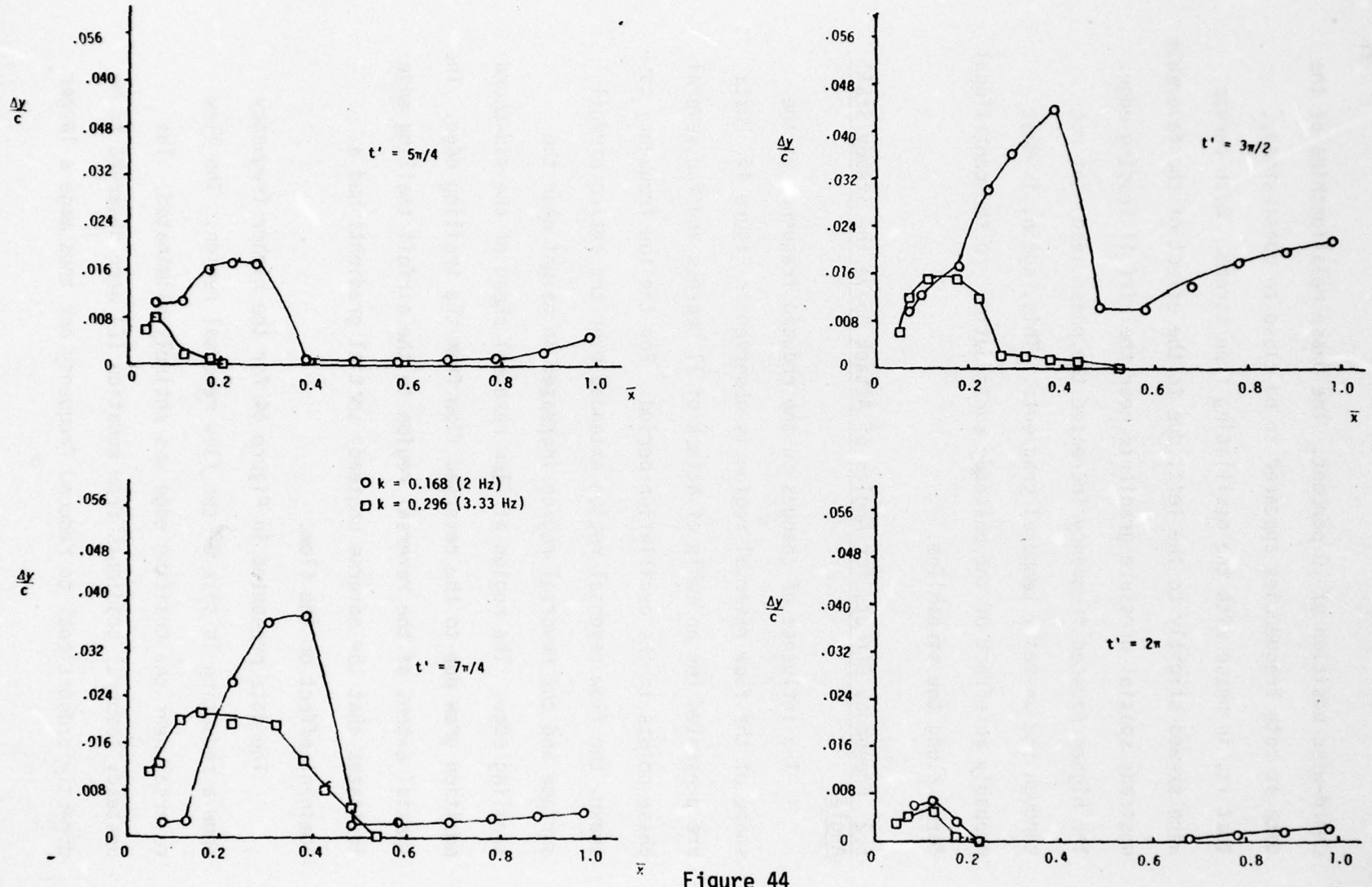


Figure 44
FREQUENCY EFFECT ON REVERSAL REGION SHAPE, α = 11 degrees

contribution to the unsteady flow response at higher frequencies, opposing the spatial gradients.

The shape of reversal data collected at an angle of attack of 12 degrees for two reduced frequencies are compared in Figure 45. The influence of the high reduced frequency is not as pronounced at this larger angle of attack since the unsteady boundary layer is separated for part of the oscillation cycle. While the maximum heights of the reversal regions for the two frequencies are closer in magnitude, the higher frequency effects are again observed to limit the chordwise extent of the reversal region. The important influence of the angle of attack increase is observed with the phase of the reversal region response and is shown below.

The influence on the phase due to changes in reduced frequency was observed to be more significant above the steady stall angle. The reversal data are compared in Figure 46 for an angle of attack of 11 degrees and several chordwise positions. The phase of the lower frequency reversed flow region is observed to lag the quasi-steady response near the leading edge, but is close to the quasi-steady phase near the trailing edge. Near the leading edge, the influence of the reduced frequency, acting through the unsteady temporal gradients, appears to be dominant and causes the phase lag. The effects of the spatial gradients are insignificant since, at this forward chord position and low amplitude ratio, the spatial gradient terms are small, either slightly negative (favorable) or slightly positive (adverse). Near the airfoil trailing edge, the spatial gradient terms are larger and oppose the frequency-induced phase lag. The higher-frequency data in Figure 46 are shown to have

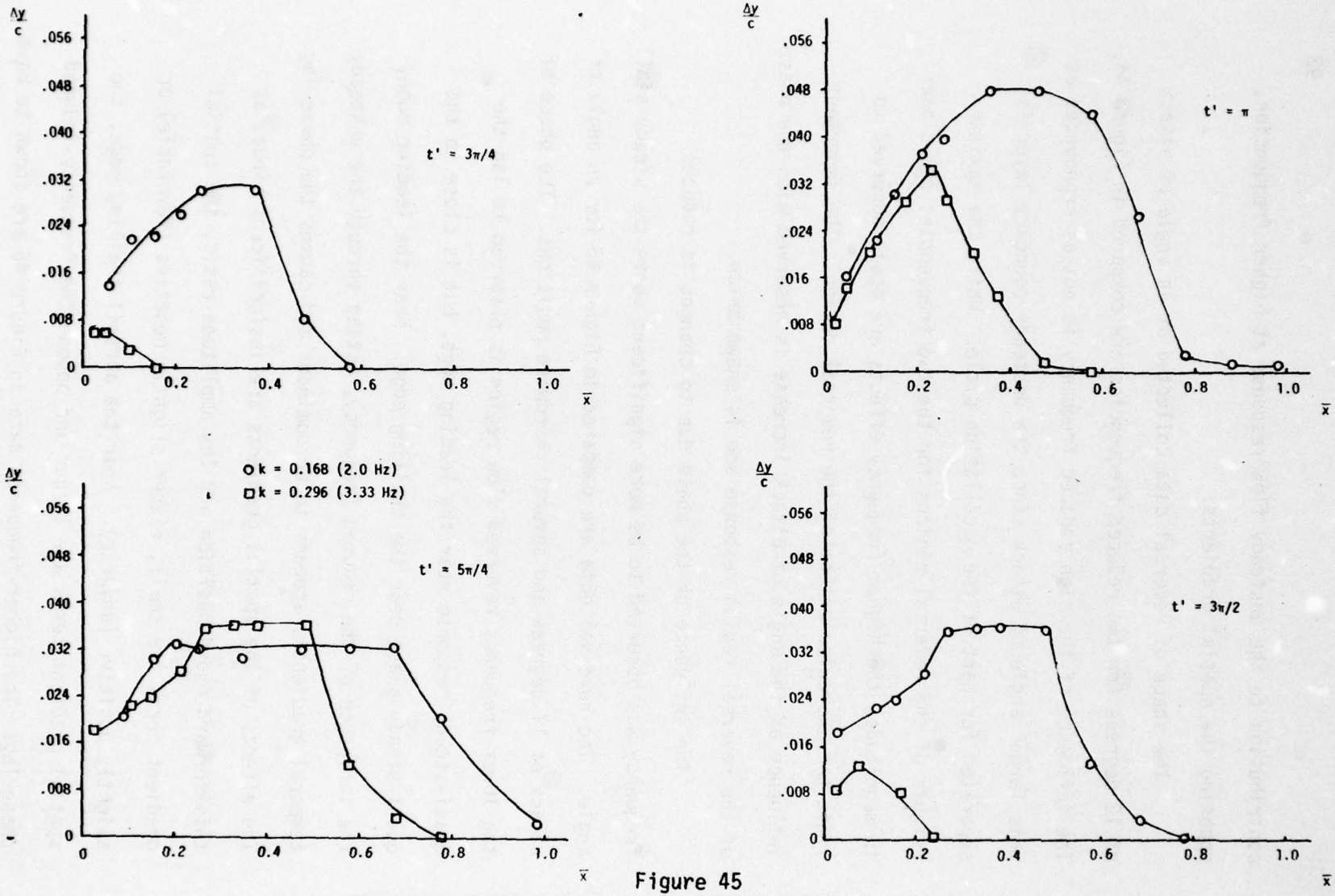


Figure 45
FREQUENCY EFFECT ON REVERSAL REGION SHAPE, α = 12 degrees

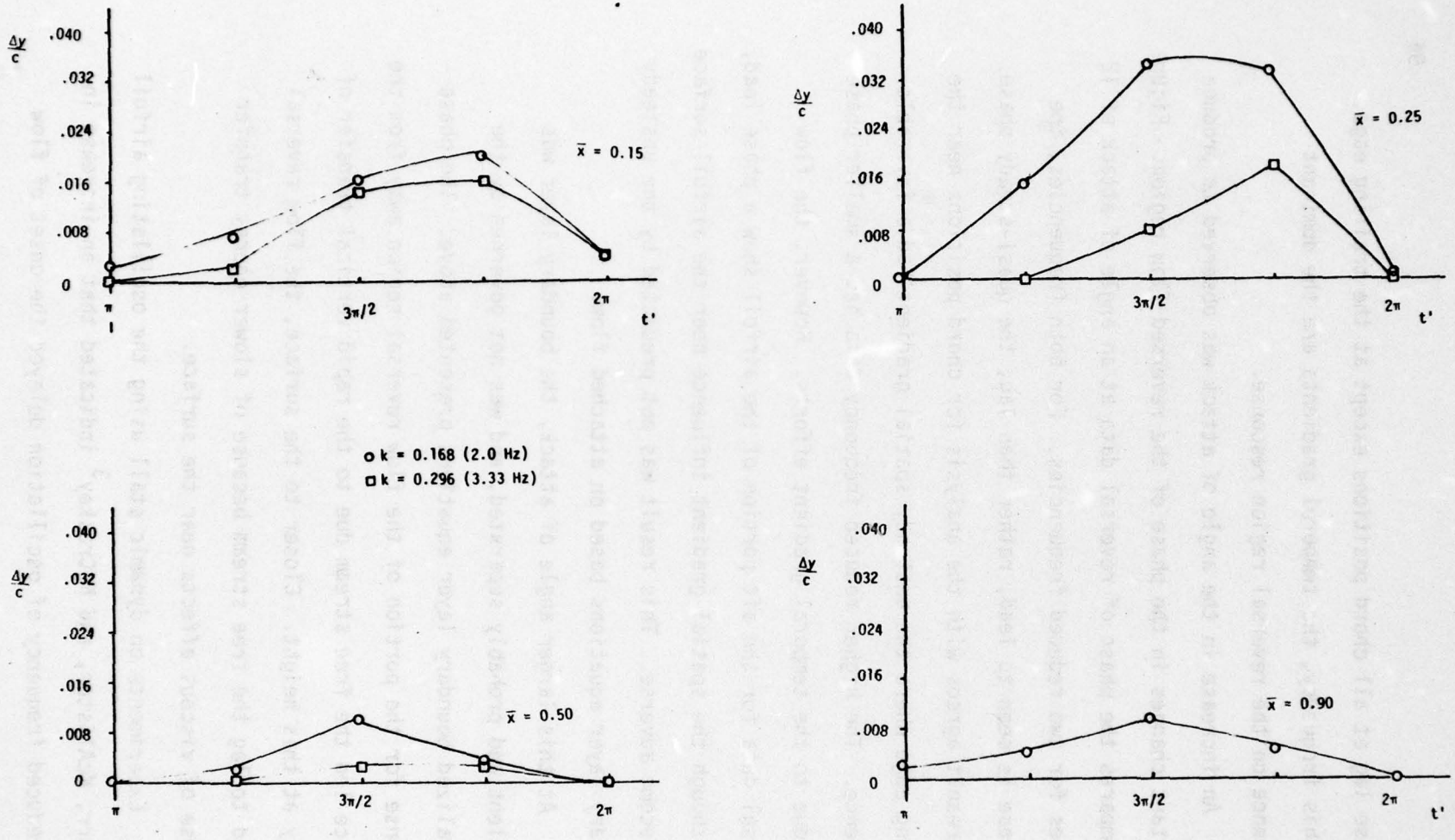


Figure 46
FREQUENCY EFFECT ON PHASE OF FLOW REVERSAL RESPONSE, α = 11 degrees

a phase lag at all chord positions except at the trailing edge. For this frequency, the temporal gradients are the dominant influence on the reversal region response.

An increase in the angle of attack was observed to produce important changes in the phase of the reversed flow region. Figure 47 compares the phase of reversal data at an angle of attack of 12 degrees for two reduced frequencies. For both frequencies, the response is seen to lead, rather than lag, the quasi-steady phase. This result agrees with the analysis for chord positions near the leading edge where the unsteady spatial gradient had a favorable influence. The higher reduced frequency data had a smaller phase lead due to the temporal gradient efforts. However, the flow reversal data for the aft portion of the airfoil show a phase lead, even though the spatial gradient influence near the airfoil surface had become adverse. This result was not predicted by the unsteady boundary layer equations based on attached flow.

At this larger angle of attack, the boundary layer was turbulent and probably separated, and was not governed by the generalized boundary layer equations presented above. The phase response for the portion of the flow reversal region away from the surface led the free stream due to the rapid vertical transfer of energy at this height. Closer to the surface, the flow reversal tended to lag the free stream because of slower energy transfer because of viscous effects near the surface.

Experiments on dynamic stall using the oscillating airfoil by Carr, McAlister, and McCroskey[3] indicated that an increase in the reduced frequency of oscillation delayed the onset of flow

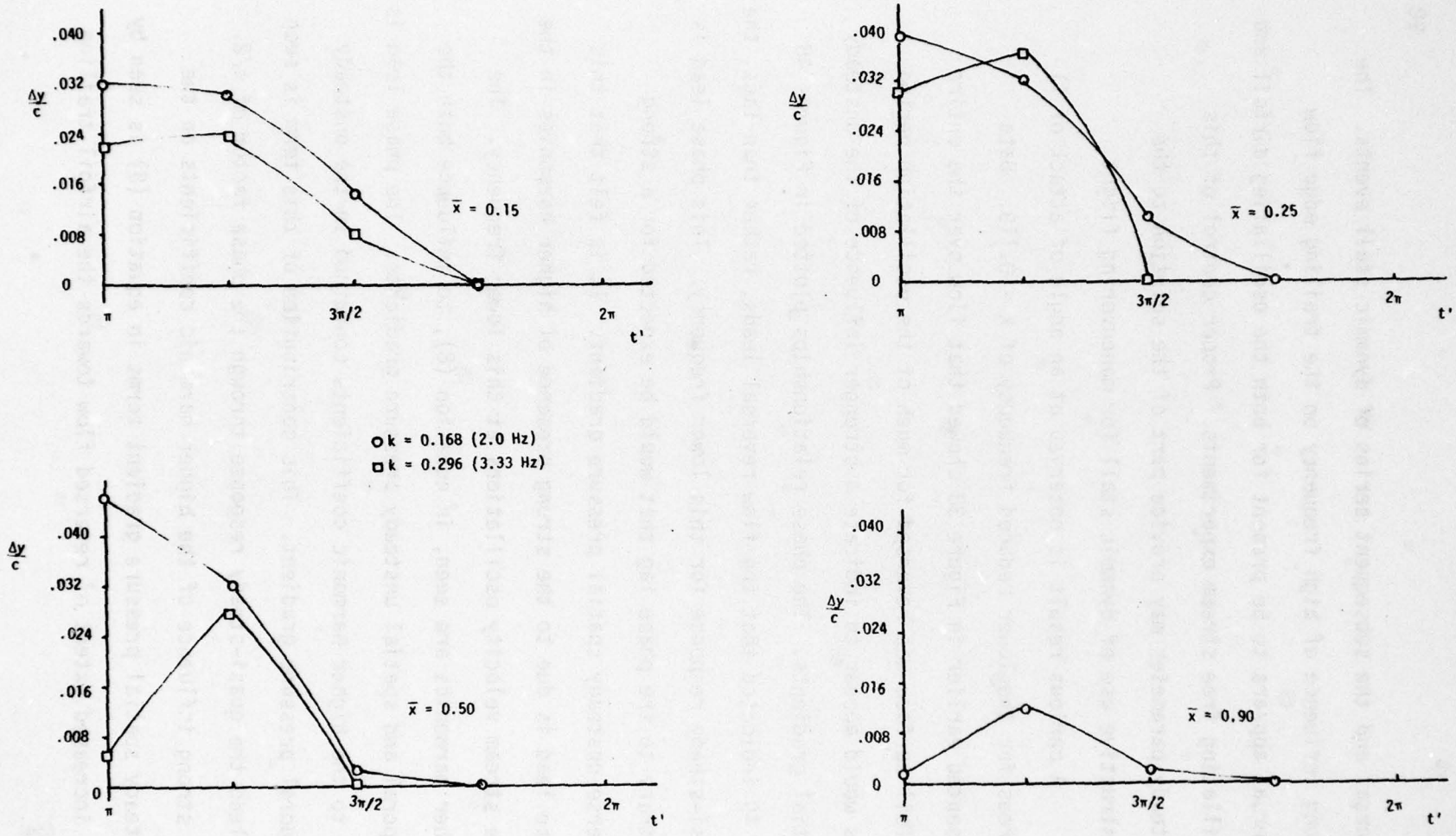


Figure 47
FREQUENCY EFFECT ON PHASE OF FLOW REVERSAL RESPONSE, α = 12 degrees

reversal and the subsequent series of dynamic stall events. The strong influence of high frequency on the trailing edge flow reversal appears to be present for both the oscillating airfoil and oscillating free stream experiments. Proper control of this unsteady parameter may provide part of the solution to the constructive use of dynamic stall for maneuvering flight.

A curious result is observed at an angle of attack of 11 degrees for the lower reduced frequency of $k = 0.119$. Data presented earlier in Figure 38 showed that flow over the entire airfoil surface was reversed for much of the oscillation period. This would appear to indicate a stronger influence of the unsteady spatial gradients. The phase relationships plotted in Figures 48 and 49 indicated that the flow reversal leads, rather than lags, the quasi-steady response for this lower frequency. This phase lead is contrary to the phase lag that would be expected for a strong adverse unsteady spatial pressure gradient. It is felt that this phase lead is due to the strong presence of higher harmonics in the free stream velocity oscillations at this lower frequency. The higher harmonics are seen, in equation (8), to influence both the temporal and spatial unsteady pressure gradients. The phase lead is due to the higher harmonic coefficients contained in the unsteady temporal pressure gradient. This contribution of this term is seen to lead the quasi-steady response through the phase factor of $\pi/2$. The strong influence of the higher harmonic coefficients on the unsteady spatial pressure gradient terms in equation (8) is seen by the increased extent of reversed flow towards the airfoil trailing edge.

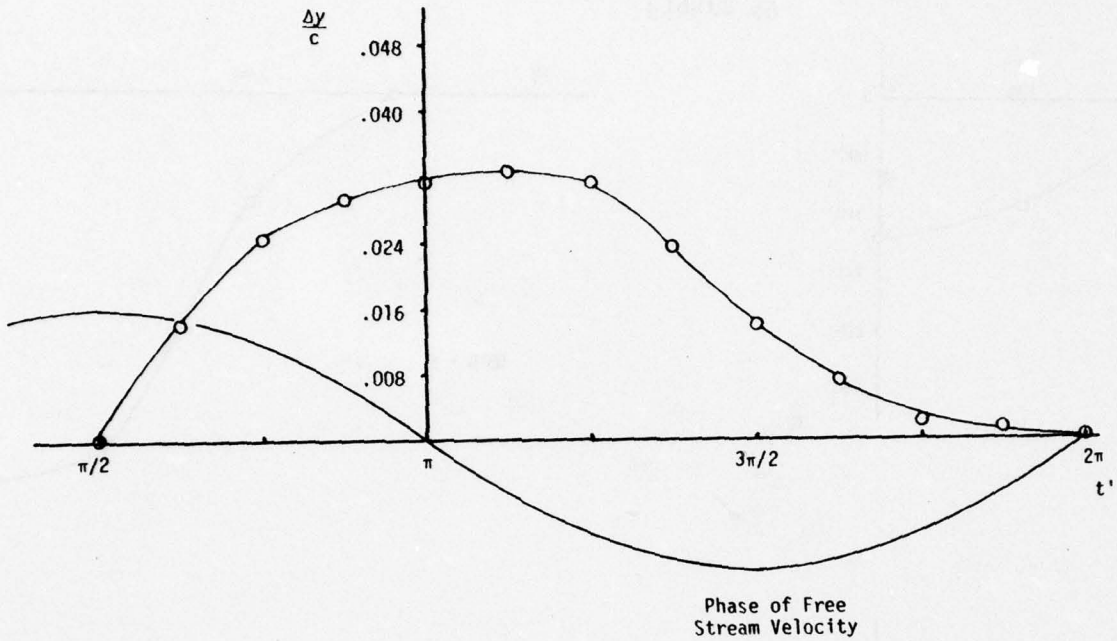


Figure 48
FREQUENCY EFFECT ON PHASE OF FLOW REVERSAL RESPONSE
α = 11 degrees, $\bar{x}$ = 0.15, k = 0.119 (1.43 Hz)

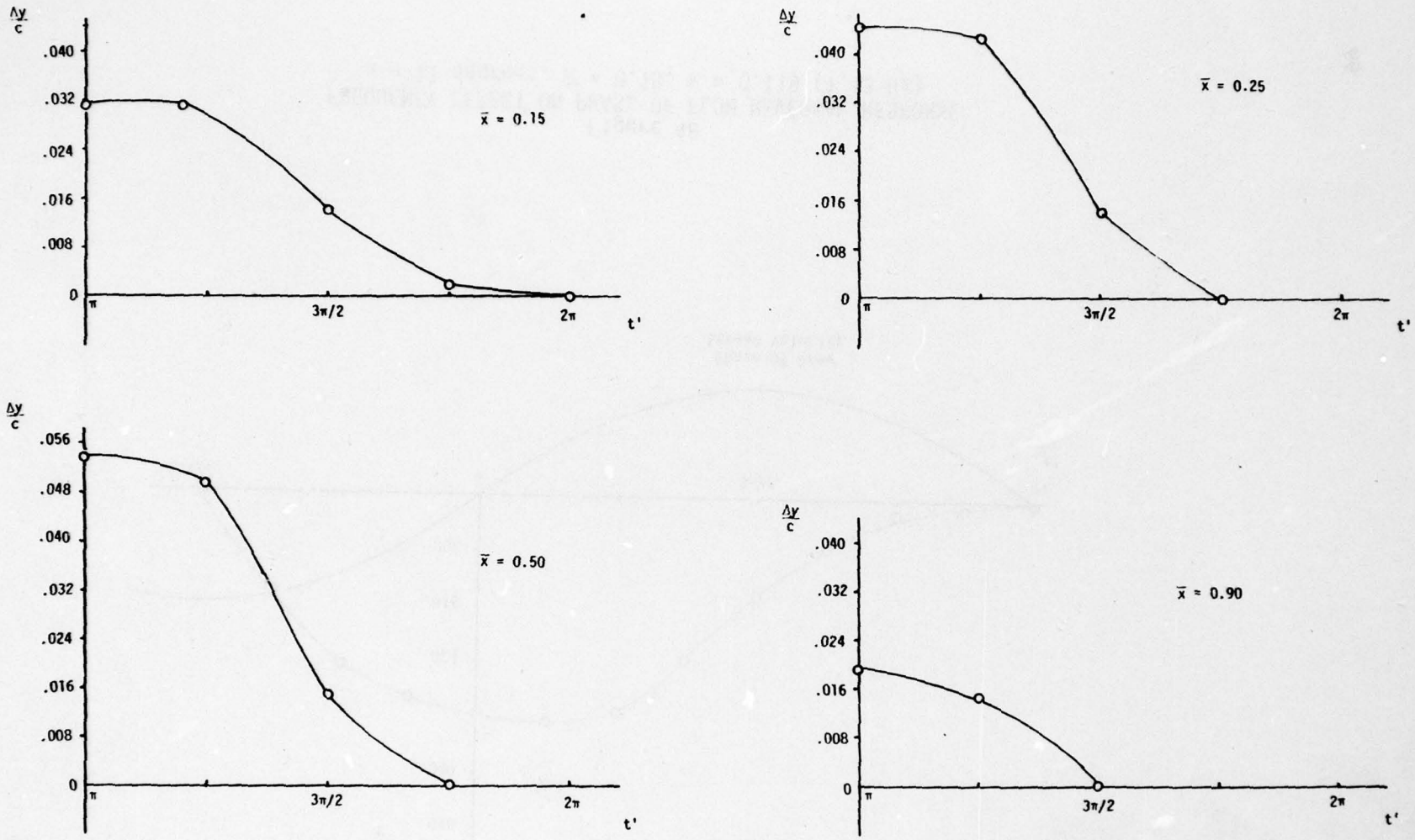


Figure 49
FREQUENCY EFFECT ON PHASE OF FLOW REVERSAL RESPONSE
α = 11 degrees, k = 0.110 (1.43 Hz)

These low frequency results emphasize the desirability of conducting unsteady experiments of this type in oscillating flows that are free from higher harmonic content. These harmonics can produce data which indicate phase leads where lags are normally observed. Also the relative influence of the spatial and temporal unsteady effects can be greatly altered by the presence of the higher harmonics.

6. OSCILLATION AMPLITUDE EFFECTS ON FLOW REVERSAL

6.1 Amplitude Effects for Angles of Attack Below the Steady Flow Stall Angle

Flow reversal data presented below show the effect on the flow reversal caused by a large increase in the amplitude ratio, N, of the oscillating free stream. The influence of this parameter is significant due to the coupling of the temporal and spatial unsteady gradients through N. This influence is shown in equation (6), which is repeated below:

$$u' \frac{\partial u'}{\partial x'} + v' \frac{\partial u'}{\partial y'} - \frac{\partial^2 u'}{\partial y'^2} = 2kN \cos(t') - 2k \frac{\partial u'}{\partial t'} + \frac{1}{U_1} \frac{dU_1}{dx'}$$

$$+ \frac{2N}{U_1} \frac{dU_1}{dx'} \sin(t') + \frac{N^2}{U_1} \frac{dU_1}{dx'} \sin^2(t')$$

$$= A_2 \sin(t' + \pi/2) - 2k \frac{\partial u'}{\partial t'} + B_2(x)$$

$$+ C_2(x) \sin(t') + D_2(x) \sin^2(t'). \qquad (6)$$

It can be noted that a combination of an amplitude ratio near unity and a low mean free stream velocity, U_1, will cause the unsteady pressure gradient terms (the last three terms on the right hand side) to dominate the boundary layer response.

This lower speed flow situation provided the data shown in Figure 50 at an angle of attack of 9 degrees for a fixed phase point of $t' = 3\pi/4$ and a mean velocity of 12 feet per second (3.66 meters per second). This mean velocity was the maximum attainable with the

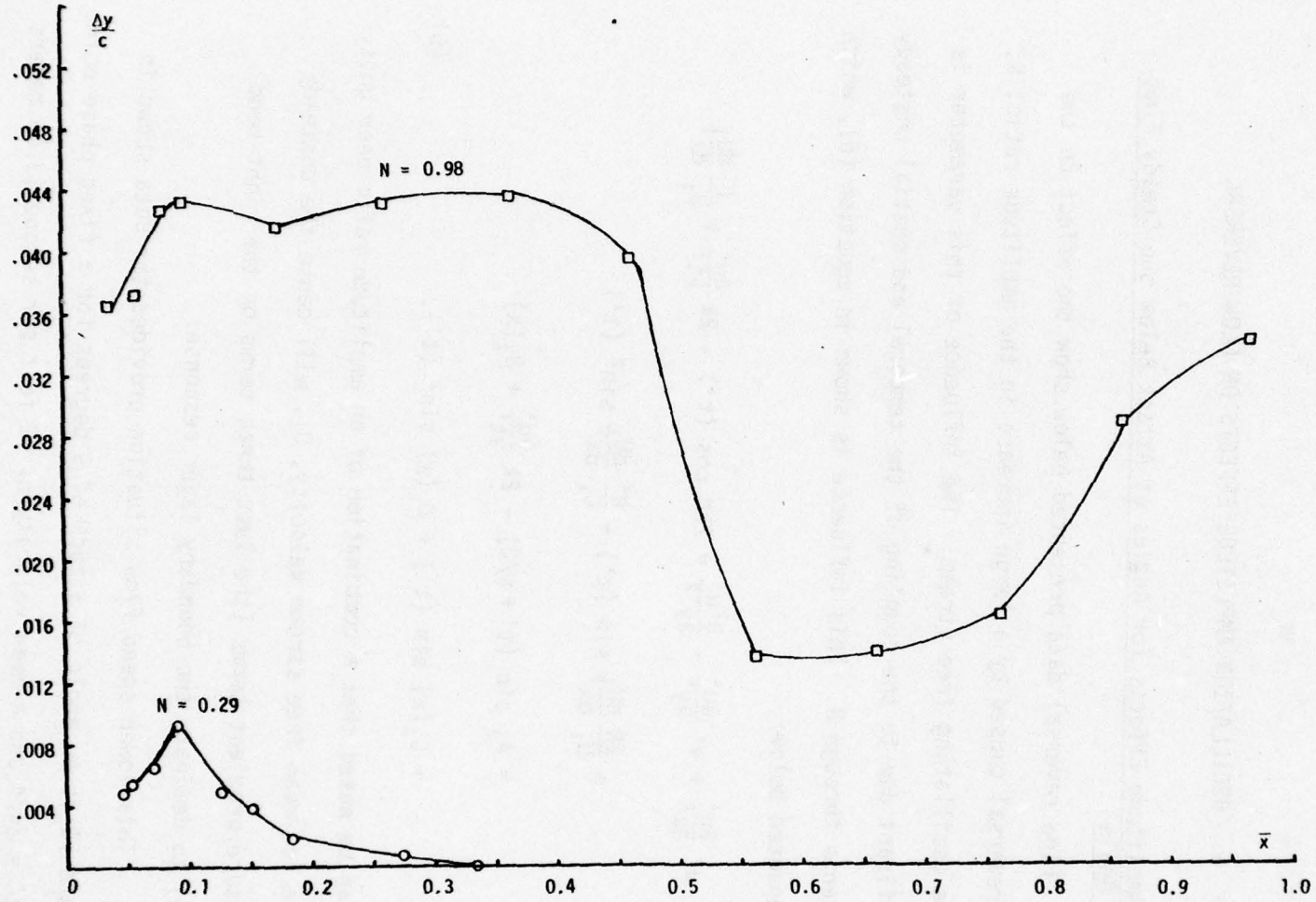


Figure 50
AMPLITUDE RATIO EFFECT ON SHAPE OF REVERSAL REGION
α = 9 degrees, t' = $3\pi/2$, U_1 = 12 ft/sec

large set of rotating vanes (set C). The mean velocity obtained with the medium size vanes (set B) was then adjusted to 12 feet per second. It is observed that, for the larger amplitude ratio, reversed flow extends to the trailing edge and appears to be separating near the trailing edge. For this flow condition, the effect of the unsteady adverse pressure gradient appears to dominate the reversed flow over the entire airfoil upper surface.

The effect of the amplitude ratio variation on the phase of the flow reversal is shown in Figure 51 for a chord position of $\bar{x} = 0.15$. The phase lead caused by the large amplitude ratio is significant and is probably due to the higher order unsteady spatial gradient in equation (6):

$$D(x) \sin (t') = \frac{D(x)}{2} [1 + \cos (2t')].$$

For the flow reversal caused by the lower amplitude ratio, the phase lead is due to the unsteady temporal gradient.

6.2 Amplitude Effects for Angles of Attack Above the Steady Flow Stall Angle

The effect of an increase in oscillation amplitude ratio on the flow reversal region shape at an angle of attack of 11 degrees was not as pronounced as for the lower angle of attack. Figure 52 shows that, for a phase point of $t' = 3\pi/2$, the reversal regions produced by the two different amplitude ratios did not differ greatly. The reversed flow region extends to the trailing edge for both cases, and is actually thicker for the lower amplitude ratio. This increased thickness is probably due to the presence of a larger region of separated flow for the lower amplitude ratio case.

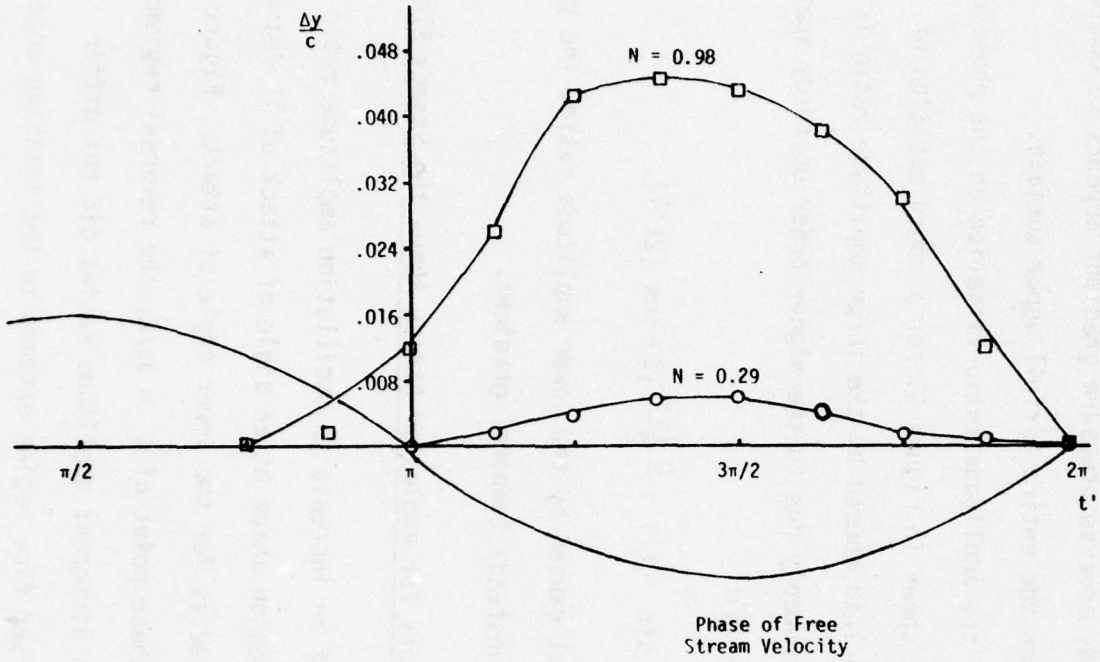


Figure 51
AMPLITUDE RATIO EFFECT ON PHASE OF REVERSAL REGION
α = 9 degrees, $\bar{x}$ = 0.15

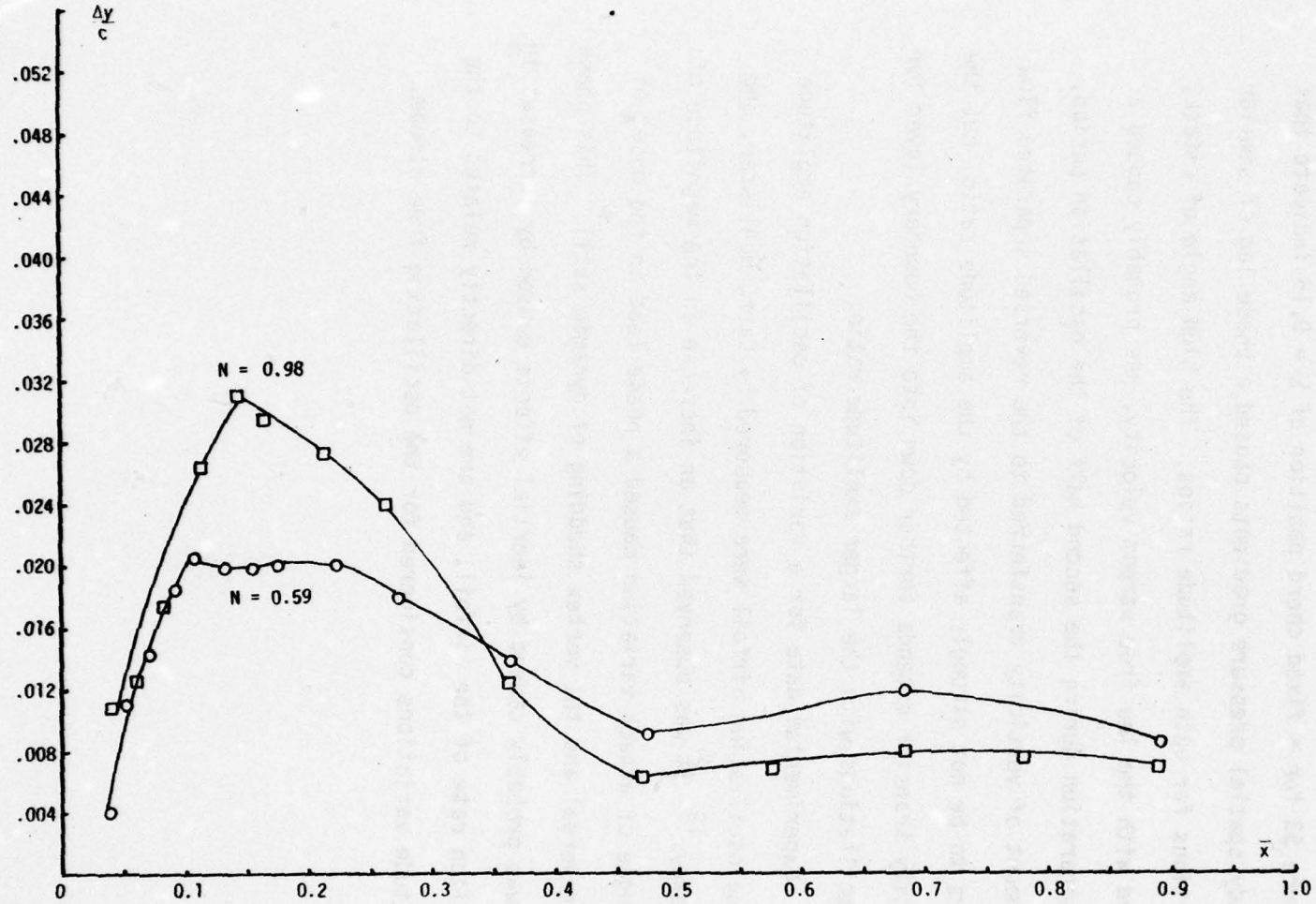


Figure 52
AMPLITUDE RATIO EFFECT ON SHAPE OF REVERSAL REGION
α = 11 degrees, t' = $3\pi/2$, U_1 = 12 ft/sec

For this angle of attack, the increased amplitude variation had a smaller effect on the phase of the flow reversal. Data shown in Figure 53 for a fixed chord position of $\bar{x} = 0.15$ indicate that unsteady spatial pressure gradients caused a phase lag of similar proportions for both amplitude ratios. The high angle of attack, coupled with the low free stream velocity, has probably caused a flow separation during the second half of the oscillation period. The amount of vorticity transferred to the reversed separated flow appears to be not strongly affected by the amplitude ratio, but the vorticity transfer extends further down into the boundary layer for the oscillations with the larger amplitude ratio.

Experimental data for a variation of oscillation amplitude for the oscillating airfoil were measured by Carr, McAlister, and McCroskey.[19] It was observed that an increase in the magnitude of the angle of attack variation caused a phase lead in the onset of flow reversal and the vortex shedding of dynamic stall. This phase lead was probably caused by inertial effects caused by increases in the pitch rate of the airfoil, and are not directly related to the amplitude variations considered for the oscillating free stream.

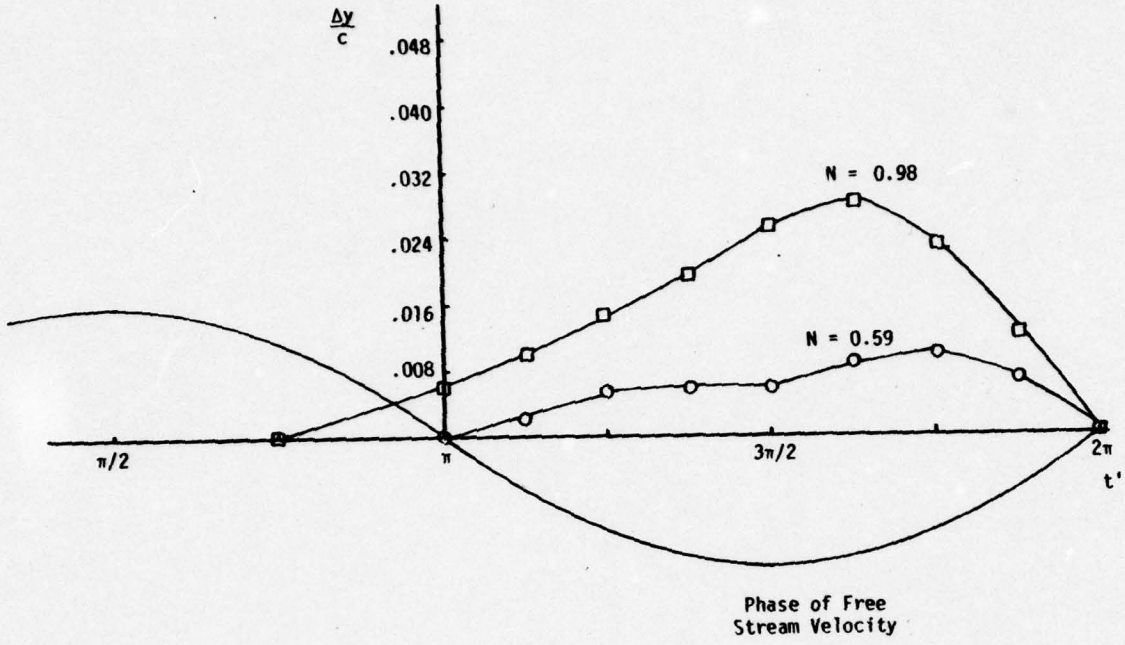


Figure 53
AMPLITUDE RATIO EFFECT ON PHASE OF REVERSAL REGION
α = 11 degrees, $\bar{x}$ = 0.15

7. CONCLUSIONS

The onset of unsteady boundary layer flow reversal was measured above the surface of a stationary NACA 0012 airfoil in a longitudinally oscillating flow. The response of the flow reversal region to the influence of the flow unsteadiness was found to be similar to the flow reversal observed during dynamic stall. Previous dynamic stall experiments using oscillating airfoils have produced flow reversal regions which originated near the airfoil trailing edge and moved upstream. However, this experiment produced flow reversal regions which initially appeared near the airfoil leading edge and spread downstream.

It is shown that the influence of unsteady flow parameters on the onset of flow reversal in the two types of experiments are similar. Using a fixed airfoil experiment, the flow reversal measurements above the surface of the airfoil can be more easily and more accurately obtained.

Preliminary measurements of flow reversal in steady flow indicated a small reversal region near the airfoil leading edge, which represented part of the laminar separation bubble. These measurements also determined the steady-flow stall angle of attack, which provided a division between the different types of reversal phenomena observed in unsteady flow.

At both low and high angles of attack, the unsteady effects were seen to be caused by unsteady temporal and spatial quantities. Variations in the reduced frequency and the amplitude ratio of the oscillating free stream velocity were observed to produce changes in the relative influence of the temporal and spatial unsteady gradients. The influence of variations of oscillation frequency and amplitude were observed to be strongly coupled, because of the nature of the unsteady boundary layer equations. The amplitude effects were seen to depend strongly on whether the amplitude ratio, N, was near unity. These amplitude effects had not been previously measured experimentally for the reversed flow region above the airfoil surface.

For angles of attack below the steady stall angle, the flow reversal response was close to quasi-steady at low amplitude ratios. An increased amplitude ratio greatly increased the size of the reversed flow region and caused it to lag the quasi-steady phase. No significant unsteady effects were noted for variations of reduced frequency at this angle of attack.

For angles of attack greater than the steady flow stall angle, the unsteady spatial and temporal gradients cause departures from the quasi-steady response. The phase and spatial extent of the reversed flow region were seen to be strong functions of reduced frequency, amplitude ratio, and angle of attack, with the response normally lagging the quasi-steady flow, except at high angles of attack. The influence of higher harmonic content in the power spectra of the free stream velocity oscillations is observed

to contribute to a response which leads the phase of the quasi-steady flow.

The shape of the reversed flow region noted at various times in the oscillation period lends credence to the reversal and separation model of Sears and Telionis.[5] For certain combinations of the unsteady flow parameters, the observed thickening of the reversed flow region near the trailing edge may indicate flow separation. Increased oscillation frequencies appear to inhibit separation near the trailing edge. Without additional data on the velocity profiles and displacement thicknesses throughout the boundary layer, no further validation of this model can be made.

Although the split-film sensor proved valuable for measuring the onset of flow reversal, it was unable to provide accurate measurements of the magnitude of the reversed flow velocity. It is recommended that the velocity magnitude and direction in the reversed flow region be measured using a split-film sensor with the plane of the split parallel to the longitudinal flow axis. Also, another measurement device, such as a laser doppler velocimeter, might be used.

The higher harmonic content of the free stream velocity oscillations was reduced by adjustment of the bypass flow of the rotating vane device. The best operating conditions, with a high reduced frequency and a small amplitude ratio, provided a second harmonic rejection of approximately 48 db. Other combinations of flow parameters used in the experiment produced second harmonic rejections of at least 10 db. It is recommended that a feedback control system for the motor drive similar to that used by Simpson[15]

be used to greatly improve the harmonic rejection ability of this unsteady flow device.

REFERENCES

1. Saxena, L. S., Fejer, A. A., Morkovin, M. V., "Features of Unsteady Flows over Airfoils," Proc. AGARD Symp. on Unsteady Aerodynamics, Ottawa, September 26-28, 1977.

2. Lighthill, M. J., "The Response of Laminar Skin Friction and Heat Transfer to Fluctuations in the Stream Velocity," Proc. Roy. Soc. A, Vol. 224, 1954, p. 1.

3. Lin, C. C., "Motion in the Boundary Layer with a Rapidly Oscillating External Flow," Proc. of 4th Intl. Congr. Appl. Mech., Vol. 4, 1966, p. 155.

4. Nickerson, R. H., "The Effect of Free-Stream Oscillations on the Laminar Boundary Layers on a Flat Plate," Ph.D. Thesis, Massachusetts Institute of Technology, 1957.

5. Karlsson, S. K. F., "An Unsteady Turbulent Boundary Layer," J. Fluid Mech., Vol. 5, 1959, p. 622.

6. Hill, P. G., Stenning, A. H., "Laminar Boundary Layers in Oscillatory Flow," Trans. ASME, Ser. D, J. of Basic Engr., Vol. 82, September 1960, p. 593.

7. Cousteix, J., Houdeville, R., Desopper, A., "Resultats Experimentaux et Methodes de Calcul Relatifs aux Couches Limites Turbulentes en Ecoulement Instationnaire," Proc. AGARD Symp. on Unsteady Aerodynamics, Ottawa, September 26-28, 1977.

8. Patel, M. H., "On Laminar Boundary Layers in Oscillatory Flow," Proc. Roy. Soc. A, Vol. 347, 1975, pp. 99-123.

9. Patel, M. H., Nash, J. F., "Unsteady Turbulent Boundary Layers with Flow Reversal," Proc. Symp. Unsteady Aerodynamics, Tucson, March 18-20, 1975, pp. 155-190.

10. Telionis, D. P., Tsahalis, D. T., Werle, M. J., "Numerical Investigation of Unsteady Boundary-Layer Separation," Physics of Fluids, Vol. 16, No. 7, July 1975, pp. 968-973.

11. Sears, W. R., Telionis, D. P., "Boundary Layer Separation in Unsteady Flow," SIAM J. on Appl. Math, Vol. 28, No. 1, January 1975, pp. 215-235.

12. Nash, J. F., Scruggs, R. M., "Unsteady Boundary Layers with Reversal and Separation," Proc. AGARD Symp. on Unsteady Aerodynamics, Ottawa, September 26-28, 1977.

13. Nash, J. F., "Further Studies of Unsteady Boundary Layers with Flow Reversal," NASA Contractor Report CR-2767, December 1976.

14. Despard, R. A., Miller, J. A., "Separation in Oscillating Laminar Boundary-Layer Flows," J. Fluid Mech., Vol. 47, Part 1, 1971, pp. 21-31.

15. Simpson, R. L., "Features of Unsteady Turbulent Boundary Layers as Revealed from Experiments," Proc. AGARD Symp. on Unsteady Aerodynamics, Ottawa, September 26-28, 1977.

16. Kennison, R. C., "An Experimental Study of the Effect of Oscillatory Flow on the Separation Region in a Turbulent Boundary Layer," Proc. AGARD Symp. on Unsteady Aerodynamics, Ottawa, September 26-28, 1977.

17. McCroskey, W. J., Philippe, J. J., "Unsteady Viscous Flow on Oscillating Airfoils," AIAA J., Vol. 13, No. 1, January 1975, pp. 71-79.

18. McCroskey, W. J., Carr, L. W., McAlister, K. W., "Dynamic Stall Experiments on Oscillating Airfoils," AIAA J., Vol. 14, No. 1, January 1976, pp. 57-63.

19. Carr, L. W., McAlister, K. W., McCroskey, W. J., "Analysis of the Development of Dynamic Stall Based on Oscillating Airfoil Experiments," NASA Technical Note D-8382, January 1977.

20. Rebont, J., Maresca, C., Favier, D., Valensi, J., "Recollement Dynamique sur un Profile d'Aile en Mouvement de Tamis - Influence des Parametres d'Oscillation," Proc. AGARD Symposium on Unsteady Aerodynamics, Ottawa, September 26-28, 1977.

21. Despard, R. A., "Laminar Boundary Layer Separation in Oscillating Flow," Ph.D. Thesis, Naval Postgraduate School, June 1969.

22. Morkovin, M. V., Loehrke, R. I., Fejer, A. A., "On the Response of Laminar Boundary Layers to Periodic Changes in Free-Stream Speed," Proc. Symp. on Recent Research on Unsteady Boundary Layers, Quebec, 1972.

23. Charnay, G., Mathieu, J., "Periodic Flow in a Wind Tunnel Produced by Rotating Shutters," J. Fluid Engr., Trans. ASME, Ser. I, Vol. 98, No. 2, June 1976, pp. 278-283.

24. Francis, M. S., "An Experimental Investigation of Wing Trailing Vortex Formation," F. J. Seiler Research Laboratory TR-76-0013, August 1976.

25. Bank, W., "Build Your Own Constant Temperature Hot-Wire Anemometer," Electronic Design News, August 1972.

26. King, L. V., "On the Convection of Heat from Small Cylinders in a Stream of Fluid: Determination of the Convective Constants of Small Platinum Wires, With Applications to Hot-Wire Anemometry," Phil. Trans. of Roy. Soc., 214A, 1914, pp. 373-432.

27. McMichael, J. M., "A Study of the Axisymmetric Turbulent Wake Generated by Co-Flowing Incompressible Streams," Ph.D. Thesis, University of Colorado, 1971.

28. "TSI Split Film Sensor Calibration and Applications," Technical Bulletin TB20, TSI, Inc., Saint Paul, Minn., 1977.

29. "System Operating Manual - Fourier Analyzer System 5450A/5452A," Hewlett-Packard Corp., Santa Clara, Calif., 1970.

30. McMichael, J. M., Private Communication, December 18, 1975.

31. Chang, P. K., Separation of Flow, Oxford, Permagon Press, 1970, pp. 326-327.

32. McCroskey, W. J., "Some Current Research in Unsteady Fluid Dynamics," Trans. ASME, J. Fluids Engr., March 1977, pp. 8-39.

APPENDIX A

1. PROGRAM 1 FOR TI-58 PROGRAMMABLE CALCULATOR

Description:

This program computes the position of the probe with respect to the airfoil trailing edge at a given angle of attack.

Instructions:

	Enter	Press	Display
1. Enter angle of attack (α) in degrees	α	STO 00	α
2. Enter X_o, position of trailing edge, in inches	X_o	STO 01	X_o
3. Enter Y_o, position of trailing edge, in inches	Y_o	STO 02	Y_o
4. Enter X-traverse	X_{trav}	A	X from trailing edge
		B	$\overline{X}$ from leading edge
5. Enter Y-traverse	Y_{trav}	C	Y from trailing edge

Program Steps:

Location	Code	Key
0	76	2nd-LBL
1	11	A
2	75	-
3	43	RCL
4	01	01
5	95	=
6	94	+/-
7	42	STO
8	03	03
9	91	R/S
10	76	2nd-LBL
11	12	B
12	43	RCL
13	03	03
14	55	÷
15	53	(
16	43	RCL
17	00	00
18	39	2nd-COS
19	54	)
20	55	÷
21	01	1
22	00	0
23	95	=
24	75	-
25	01	1
26	95	=
27	94	+/-
28	42	STO
29	04	04
30	91	R/S
31	76	2nd-LBL
32	13	C
33	75	-
34	43	RCL
35	02	02
36	95	=
37	42	STO
38	05	05
39	91	R/S
40	81	RST

2. PROGRAM 2 FOR TI-58 PROGRAMMABLE CALCULATOR

Description:

This program computes the height of the probe above the airfoil surface at a given probe position from the trailing edge and at a given angle of attack. The airfoil surface coordinates of the NACA 0012 profile are stored in calculator memories, The input probe positions were calculated using Program 1.

Instructions:

	Enter	Press	Display
1. Enter angle of attack (α)	α	STO 00	α
2. Enter iteration counter	37	STO 06	37
3. Enter X_{TE} - from Program 1	X_{TE}	A	
4. Enter $\overline{X}_{LE}$ - from Program 1	$\overline{X}_{LE}$	B	
5. Enter Y_{TE} - from Program 1	Y_{TE}	C	ΔY

Store airfoil surface coordinates below in memories indicated:

Memory	Data	Memory	Data	Memory	Data	Memory	Data
20	0.0	30	.400	40	.2615	50	.4563
21	.0125	31	.500	41	.3555	51	.3664
22	.0250	32	.600	42	.4200	52	.2623
23	.050	33	.700	43	.4683	53	.1448
24	.075	34	.800	44	.5345	54	.0807
25	.100	35	.900	45	.5737	55	.0126
26	.150	36	.950	46	.5941		
27	.200	37	1.00	47	.6002		
28	.250	38	0.0	48	.5803		
29	.300	39	.1894	49	.5294		

Program Steps:

Location	Code	Key	Location	Code	Key
0	76	2nd-LBL	50	75	-
1	11	A	51	73	RCL 2nd-IND
2	42	STO	52	07	7
3	03	03	53	95	=
4	76	2nd-LBL	54	55	÷
5	12	B	55	53	(
6	42	STO	56	73	RCL 2nd-IND
7	04	04	57	06	6
8	76	2nd-LBL	58	75	-
9	13	C	59	73	RCL 2nd-IND
10	42	STO	60	07	7
11	05	05	61	54	)
12	97	2nd-DSZ	62	95	=
13	06	6	63	65	x
14	40	2nd-IND	64	53	(
15	06	6	65	73	RCL 2nd-IND
16	32	$x \lessgtr t$	66	08	8
17	43	RCL	67	75	-
18	04	04	68	73	RCL 2nd-IND
19	22	INV	69	09	9
20	77	2nd-$x \geq t$	70	54	)
21	15	E	71	85	+
22	91	R/S	72	73	RCL 2nd-IND
23	76	2nd-LBL	73	09	9
24	15	E	74	95	=
25	43	RCL	75	42	STO
26	06	06	76	10	10
27	75	-	77	73	RCL 2nd-IND
28	01	1	78	08	8
29	95	=	79	75	-
30	42	STO	80	73	RCL 2nd-IND
31	07	07	81	09	9
32	73	RCL 2nd-IND	82	95	=
33	06	6	83	55	÷
34	85	+	84	53	(
35	01	1	85	73	RCL 2nd-IND
36	08	8	86	06	6
37	95	=	87	75	-
38	42	STO	88	73	RCL 2nd-IND
39	08	08	89	07	7
40	73	RCL 2nd-IND	90	54	)
41	07	7	91	95	=
42	85	+	92	55	÷
43	01	1	93	01	1
44	08	8	94	00	0
45	95	=	95	95	=
46	42	STO	96	22	INV
47	09	09	97	30	2nd-TAN
48	43	RCL	98	42	STO
49	04	04	99	11	11

Location	Code	
100	09	9
101	00	0
102	75	-
103	43	RCL
104	11	11
105	95	=
106	38	2nd-SIN
107	42	STO
108	12	12
109	09	9
110	00	0
111	75	-
112	43	RCL
113	00	00
114	85	+
115	43	RCL
116	11	11
117	9-	=
118	38	2nd-SIN
119	35	1/x
120	65	x
121	43	RCL
122	12	12
123	95	=
124	65	x
125	43	RCL
126	10	10
127	95	=
128	65	+
129	53	(
130	43	RCL
131	03	03
132	65	x
133	53	(
134	43	RCL
135	00	00
136	30	2nd-TAN
137	54	)
138	54	)
139	75	-
140	43	RCL
141	05	05
142	95	=
143	94	+/-
144	91	R/S
145	81	RST

APPENDIX B

UNSTEADY FLOW ANALYSIS

This simplified analysis of the unsteady wind tunnel flow with identical main-flow and bypass rotating vanes was adapted from the analysis of McMichael.[30] It shows the adjustment required for the bypass port to obtain, ideally, only the add harmonic components of the oscillating velocity. An extended analysis for the case where the main-flow and bypass vanes are not the same size shows that, while the equations are a great deal more complex, optimization is still possible.

The momentum equation for the wind tunnel flow may be written

$$\frac{\partial u}{\partial t} + u \frac{\partial u}{\partial x} = - \frac{\partial}{\partial x}\left(\frac{P}{\rho}\right) - \gamma(x)\, u^2$$

where $\gamma(x)$ represents losses due to the friction of the walls. The mass balance is:

$$Q(x,t) = A(x)\ u(x,t)$$

where A(x) is the local cross-sectional area. Substituting,

$$\frac{1}{A(x)} \frac{\partial Q}{\partial t} + \frac{Q^2}{2} \frac{\partial}{\partial x}\left(\frac{1}{A^2(x)}\right) + \frac{Q^2 \gamma(x)}{A^2(x)} = - \frac{\partial}{\partial x}\left(\frac{P}{\rho}\right).$$

The wind tunnel stations and mass flows are defined in Figure 7. Integrating between arbitrary stations m and n yields:

$$(P_m - P_n) = \alpha_{mn} \frac{\partial Q}{\partial t} + K_{mn}\, Q^2$$

where:

$$\alpha_{mn} = \rho \int_m^n \frac{dx}{A(x)}$$

$$K_{mn} = \frac{P}{2}\left[\frac{1}{A^2(x)}\right]_m^n + P \int_m^n \frac{\gamma(x)}{A^2(x)}\, dx.$$

Knowing that $P_1 = P_8 = Pa$ (atmospheric pressure) and assuming quasi-steady, high Reynolds number flow, the pressure differences at each station are:

$$P_1 - P_2 = \alpha_{12}\, Q_1 + K_{12}\, Q_1^2$$

$$P_3 - P_4 = \alpha_{34}\, Q_1 + K_{34}\, Q_1^2$$

$$P_5 - P_6 = \alpha_{56}\, (\dot{Q}_1 + \dot{Q}_2) + K_{56}\, (Q_1 + Q_2)^2$$

$$P_7 - P_8 = \alpha_{78}\, (\dot{Q}_1 + \dot{Q}_2) + K_{78}\, (Q_1 + Q_2)^2$$

also:

$$P_2 - P_3 = C_{23}\, Q_1^2$$

$$P_4 - P_5 = C_{45}\, Q_1^2$$

$$P_4 - P_5 = C_{a5}\, Q_2^2$$

where C_{mn} is the pressure drop coefficient across the indicated mechanical devices. Also:

$$P_6 - P_7 = -P_f \text{ (fan pressure rise).}$$

Then, McMichael writes:

$$(P_1 - P_5) = (P_a - P_5) = (\alpha_{12} + \alpha_{34})\dot{Q}_1 + (K_{12} + K_{34} + C_{23} + C_{45})Q_1^2.$$

Now define

$$\alpha_1 = (\alpha_{12} + \alpha_{34})$$

$$K_1 = (K_{12} + K_{34} + C_{23})$$

$$F_1 = C_{45}$$

$$F_2 = C_{a5}.$$

Combining these terms gives

$$F_2 Q_2^2 = \alpha_1 \dot{Q}_1 + (K_1 + F_1) Q_1^2 .$$

The adjustable bypass ports can be opened a distance L and essentially add a resistance $K_2(L)$ so that

$$P_a - P_5 = (K_2 + F_2) Q_2^2 .$$

Thus

$$(P_a - P_5) = (K_2 + F_2) Q_2^2 = \alpha_1 \dot{Q}_1 + (K_1 + F_1) Q_1^2 .$$

Note that $\alpha_2 \dot{Q}_2$ was considered negligible because of the short distance between the bypass port and bypass vanes. For the fan duct exit

$$\begin{aligned} (P_5 - P_a) &= (P_5 - P_6) + (P_6 - P_7) + (P_7 - P_8) \\ &= (\alpha_{56} + \alpha_{78})(\dot{Q}_1 + \dot{Q}_2) + (K_{56} + K_{78})(Q_1 + Q_2)^2 - P_f \end{aligned}$$

define

$$K_3 = K_{56} + K_{78}$$

$$\alpha_3 = \alpha_{56} + \alpha_{78} .$$

Collecting the previous relations yields

$$P_a - P_5 = \begin{cases} (K_2 + F_2) Q_2^2 & \text{(B-1)} \\ (K_1 + F_1) Q_1^2 + \alpha_1 \dot{Q}_1 & \text{(B-2)} \\ -K_3 (Q_1 + Q_2)^2 - \alpha_3 (\dot{Q}_1 + \dot{Q}_2) + P_f . & \text{(B-3)} \end{cases}$$

A reference state for the tunnel flow may be defined using the time average of the vane pressure drop coefficients and mass flows at a given mean tunnel velocity. Then,

$$F_1(\phi) = F_{10} + f_1(t)$$

$$F_2(\phi) = F_{20} + f_2(t)$$

$$Q_1(t) = Q_{10} + q_1(t)$$

$$Q_2(t) = Q_{20} + q_2(t)$$

where

$$\overline{F_1(\phi)} = F_{10}$$

$$\overline{F_2(\phi)} = F_{20}$$

$$\overline{Q_1(t)} = Q_{10}$$

$$\overline{Q_2(t)} = Q_{20}$$

and

$$\overline{f_1(t)} = \overline{f_2(t)} = \overline{q_1(t)} = \overline{q_2(t)} = 0$$

also,

$$P_f = P_{f_0} + \Delta P_f$$

and

$$\frac{q_1}{Q_{10}} \sim \frac{q_2}{Q_{20}} \sim \frac{\Delta P_f}{P_{f_0}} << 1.$$

The reference state (time average) of equation s (1), (2), and (3) show

$$(K_2 + F_{20})Q_{20}^2 = (K_1 + F_{10})Q_{10}^2 \qquad \text{(B-4)}$$

$$(K_1 + F_{10})Q_{10}^2 = P_{f_0} - K_3(Q_{10} + Q_{20})^2. \qquad \text{(B-5)}$$

Equations (B-1), (B-2), and (B-3) are then linearized about the reference state (second-order-terms dropped):

$$2(K_2 + F_{20})Q_{20}q_2 + f_2Q_{20}^2 = 2(K_1 + F_{10})Q_{10}q_1 + f_1Q_{10}^2 + \alpha_1\dot{q}_1 \qquad \text{(B-6)}$$

$$2(K_2 + F_{20})Q_{20}q_2 + f_2Q_{20}^2 = \Delta P_f - \alpha_3(\dot{q}_1 + \dot{q}_2) - K_3(Q_{10} + Q_{20})(q_1 + q_2). \tag{B-7}$$

For the simplified case where the main-flow and bypass vanes are identical, equations (B-4) and (B-5) show that $F_{10} = F_{20} \equiv F_O$. To balance the reference state flow rates, K_2 is adjusted so that $K_1 = K_2$, so that $Q_{10} = Q_O/2$. Then define:

$$R_1 = K_1 + F_{10}$$

$$R_2 = K_2 + F_{20}$$

$$r^2 = R_1/R_2$$

$$Q_{20} = rQ_{10}.$$

The equations (B-6) and (B-7) become:

$$2rR_2Q_{10}q_2 + f_2r^2Q_{10}^2 = 2R_1Q_{10}q_1 + f_1Q_{10}^2 + \alpha_1\dot{q}_1 \tag{B-8}$$

$$= \Delta P_f - \alpha_3(\dot{q}_1 + \dot{q}_2) - 2K_3Q_{10}(1 + r)(q_1 + q_2)$$

for simplification, ΔP_f may be approximated as

$$\Delta P_f \simeq \beta(q_1 + q_2)$$

where β is a constant. Equation (B-8) may be non-dimensionalized using

$$R_1 = R_2 = R'$$

$$\hat{f}_1 = f_1/2R'$$

$$\hat{f}_2 = f_2/2R'$$

$$\hat{q}_1 = q_1/(Q_O/2)$$

$$\hat{q}_2 = q_2/(Q_O/2)$$

which gives

$$2\hat{q}_2 + 2\hat{f}_2 = 2\hat{q}_1 + 2\hat{f}_1 + \frac{2\alpha_1}{RQ_o}\dot{\hat{q}}_1$$

$$= \frac{2\beta}{RQ_o}(\hat{q}_1 - \hat{q}_2) - \frac{2\alpha_3}{RQ_o}(\dot{\hat{q}}_1 - \dot{\hat{q}}_2) - \frac{2K_3}{R}(\hat{q}_1 + \hat{q}_2). \quad \text{(B-9)}$$

Now define the time constants

$$\tau_1 = \frac{\alpha_1}{RQ_o}, \qquad \tau_3 = \frac{\alpha_3}{RQ_o}$$

and also let

$$G = \frac{\beta}{RQ_o} - \frac{K_3}{R}.$$

Substituting gives

$$\tau_1\tau_3\ddot{\hat{q}}_1 + [\tau_1(1-G) + 2\tau_3]\dot{\hat{q}}_1 + (1-2G)\hat{q}_1$$

$$= G(\hat{f}_1 - \hat{f}_2) - \tau_3(\dot{\hat{f}}_1 - \dot{\hat{f}}_2). \quad \text{(B-10)}$$

The damping ratio for this second order system is

$$\zeta = \frac{(1-G)\tau_1 + 2\tau_3}{2\sqrt{(1-G)\tau_1\tau_3}}$$

and the resonant frequency is

$$\omega_o = \frac{\sqrt{1-2G}}{\sqrt{\tau_1\tau_3}} = \frac{RQ_o\sqrt{1-2G}}{\sqrt{\alpha_1\alpha_3}}.$$

It can also be shown that these small vanes of set A ideally generate only even harmonics in the velocity field. Equation (B-10) shows that the forcing function is $(\hat{f}_1 - \hat{f}_2)$. Figure B-1, also from McMichael, shows the angular dependence between the two sets of vanes to be

$$2\phi_1 = \omega t + \pi/2$$

$$2\phi_2 = \omega t - \pi/2.$$

For a given vane resistance function

$$\hat{f}(\phi) = \frac{a_0}{2} + \sum_{n=1}^{\infty} a_n \cos(2n\phi)$$

it can be seen that

$$\hat{f}_1(\phi_1) + \hat{f}_2(\phi_2) = \frac{a_0}{2} + \sum_{n=0,2,4,\ldots}^{\infty} a_n \cos\left(n(\omega t + \pi/2)\right)$$

and

$$\hat{f}_1(\phi_1) - \hat{f}_2(\phi_2) = \sum_{n=1,3,5,\ldots}^{\infty} a_n \cos\left(n(\omega t - \pi/2)\right)$$

The forcing function $(\hat{f}_1 - \hat{f}_2)$ in the dynamic equation thus ideally only contains odd harmonics. This was difficult to determine experimentally since, for the small vanes, usually only the second harmonic was of a large enough amplitude to be detected by the Fourier analyzer on a logrithmic-magnitude power spectrum (maximum scale of 80 db). The equations cannot be so easily simplified for the situation where the main-flow vanes and bypass vanes are different, because $F_{10} \neq F_{20}$ and $K_1 \neq K_2$. The first line of equation (B-8) may then be written (including the assumption for ΔP_f):

$$q_2 = A'f_1 - B'f_2 + C'\dot{q}_1 + D'q_1 \qquad \text{(B-11)}$$

where

$$A' = Q_{10}/(2rR_2)$$

$$B' = rQ_{10}/(2R_2)$$

$$C' = \alpha_1/(2rR_2Q_{10})$$

$$D' = r.$$

Substituting expression (B-11) into the second line of equation (B-8) yields:

$$\ddot{q}_1\left[\frac{\alpha_3\alpha_1}{2rR_2Q_{10}}\right] + \dot{q}_1\left[\alpha_1\left(1 + \frac{2K_3(1+r)Q_{10} - \beta}{2rR_2Q_{10}}\right) + \frac{\alpha_1\alpha_3}{2rR_2Q_{10}} + \alpha_3\right]$$

$$+ q_1\left[2r^2R_2Q_{10} - \beta(1+r) + 2K_3Q_{10}(1+r)^2\right]$$

$$= -\alpha_3\dot{f}_1 + \dot{f}_2\left[\frac{\alpha_3 rQ_{10}}{2R_2}\right] + \frac{f_1}{2rR_2}\left[\beta Q_{10} - 2K_3Q_{10}^2(1+r) - 2rR_2Q_{10}^2\right]$$

$$+ \frac{f_2}{2R_2r}\left[2K_3Q_{10}^2(1+r)r^2 - Br^2\right] \qquad \text{(B-12)}$$

The effect of the variable bypass, through R_2, is seen to affect each term of equation (B-12).

ACKNOWLEDGEMENTS

I wish to thank Professor Donald A. Kennedy for his timely guidance and valuable suggestions which contributed to the successful completion of this experiment.

I am indebted to Professor Robert A. Kadlec for our enlightening discussions on understanding the complicated nature of unsteady flow effects.

To Captain Michael S. Francis, who encouraged me throughout my graduate study, I offer my gratitude. The technical and equipment support provided by the Frank J. Seiler Research Laboratory (USAF) and coordinated by Captain Francis was invaluable to the conduct of the experiment.

The superb craftsmanship of Mr. Russell Meinzer and Mr. Willy Grothe was greatly appreciated during the construction of the experimental apparatus. I also wish to thank Mr. Wolfgang Bank for his assistance and encouragement in the development of the electronic instrumentation. These gentlemen are talented professionals who provided me with a wealth of valuable practical knowledge.

I am grateful to Donna Weiss for her assistance in the typing of the manuscript.

Finally, I owe special thanks to my wife, Joan, and my son, Ryan, for their patience and understanding through my years of graduate study.